Study of Ξ–nucleus interaction by measurement of twin hypernuclei with hybrid emulsion method

Shuhei Hayakawa

A dissertation
submitted to the Department of Physics
of Osaka University
in partial fulfillment of the requirements
for the degree of

Doctor of Science

February, 2019

Abstract

An experimental study of twin Λ hypernuclei and double-Λ hypernuclei with hybrid emulsion method was performed using a K^- meson beam with the momentum of 1.81 GeV/c at J-PARC K1.8 beam line. Ξ^- hyperons were produced via the quasi-free $p(K^-, K^+)$ reaction at a diamond target. In total, 1.13×10^{11} K^- meson beams were irradiated to the diamond target. Around 10^4 stopped-Ξ^- were recorded by one hundred eighteen emulsion modules. By measuring the position and angle of the produced Ξ^- with spectrometers, we observed eight events having a topology of twin Λ hypernuclei and nine events having a topology of double-Λ hypernucleus while the emulsion scanning is under way. One of the twin Λ hypernuclei event was named "IBUKI event". A reaction process of the IBUKI event was interpreted as $\Xi^- + {}^{14}\mathrm{N} \to {}^{10}_{\Lambda}\mathrm{Be} + {}^{5}_{\Lambda}\mathrm{He}$ by kinematic analysis. The binding energy of $\Xi^- + {}^{14}\mathrm{N}$ system, $B_{\Xi^-}({}^{15}_{\Xi}\mathrm{C})$, was estimated to be 1.27 ± 0.21 MeV. The binding energy indicated a hypernuclear bound state of the $\Xi^- + {}^{14}\mathrm{N}$ by an additional attractive ΞN interaction.

Contents

List of Tables

List of Figures

Chapter 1
Introduction

1.1 Extension of baryon–baryon interaction

All the atomic nuclei composing materials around us consist of protons and neutrons bound by the nuclear force. The nuclear force, the nucleon–nucleon (NN) interaction, has been extensively studied for more than half a century. Various theoretical works [1–3] have been performed to describe the phenomenological nuclear force based on abundant NN scattering experimental data. Several realistic NN potentials were constructed using the one-boson-exchange (OBE) mechanism as represented by Yukawa's pion exchange model. An attractive interaction at a long range (> 1.5 fm) was well described in such models based on OBE, while a repulsive interaction at a short range (< 0.6 fm) was not sufficiently explained. The quark cluster model (QCM) [4] which was based on one-gluon-exchange mechanism between quarks, introduced the origin of the repulsive interaction.

Since Gell-Mann and Zweig had introduced the idea of quarks and flavor SU(3) symmetry ($\mathrm{SU(3)_{flavor}}$) using u, d, and s quarks in 1964 [5–7], the knowledge of the nuclear force have been tried to extend into other constituents of the baryon in which another quantum number, strangeness (S), was introduced. The interaction between quarks are described explicitly by quantum chromodynamics (QCD), a theory of strong interaction. Although it is difficult to calculate the baryon mass due to the non-perturbative feature of QCD, phenomenological quark models have achieved a great success to explain the mass spectra. Introducing s quark, baryons made of u and d quarks with a spin of $1/2$, nucleons, was extended to baryon octet as shown in Figure 1.1 The baryons which have strangeness are called hyperons.

The baryon–baryon interaction are also described using $\mathrm{SU(3)_{flavor}}$ symmetry. Figure 1.2 tabulates irreducible representations for two-baryon systems based on $\mathrm{SU(3)_{flavor}}$ symmetry. The flavor representation of two octet baryons, each transforming in the 8 irreducible representation of SU(3), has a decomposition of the form,

$$8 \otimes 8 = 27 \oplus 10^* \oplus 10 \oplus 8_s \oplus 8_a \oplus 1. \tag{1.1}$$

Flavor channels belonging to the totally symmetric irreducible representations 27, 8_s, and 1 have a total spin equal to zero, while those belonging to the totally antisymmetric irreducible representations 10^*, 10, and 8_a have a total spin equal to one. The NN interaction has been well studied with rich experimental data; nevertheless information derived from them was limited to only 27 and 10^* sectors of the baryon–baryon interaction. The study of hyperon–nucleon (YN) and hyperon–hyperon (YY) interactions is essential for understanding of extended baryon–baryon interaction.

Experimentally, one of the best ways to investigate the baryon–baryon interactions is to study

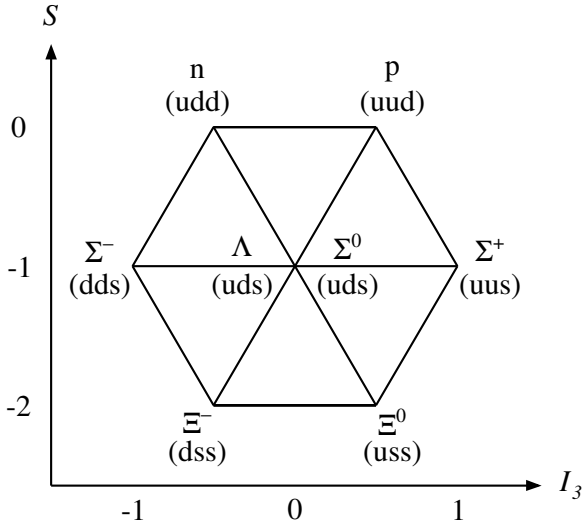

Figure 1.1: Baryon octet in the $SU(3)_{\text{flavor}}$ symmetry with a spin of 1/2. I3 and S represent z component of isospin and strangeness, respectively.

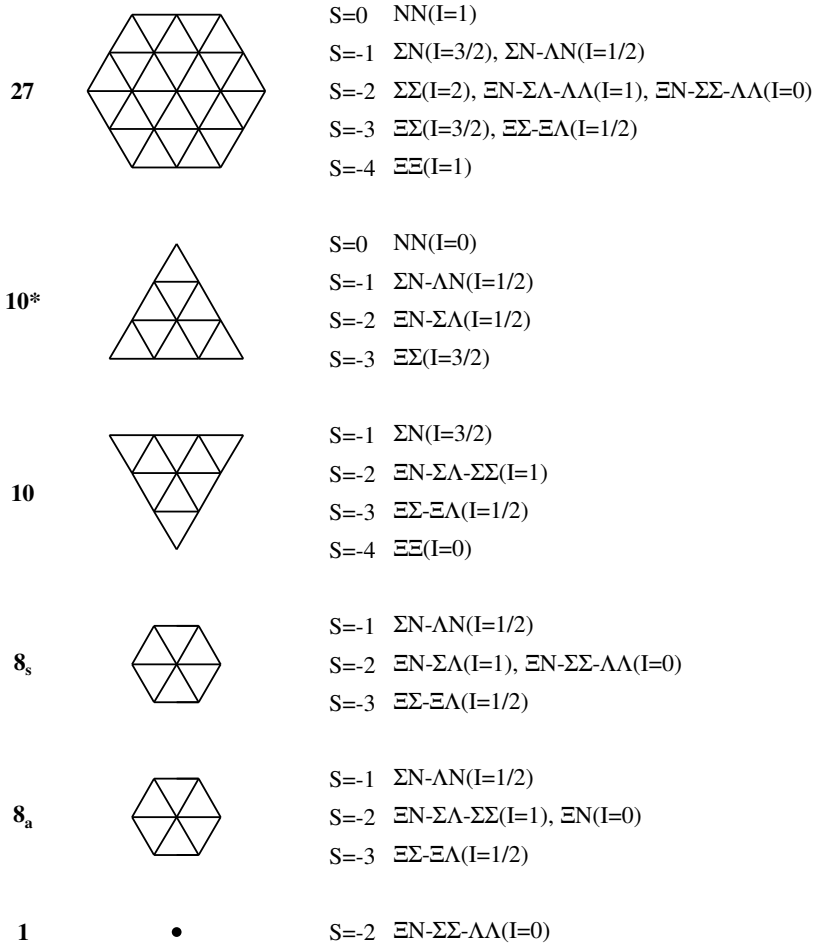

Figure 1.2: Irreducible representations for two-baryon system based on the $SU(3)_{\text{flavor}}$ symmetry.

baryon–baryon scattering. However, it is difficult to produce an intense hyperon beam due to the very short life time of hyperons ($\tau \sim 10^{-10}$ s, $c\tau \sim 10^{-2}$ m). Even in the $S = -1$ sector such as ΛN and ΣN, the available data is limited in both statistics and energy range. The first discovery of a hypernuclear production event was observed in emulsion as a hyperfragment induced by a cosmic ray [8]. Subsequently, most data were taken with bubble chambers and emulsion in the 1960s. Since the 1970s, spectroscopic studies had been conducted intensively [9]. The structure of Λ (or Σ) hypernucleus, which has a Λ (or Σ) hyperon in a nucleus, have been studied. Information of Λ hypernuclear structure has played an essential role in testing and improving the YN interaction models. The studies using the (K^-, π^-) reaction had been performed at the European Organization for Nuclear Research (CERN) and Brookhaven National Laboratory (BNL). The (π^+, K^+) reaction had been utilized for the hypernuclear study at the alternating gradient synchrotron (AGS) of BNL and High Energy Accelerator Research Organization (KEK). Furthermore, hypernuclear γ-ray spectroscopy has been carried out with resolution of a few keV using a germanium detector. At the Thomas Jefferson National Accelerator Facility (JLab), spectroscopy measurements using the $(e, e'K^+)$ reaction were conducted with the high-quality and high-intensity electron beams. Thus, Λ hypernuclei have been widely investigated in the mass range up to $A = 208$.

As for the $S = -2$ sector, the study on Ξ hypernuclei and double-Λ hypernuclei provides information around the ΞN and $\Lambda\Lambda$ interaction as is the case with single-Λ hypernuclei in the $S = -1$ sector. Information of the ΞN and $\Lambda\Lambda$ interaction has been extracted by measuring the binding energies of a Ξ^- hyperon and Λ hyperons in Ξ hypernuclei and double-Λ hypernuclei, respectively.

Since the electric charge of the Ξ^- hyperon is -1, Ξ^- hypernuclei have a different charge from the core nuclei. In hypernuclei, A and Z are defined as the baryon number and the electric charge, respectively. The Ξ^- hyperon in an atomic state of a nucleus may interact with the nucleus by the Ξ^-–nucleus interaction. Thus, the binding energy of the Ξ^- hyperon is defined as

$$B_{\Xi^-}({}^{A}_{\Xi}Z) = M({}^{A-1}(Z+1)) + M(\Xi^-) - M({}^{A}_{\Xi}Z), \tag{1.2}$$

where $B_{\Xi^-}({}^{A}_{\Xi}Z)$ is the binding energy of the Ξ^- hyperon in the Ξ^--nucleus system. $M({}^{A-1}(Z+1))$, $M(\Xi^-)$, and $M({}^{A}_{\Xi}Z)$ are the masses of the core nucleus, the Ξ^- hyperon, and the Ξ^-–nucleus system, respectively.

Similarly, information of the $\Lambda\Lambda$ interaction is obtained by measuring the binding energy of two Λ hyperons in double-Λ hypernuclei. The binding energy of two Λ hyperons is defined as

$$B_{\Lambda\Lambda}({}^{A}_{\Lambda\Lambda}Z) = M({}^{A-2}Z) + 2M(\Lambda) - M({}^{A}_{\Lambda\Lambda}Z), \tag{1.3}$$

where $B_{\Lambda\Lambda}({}^{A}_{\Lambda\Lambda}Z)$ is the binding energy of the two Λ hyperons in the double-Λ hypernucleus. $M({}^{A-2}Z)$, $M(\Lambda)$, and $M({}^{A}_{\Lambda\Lambda}Z)$ are the masses of the core nucleus, the Λ hyperon, and the double-Λ hypernucleus.

Experimental data of Ξ hypernuclei and double-Λ hypernuclei were not obtained hardly any in contrast to the Λ hypernuclei. The experimental information of the ΞN and $\Lambda\Lambda$ interactions is quite essential to understand the baryon–baryon interaction.

1.2 Past experiments

Nuclear emulsion has been used for various experiments to detect a sequential weak decay of hypernuclei in the $S = -2$ sector. The method of absorbing Ξ^- hyperons into nuclei of emulsion has been used and succeeded in a study of Ξ^- hypernuclei and double-Λ hypernuclei.

Several emulsion experiments reported production of twin Λ hypernuclei, where two single-Λ hypernuclei were produced simultaneously after the formation of a Ξ^- hypernucleus or a Ξ^- atom. If all decay fragments from the absorption point of a Ξ^- hyperon are identified, and their kinematic energies are measured, the binding energy of the Ξ^- hyperon, B_{Ξ^-}, is calculated with (1.2). Furthermore, if the positive B_{Ξ^-} value is obtained, it presents the Ξ^- hypernuclear production. Thus, the reconstruction of the masses of twin Λ hypernuclei provides information of the binding energy of Ξ^- in the nucleus.

1.2.1 Twin Λ hypernuclei

Wilkinson et al. reported an event of twin hypernuclei in an emulsion exposed to π^- mesons with the momentum of 4.5 GeV/c [10]. They suggested that $B_{\Xi^-}(^{8}_{\Xi}\mathrm{He}) = 5.9 \pm 1.2$ MeV or $B_{\Xi^-}(^{9}_{\Xi}\mathrm{He}) = 3.6 \pm 1.2$ MeV. Bhowmik [11] presented a twin hypernuclei candidate. However, there remained the possibility of the in-flight reaction of the Ξ^- hyperon. An event associated with two single-Λ hypernuclei at the reaction point was reported by Steinberg et al. [12]. In the experiment at the CERN PS, Bechdolff et al. [13] found four events involving a hyperfragment pair. Taking into consideration only the most probable interpretation of each single hyperfragment, the binding energies were deduced to be $B_{\Xi^-}(^{17}_{\Xi}\mathrm{O}) = 16.0 \pm 5.5$ MeV, $B_{\Xi^-}(^{29,30}_{\Xi}\mathrm{Mg}) = 2.4 \pm 6.3$ MeV, $B_{\Xi^-}(^{28}_{\Xi}\mathrm{Al}) = 23.2 \pm 6.8$ MeV, and $B_{\Xi^-}(^{15}_{\Xi}\mathrm{C}) = 16.0 \pm 4.7$ MeV. Mondal et al. [14] presented $B_{\Xi^-}(^{13}_{\Xi}\mathrm{C}) = 18.1 \pm 3.2$ MeV. They also reported experimental values of B_{Ξ^-} for six events with twin Λ hypernuclei versus mass number.

In the 1990s, the KEK E176 experiment reported two twin Λ hypernuclear events [15, 16]. Both events were interpreted as the most probable decay mode of $\Xi^- + {}^{12}\mathrm{C} \to {}^{9}_{\Lambda}\mathrm{Be} + {}^{4}_{\Lambda}\mathrm{H}$. They reanalyzed the kinematics of both events and revised the values of the binding energy later [17, 18]. The updated B_{Ξ^-} value was obtained to be 0.82 $\pm$ 0.17 MeV from one of them. The other provided $B_{\Xi^-} = 3.89 \pm 0.14$ MeV if both Λ hypernuclei were in ground states, $B_{\Xi^-} = 0.82 \pm 0.14$ MeV if the ${}^{9}_{\Lambda}\mathrm{Be}$ was in an excited state, or $B_{\Xi^-} = 2.84 \pm 0.15$ MeV if the ${}^{4}_{\Lambda}\mathrm{H}$ was in an excited state. In 2014, the KEK E373 experiment presented a twin Λ hypernuclear event [19], named "KISO event". The event was uniquely interpreted as the decay mode of $\Xi^- + {}^{14}\mathrm{N} \to {}^{10}_{\Lambda}\mathrm{Be} + {}^{5}_{\Lambda}\mathrm{He}$. Since Gogami et al. [20] revised the binding energy of the ${}^{10}_{\Lambda}\mathrm{Be}$ hypernucleus and measured the levels of the excited states, the B_{Ξ^-} value of the KISO event was also revised to be 3.87 ± 0.21 MeV or 1.03 ± 0.18 MeV for production of the ${}^{10}_{\Lambda}\mathrm{Be}$ nucleus as either the ground state or the first excited state, respectively [18]. Even for production of the ${}^{10}_{\Lambda}\mathrm{Be}$ nucleus in the excited state, the binding energy of the Ξ^- hyperon was deeper than that in the case of considering only the Coulomb force from the nitrogen nucleus at the atomic $3D$ state. The B_{Ξ^-} value differed from the atomic $3D$ level by 4.6 σ. Therefore, the KISO event was interpreted as a bound state of the Ξ^-–${}^{14}\mathrm{N}$ system with an additional attractive

ΞN interaction, while there remained the ambiguity of the B_{Ξ^-} value depending on the state of the ${}^{10}_{\Lambda}$Be nucleus.

1.2.2 Double-Λ hypernucleus

Danysz, Prowse, and Mondal reported three observations of the double-Λ hypernuclei with nuclear emulsion in the 1960s and 1970s [21–23]. The reanalysis result of Danysz's event indicated the production of ${}^{10}_{\Lambda\Lambda}$Be which leads to $B_{\Lambda\Lambda} = 14.7 \pm 0.4$ MeV [18, 24, 25]. Since the authenticity of the event identification was considered doubtful, events of Prowse and Mondal were no longer regarded as to be a double-Λ hypernucleus. The KEK E176 experiment found four sequential decay of a double-Λ hypernucleus at rest in emulsion. One of them was interpreted to be ${}^{13}_{\Lambda\Lambda}$B as the most probable case. The binding energy was reported to be $B_{\Lambda\Lambda} = 23.3 \pm 0.7$ MeV [17]. The KEK E373 experiment presented seven events of double-Λ hypernuclear production among about 10^3 events of Ξ^- hyperons captured at rest by emulsion nuclei. The $B_{\Lambda\Lambda}$ values of four events were reported [26]. They uniquely identified one of them as ${}^{6}_{\Lambda\Lambda}$He, called "NAGARA event" [27]. The $B_{\Lambda\Lambda}$ value was obtained to be 6.91 ± 0.16 MeV. Another event, called "MIKAGE event", had three interpretations, $B_{\Lambda\Lambda}({}^{6}_{\Lambda\Lambda}\mathrm{He}) = 10.01 \pm 1.71$ MeV with the target of ^{12}C, $B_{\Lambda\Lambda}({}^{11}_{\Lambda\Lambda}\mathrm{Be}) = 22.15 \pm 2.94$ MeV with the target of ^{12}C, and $B_{\Lambda\Lambda}({}^{11}_{\Lambda\Lambda}\mathrm{Be}) = 23.05 \pm 2.59$ MeV with the target of ^{14}N, by considering the consistency with NAGARA event. From the event called "Demachi-Yanagi event", the most probable mode provided the $B_{\Lambda\Lambda}$ value of 11.90 ± 0.13 MeV. They also found a double-Λ hypernuclear event, called "Hida event". Two processes remained as possible modes which provided a consistency with the NAGARA event. The obtained values were $B_{\Lambda\Lambda}({}^{12}_{\Lambda\Lambda}\mathrm{Be}) = 22.48 \pm 1.21$ MeV and $B_{\Lambda\Lambda}({}^{11}_{\Lambda\Lambda}\mathrm{Be}) = 20.83 \pm 1.27$ MeV.

The $B_{\Lambda\Lambda}$ values mentioned above were all calculated with the assumption for Ξ^- hyperon capture in the atomic $3D$ level.

1.2.3 Other experiments

The spectroscopic study of the $\Xi^- N$ interaction were performed using the (K^-, K^+) reaction. The excitation energy of Ξ^- in ${}^{12}_{\Xi}$Be was presented by the KEK E224 experiment [28]. The spectra deduced the well depth of the Ξ^--nucleus of 16–17 MeV. The AGS E885 experiment reported the excitation-energy spectra, which were possible to interpret as Ξ^- hypernuclei via the ${}^{12}\mathrm{C}(K^-, K^+)X$ reaction [29]. The Ξ^--nucleus potential of around 14 MeV with the Woods-Saxon prescription was presented as reasonable agreement. The AGS E906 experiment carried out the $\Xi^- N$ scattering experiment [30]. Using quasi-free Ξ^- production via the (K^-, K^+) reaction on ^{9}Be target, the $\Xi^- N$ elastic scattering cross section was deduced to be $30.7 \pm 6.7(stat)^{+3.7}_{-3.6}(syst)$ mb The ratio of $\Xi^- p$ to $\Xi^- n$ scattering cross section was also obtained to be $1.1\ ^{+1.4}_{-0.7}(stat)^{+0.7}_{-0.4}(syst)$. In all experiments, sufficient statistics were not obtained due to the low intensity of the K^- beam.

1.3 Theoretical studies on $\Xi N/\Lambda\Lambda$ interactions

The Nijmegen group has developed a lot of OBE potentials for the baryon–baryon interaction including the strangeness. The OBE potentials with the repulsive hard-core were adopted for the model D (NHC-D) [31, 32] and F (NHC-F) [33]. NHC-D was used as a qualitative representation for YN, YY interactions in the 1980s. However, NHC-D was insufficient for a test of the spin-doublet states in Λ hypernuclei. Interpreting the result of twin hypernuclei experiment [14] as being bound in the $1_{s_{1/2}}$ ground state in Ξ hypernuclei, Dover and Gal [34] investigated the Ξ^- hyperon single-particle potential, $V_\Xi(r)$, assuming a Woods-Saxon form. They presented the well depth to be 21–24 MeV depending on the radius of the core nucleus. Model NSC97 [35] based on the soft-core OBE potential instead of the phenomenological hard core was studied by the Nijmegen group.

From the 2000s on, the Nijmegen group has developed Extended-Soft-Core models, ESC00 [36], ESC04 [37, 38], and modified to be ESC08 [39–42]. ESC treats two-meson exchange processes explicitly. ESC08c provides the attractive ΞN interaction of $B_{\Xi^-}(^{13}_{\Xi}\mathrm{B}) = 0.68$ MeV and $B_{\Xi^-}(^{15}_{\Xi}\mathrm{C}) = 1.22$ MeV if a Ξ^- hyperon is absorbed at the $2P$ atomic state.

The Ehime group proposed another OBE model [43, 44]. The binding energies of a Ξ^- hyperon are deduced to be $B_{\Xi^-}(^{13}_{\Xi}\mathrm{B}) = 0.58$ MeV, $B_{\Xi^-}(^{15}_{\Xi}\mathrm{C}) = 1.14$ MeV, and $B_{\Xi^-}(^{17}_{\Xi}\mathrm{N}) = 1.77$ MeV in the case of an absorption of the Ξ^- hyperon at the $2P$ atomic state.

With respect to the $\Lambda\Lambda$ interaction, Filikhin and Gal reported the calculation of the $B_{\Lambda\Lambda}$ values [45]. Hiyama et al. presented investigated the level structure of $^{10}_{\Lambda\Lambda}$Be and extended the model to the case of four-body model [46]. Since the mass of the Ξ^- hyperon was updated [47], the calculation was also revised later [48]. The $B_{\Lambda\Lambda}$ values of $^{10}_{\Lambda\Lambda}$Be with the 0^+ and 2^+ states were 11.88 MeV and 14.74 MeV, respectively.

1.4 J-PARC E07 experiment

J-PARC E07 experiment [49] has been performed at J-PARC K1.8 beam line. The experiment aimed to search for double-strangeness nuclei such as Ξ hypernuclei and double-Λ hypernuclei. The detail of the experimental procedure of J-PARC E07 experiment is described in Chapter 2. In the experiment, Ξ hypernuclei and double-Λ hypernuclei were generated with the nuclear Ξ^- hyperons captured at rest in nuclear emulsion. The Ξ^- hyperons were produced via the (K^-, K^+) reaction at a diamond target. The positions and angles of incident Ξ^- hyperons on the emulsion surface were measured with the silicon strip detectors. The Ξ^- hyperon captured and observed in the emulsion. Decay fragments were emitted from the stop point of the Ξ^- hyperon. Twin Λ and double-Λ hypernuclear decay were observed as the sequential weak decay in the emulsion. By using high purity kaon beam of J-PARC K1.8 beam line, high statistics have been obtained.

Figure 1.3 shows a illustration of the production process of double-strangeness nuclei via the Ξ^- hyperon capture at rest. A Ξ^- hyperon produced via the quasi-free $p(K^-, K^+)\Xi^-$ reaction enters emulsion. An atom in emulsion captures a stopped Ξ^- hyperon. It is captured on an atomic orbit in a highly excited level at first. A captured Ξ^- hyperon is transferred into lower orbits with

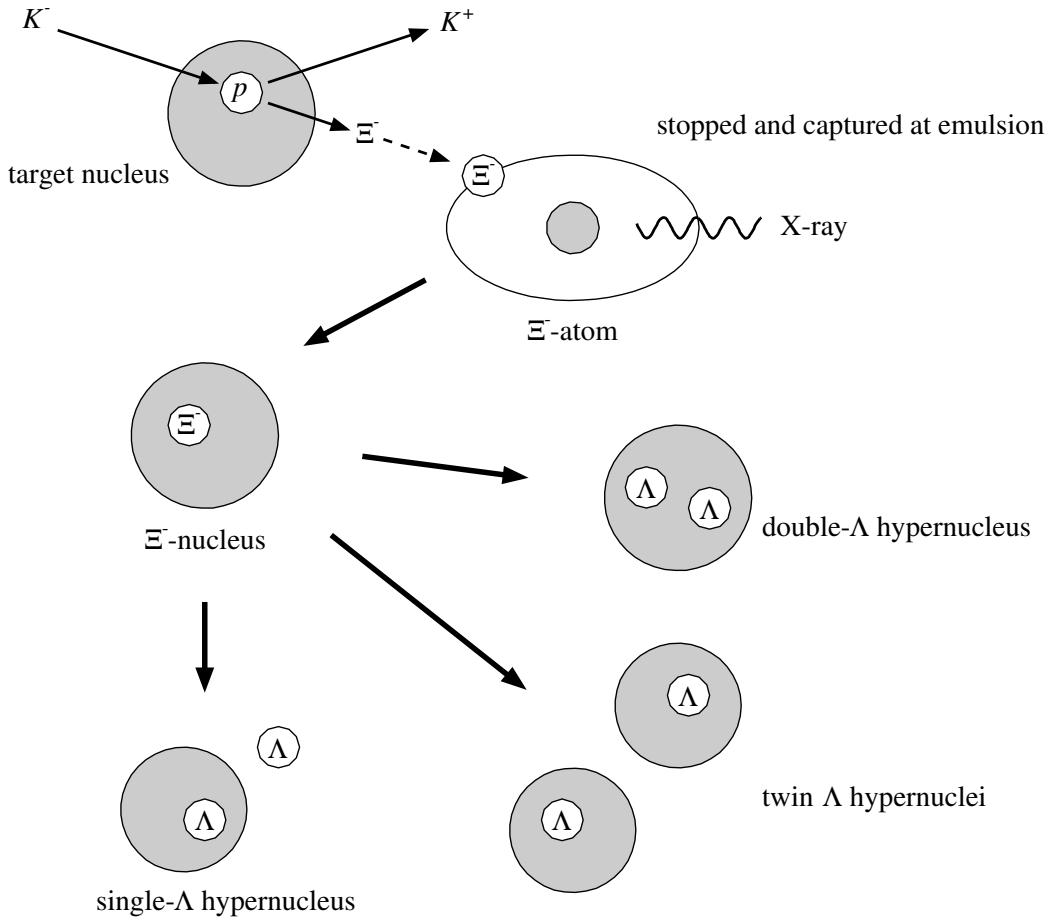

Figure 1.3: Production process of twin Λ hypernuclei and double-Λ hypernucleus.

emitting Auger electrons and X-rays. Finally, the Ξ^- hyperon is absorbed by the nucleus. When a Ξ^- hyperon is brought to rest, it will interact with a nucleus to produce two Λ hyperons according to the reaction

$$\Xi^- + p \rightarrow \Lambda + \Lambda + 28.6 \text{ MeV}, \tag{1.4}$$

where 28.6 MeV is a Q value of the reaction. Since the energy release in such an interaction is not large, the two Λ hyperons may easily form twin Λ hypernuclei and a double-Λ hypernucleus with some probability.

Ξ^- atomic X-rays also provides information on the ΞN interaction. In J-PARC E07 experiment, we also installed a germanium detector array upstream of the emulsion for the detection of Ξ^- atomic X-rays and the measurement of their energy shifts.

Chapter 2 describes the experimental procedure in detail. The analysis is presented in Chapter 3 with regard to the spectrometer. The emulsion scanning system and analysis procedure are described in Chapter 4. An observed twin Λ hypernuclear event is described and discussed in Chapter 5. The work is summarized in Chapter 6.

Chapter 2

Experiment

2.1 Overview

The J-PARC E07 experiment was performed at the K1.8 beam line in the J-PARC hadron facility in 2016 and 2017. The Ξ^-, produced via the quasi-free $p(K^-, K^+)\Xi^-$ reaction in a diamond target at $p_{K^-} = 1.81$ GeV/c, were slowed down and some of them came to rest in a nuclear emulsion. A typical beam intensity was 3×10^5 per spill with a spill length of around 2 seconds. In order to measure momenta of beam kaon and scattered kaon, K1.8 beam line and KURAMA spectrometers were used, respectively. In addition, a position and an angle of the produced Ξ^- were measured with silicon strip detectors (SSD) which were located between the target and the nuclear emulsion. Hyperfragments emitted from the Ξ^- hyperon absorption points were observed with the nuclear emulsion detector. Charged particles emitted from the hyperfragments and escaping out of the emulsion stack were detected by two SSDs placed both upstream and downstream of the emulsion. In this chapter, details of the experimental components are described.

2.2 J-PARC and hadron experimental facility

J-PARC (Japan Proton Accelerator Research Complex) [50] is a high intensity and multi-purpose proton accelerator facility which aims to explore the frontiers in nuclear physics, particle physics, materials and life sciences and nuclear technology with the highest beam power in the world. J-PARC consists of three accelerators (LINAC: a linear accelerator, RCS: a rapid cycling synchrotron and MR: a main ring) and three experimental facilities (MLF: materials and life science experimental facility, NU: neutrino experimental facility and HD: hadron experimental facility).

LINAC is composed of a negative hydrogen, H^- ion source, a radio frequency quadrupole, a drift tube linac and a separated-type drift tube linac [51]. The produced H^- beam was accelerated up to 400 MeV. The accelerated H^- is injected to RCS and converted to a proton with a carbon stripper foil [52]. RCS accelerates the injected proton up to 3 GeV. The 3 GeV proton beam is transported to mainly MLF and partly MR [53]. MR accelerates the proton up to 30 GeV and delivers it to NU by the fast extraction or HD by the slow extraction.

The primary proton beam from MR was extracted to HD for a duration of around 2 seconds in every 5.52 seconds in the experiment. The duration of the beam extraction is called a spill. HD consisted of a primary beam line and three secondary beam lines (K1.8, K1.8BR, and KL) The proton beam transported from MR comes to the primary target, T1. Secondary hadron beams such

as kaon, pion and proton produced at T1 target are delivered to experimental areas through the secondary beam lines. T1 target consisted of gold. The size of T1 target was 15-mm wide, 11-mm high and 66-mm thick.

2.3 K1.8 beam line

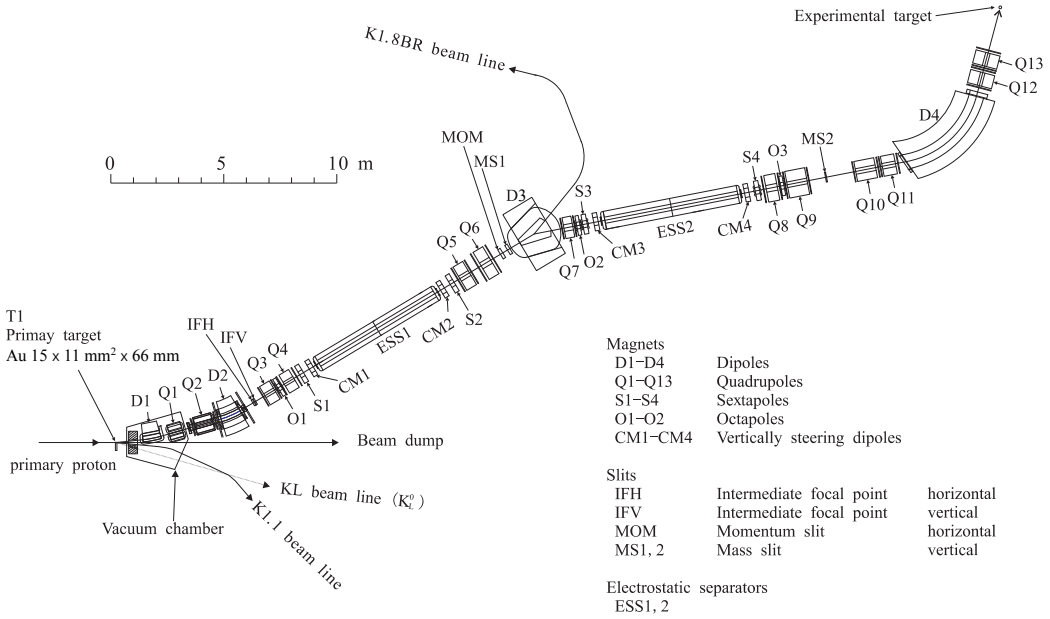

Figure 2.1: Schematic view of the K1.8 beam line.

K1.8 beam line is a general purpose mass separated beam line which can supply various secondary hadron beams such as $K^{\pm}$, $\pi^{\pm}$, p and $\bar{p}$ [54]. The beam line was designed as a high intensity and high purity kaon beam line for the hypernuclear experiment using the (K^-, K^+) reaction. Since the production cross section of Ξ^- via the (K^-, K^+) reaction becomes maximum at the beam momentum of 1.8 GeV/c, the beam line was optimized for the momentum and the maximum beam momentum is 2.0 GeV/c. Figure 2.1 shows a schematic view of K1.8 beam line, which is composed of four sections as follows, the front-end section, the first mass separation section, the second mass separation section and the momentum analysis section.

Front-end section

The front-end section is from D1 to IFV in Figure 2.1. Two dipole magnets (D1 and D2) and two quadrupole magnets (Q1 and Q2) are installed. The extraction angle is set to be 6°, where the kaon production cross section is expected to be at the maximum. Some of the beam line elements in this section are operated in a large vacuum tank of $\sim$ 1 Pa. The transported beam is vertically focused at the intermediate focus (IF) point. Both horizontal and vertical beam profiles are shaped with a horizontal slit (IFH) and a vertical slit (IFV). These slits reject so-called cloud pions which are

produced by the decay of K^0, and scattered pions by materials of upstream sections.

Mass separation section

The first mass separation section is from Q3 to MS1 and the second mass separation section is from Q7 to MS2 in Figure 2.1. In this section, one dipole magnet (D3), seven quadrupole magnets (from Q3 to Q9), four sextupole magnets (from S1 to S4), three octupole magnets (from O1 to O3) and two electrostatic separators (ESS1 and ESS2) with four correction magnets (from CM1 to CM4) are located. Two electrostatic separators are used to separate kaons from pions in both sections. The double mass separation system is an essential component for the K1.8 beam line.

An electrostatic separator generates a vertical electric field along the beam axis to separate particles with the same momentum by their mass differences. The electric field is generated in the 10 cm gap between parallel electrode plates with a size of 30 cm in width and 6 m in length. The maximum gradient of the field is 75 kV/cm adding He/Ne insulating gas in the chamber up to a few times 10^{-2} Pa. In the experiment, the electric field of both ESS1 and ESS2 was set to 50 kV/cm.

Correction magnets (CM1–4) were essential parts of the particle separation. The particle orbits are corrected by CM1–4 located both at the entrance and the exit of the electrostatic separators. After ESS1 and ESS2, the beam is focused in the vertical direction at each mass slit (MS1 and MS2). For the present pion beam experiment, the scattering of correction magnets were adjusted to let pions only pass through the slit. A horizontal momentum slit (MOM) determines the momentum bite of the secondary particles.

Momentum analysis section

The momentum analysis section is called as K1.8 beam line spectrometer. The magnet configuration is a $QQDQQ$ system (Q10–13 and D4). The beam is focused on an experimental target and the momentum of each particle is analyzed.

In the experiment, the central momentum was set to around 1.81 GeV/c for the (K^-, K^+) reaction and the typical momentum bite was about 3.4% (FWHM) as shown in Figure 2.2. The horizontal and vertical size and angle of K^- beam are shown in Figure 2.3. The typical beam size was 16 mm (horizontal) $\times$ 11 mm (vertical) in FWHM. A diamond target was used as the experimental target and its size was 50 mm (horizontal) $\times$ 30 mm (vertical). The beam angles at the experimental target were 0.05 rad and 0.004 rad in FWHM, respectively.

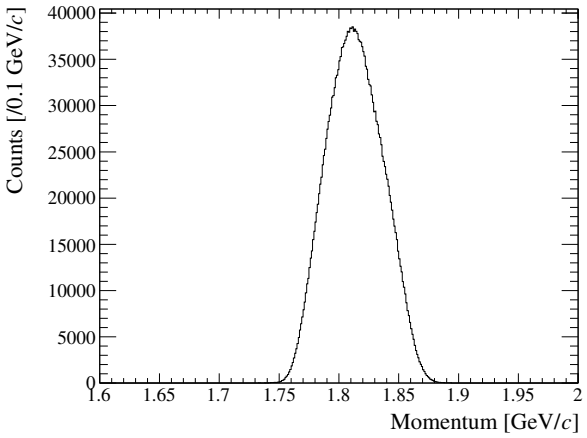

Figure 2.2: Momentum distribution of K^- beam.

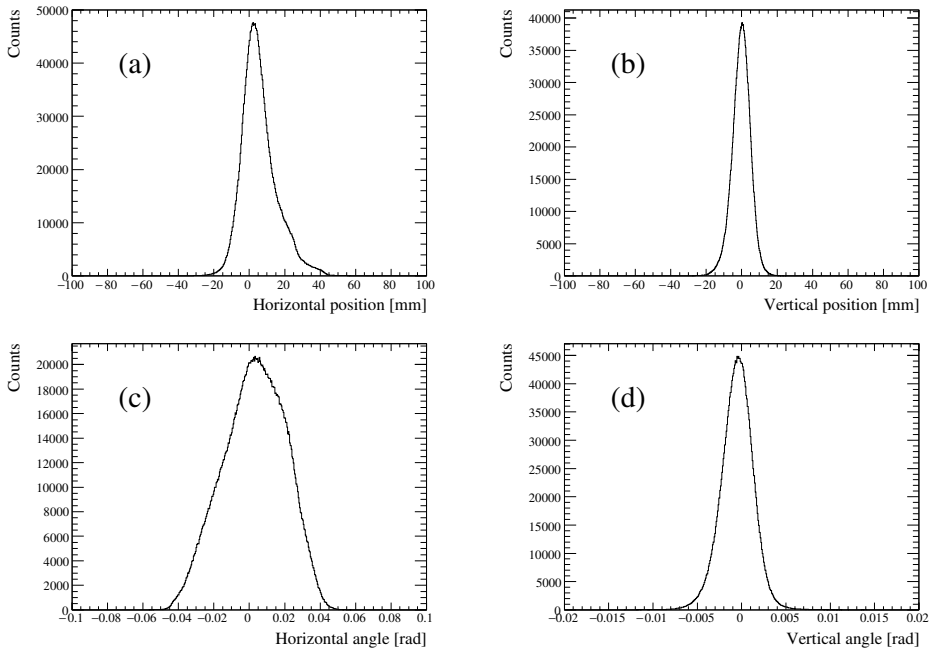

Figure 2.3: Profiles of K^- beam at the experimental target. The horizontal and vertical positions are shown in (a) and (b), respectively. The horizontal and vertical angles are shown in (c) and (d), respectively.

2.4 K1.8 beam line spectrometer

The last part of the K1.8 beam line plays a role as a beam spectrometer to analyze momentum and trajectory of each particle. The schematic view of the K1.8 beam line spectrometer is shown in Figure 2.4. The spectrometer consisted of two timing counters of plastic scintillation hodoscopes (BH1 and BH2), two Čerenkov counters for the particle identification (BAC1 and BAC2), three tracking detectors (BFT, BC3 and BC4) in front and at the exit of the $QQDQQ$ magnets, and a

position detector for a momentum trigger (FBH). Moreover, a collimator of tungsten blocks was installed at the downstream position between BC3 and BC4 in order to reduce pions generated after MS2.

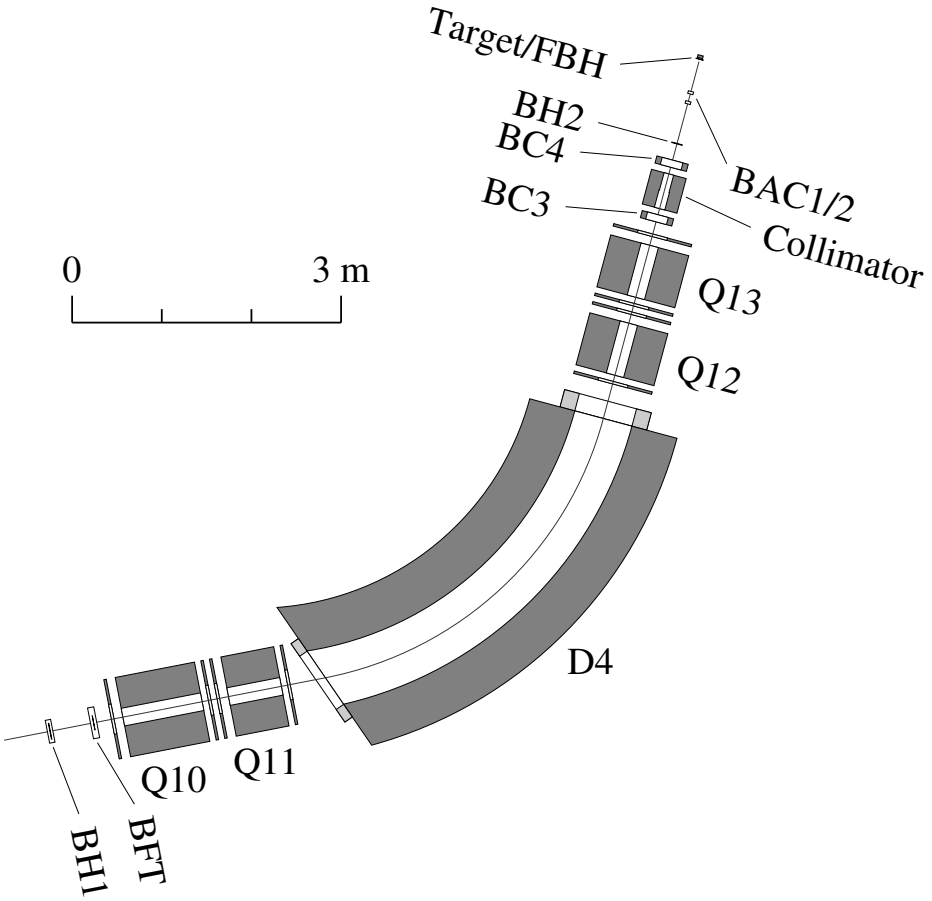

Figure 2.4: Schematic view of K1.8 beam line spectrometer.

The beam momentum is reconstructed from the horizontal position at the entrance and the trajectories at the exit using the third-order transfer matrix. The design value of the momentum resolution is $\Delta p/p = 3.3 \times 10^{-4}$ (FWHM) with a position resolution of 200 μm (rms). The magnetic field of the dipole magnet (D4) was monitored during the experiment with a high precision hall probe, Digital Teslameter 151 (DTM-151) with the accuracy of 1.7×10^{-6}. The observed fluctuation $\Delta B/B$ was less than 10^{-4}. Design specifications of the K1.8 beam line spectrometer are listed in Table 2.1.

Table 2.1: Specifications of K1.8 beam line spectrometer

Momentum resolution	3.3×10^{-4} (FWHM)
Maximum momentum	2.0 GeV/c
Maximum field	1.67 T
Bending angle	64°
Central orbital radius of D4	4 m
Pole gap of D4	19 cm
Flight path from BH1 to BH2	10.33 m

2.4.1 Trigger counters

Five trigger counters, BH1, BH2, BAC1, BAC2 and FBH, were installed in the K1.8 beam line spectrometer. Table 2.2 lists specifications of the trigger counters of K1.8 beam line spectrometer.

Table 2.2: Specifications of trigger counters of K1.8 beam line spectrometer

	Sensitive area (W×H×T [mm])	Scintillator/Radiator	Photon detector (Hamamatsu Photonics K.K.)
BH1	$170 \times 66 \times 5$	Plastic scintillator: BC-420	$3/4''$ PMT: H6524MOD
BH2	$120 \times 40 \times 6$	Plastic scintillator: EJ-212	$2''$ PMT: H10570
BAC1	$170 \times 70 \times 46$	Silica aerogel ($n = 1.03$)	$3''$ PMT: R6683
BAC2	$170 \times 70 \times 46$	Silica aerogel ($n = 1.03$)	$3''$ PMT: R6683
FBH	$82.5 \times 30 \times 2$	Plastic scintillator: EJ-212	1×1 mm^2 MPPC: S12571-100P

BH1 and BH2 counters

Two hodoscopes, BH1 and BH2 (Beam Hodoscope) were installed at the entrance and exit of the K1.8 beam line spectrometer.

BH1 consisted of 11 segments of 5-mm-thick plastic scintillators (Saint-Gobain BC420) with different widths of 8, 12, 16 and 20 mm to reduce and flatten the counting rate of each segment.

Figure 2.5 (a) shows a schematic drawing of BH1. Each segment is overlapped with the next segments by 1 mm to avoid a dead area. The size of a sensitive area was 170 mm (horizontal) × 66 mm (vertical). Phototubes (Hamamatsu H1650MOD) equipped with a three-stage booster are connected on both ends of each scintillator.

BH2 was one plastic scintillator (Eljen Technology EJ-212) with 6-mm thickness. The size of a sensitive area is 120-mm wide and 40-mm high. Phototubes (Hamamatsu H10570) were attached on both ends of the scintillator. Schematic drawing of BH2 is shown in Figure 2.5 (b). BH2 defined the start timing for all timing measurements. Since the beam kaon purity and the data aquisition efficiency are essential for the emulsion experiment, a beam intensity was 3×10^5 per spill. In the experiment, therefore, BH2 was not segmented in order to avoid an energy loss due to overlapping, and to simplify the timing analysis.

The time-of-flight (TOF) of beam particles was measured with BH1 and BH2. Figure 2.6 shows the beam time-of-flight with the unbiased trigger. The flight length was 10.33 m, where the time difference between kaons and pions was 1.16 ns at 1.81 GeV/c. The timing resolution of the beam TOF was 350 ps in FWHM for kaons.

BAC1 and BAC2

BAC (Beam Aerogel Čerenkov counter) is a threshold-type silica aerogel Čerenkov counter for the veto on light particles such as pions, muons and electrons in a beam. Two BACs, BAC1 and BAC2, were installed at the downstream of BH2 to select beam kaons in the trigger level. Figure 2.7 shows a schematic view of BAC. Silica aerogel plates with the index of 1.03 were placed at the upstream side as a Čerenkov light radiator. Figure 2.8 shows the threshold of the refractive index for Čerenkov

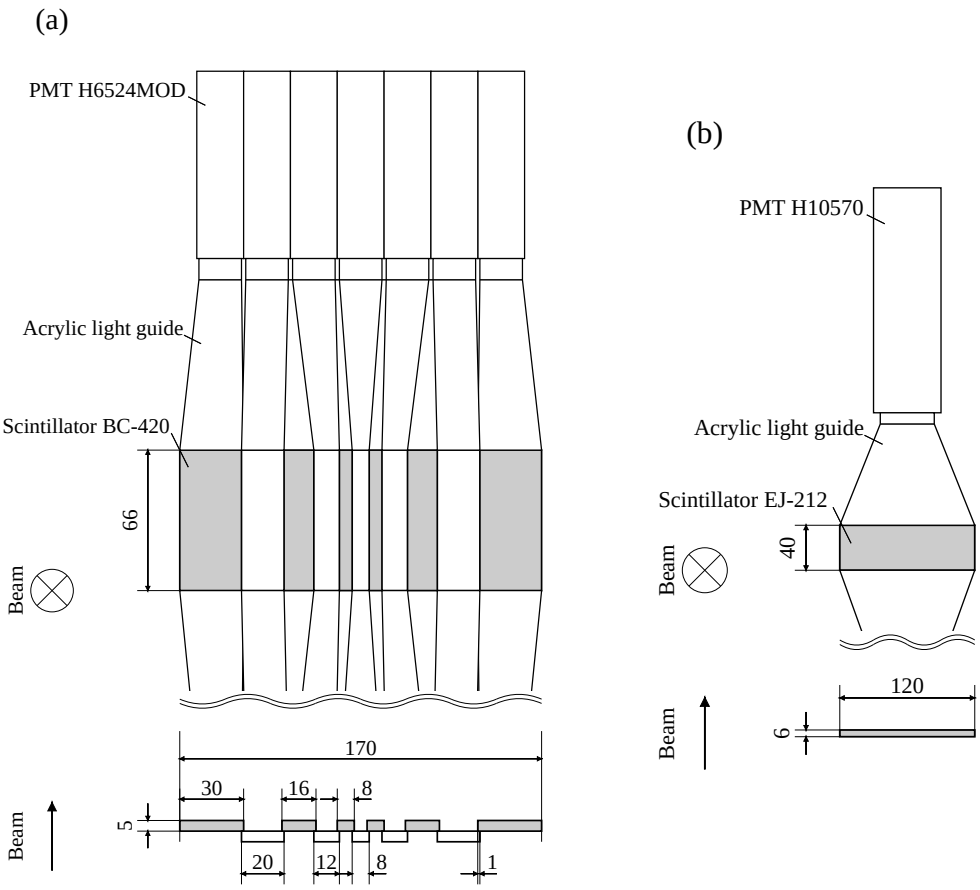

Figure 2.5: Schematic drawing of BH1 and BH2.

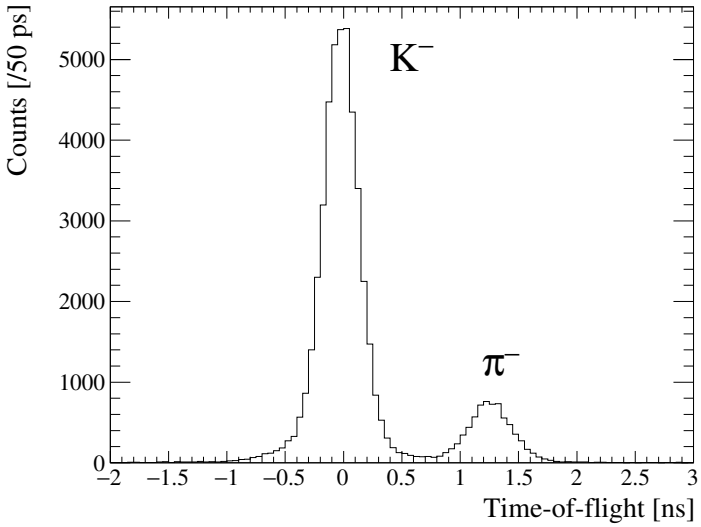

Figure 2.6: Beam time-of-flight.

radiation as a function of the momentum for each particle. The sensitive area was 170-mm wide and 70-mm high. Two fine-mesh phototubes (Hamamatsu R6683) were connected on the bottom side. On the inner surfaces of both upstream and downstream window, three 100-μm-thick teflon sheets were attached as a diffusive reflector to guide a Čerenkov light toward phototubes. On the other inner surfaces, six teflon sheets were attached. Two BACs having the same structure installed as BAC1 and BAC2. In each BAC, we mixed two analog signals of phototubes with an analog mixer (ORTEC AN308/NL). The momentum threshold of pions and kaons are 0.57 and 2.0 GeV/c. The detection efficiencies of BAC1 and BAC2 were obtained to be 99.97% and 99.96% for pions, and 2.2% and 2.4% for kaons, respectively.

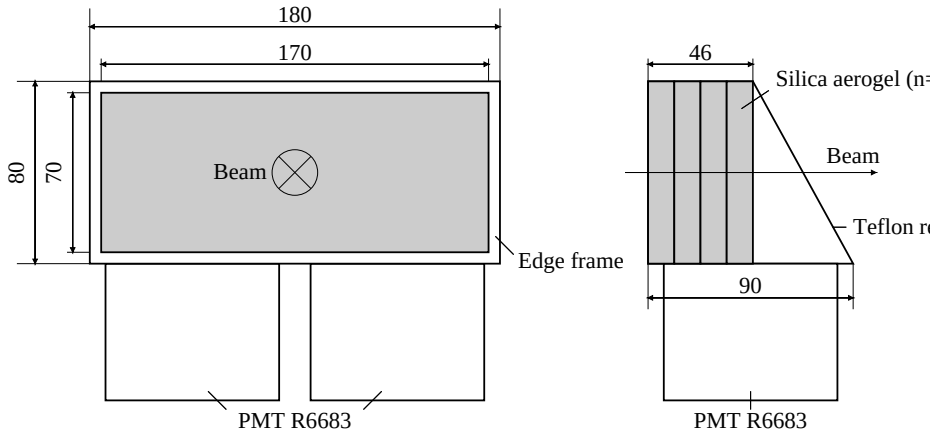

Figure 2.7: Schematic drawing of BAC.

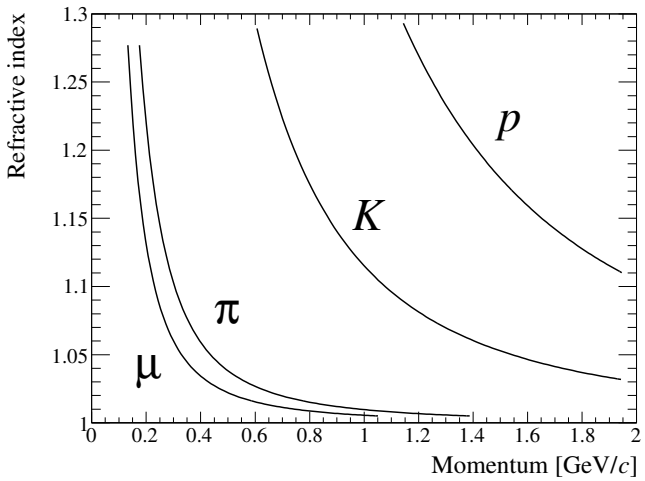

Figure 2.8: The refractive index for Čerenkov radiation as a function of the momentum.

FBH

FBH (Fine Beam Hodoscope) was placed just in front of an experimental target to measure a precise position of an incident beam particle. FBH was segmented into sixteen vertical pieces of 2-mm-thick plastic scintillators (Eljen Technology EJ-212). Each scintillator had a groove to fix a wavelength

shifting fiber (Kuraray PSFY-11J) with a diameter of 1 mm. The scintillator width was 7.5 mm and each segment was overlapped with the next segments by 2.5 mm as shown in Figure 2.9. The overlap enabled to increase the effective number of segments by using the number of hits. The scintillator and fiber were wrapped by teflon sheets. The sensitive area was 30-mm high and 82.5 mm wide to cover the target area. MPPC circuit boards were attached on both ends of each fiber. Sixteen MPPCs (Hamamatsu S12571-100P) were surface-mounted on the board. The sensor size was a square of 1 mm × 1 mm. Figure 2.10 shows a schematic layout of the MPPC circuit board and a circuit of the board.

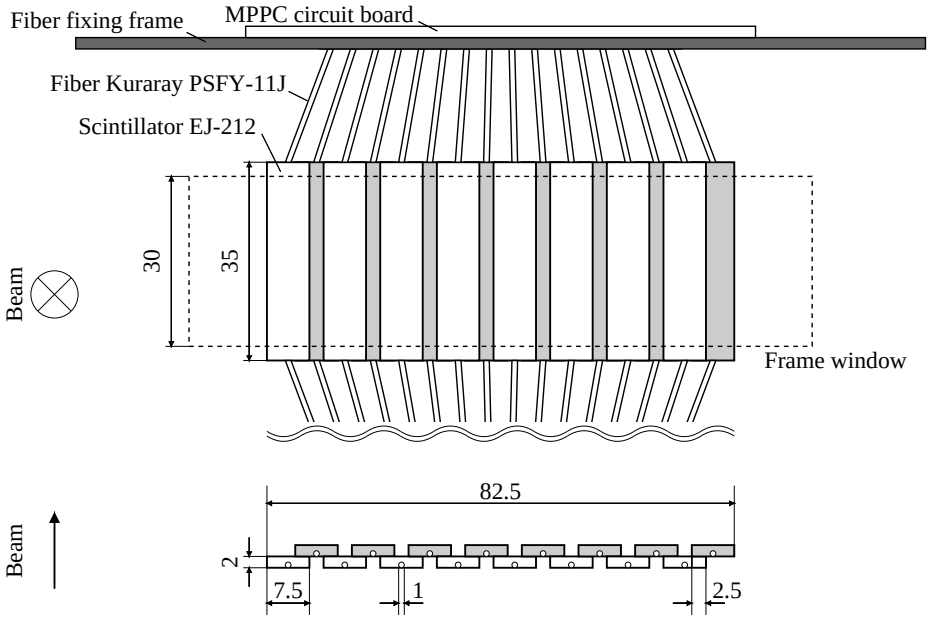

Figure 2.9: Schematic view of FBH.

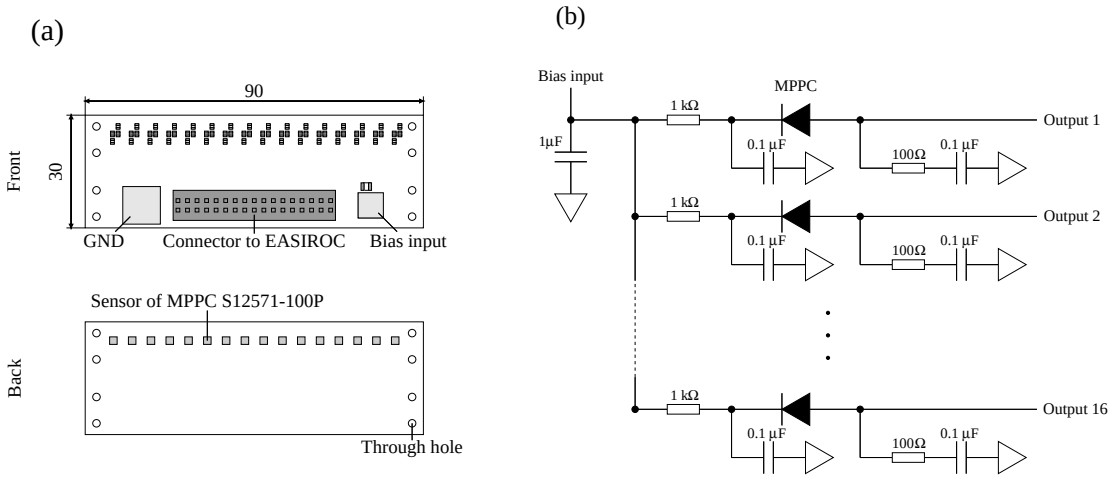

Figure 2.10: Schematic circuit of the MPPC circuit board.

For the multi-MPPC operation, we used a readout system with the EASIROC chips. Extended Analogue SiPM Integrated ReadOut Chip (EASIROC) has been developed by Omega group in

France [55]. The EASIROC provides necessary functions to operate MPPCs such as the digital to analog converter for bias adjustment, amplifiers, shapers and discriminators. Honda et al. developed the multi-MPPC readout electronics using EASIROC [56]. The module communicates with a computer via the TCP/IP protocol realized by SiTCP [57].

FBH was used as a component of a matrix coincidence trigger. The detail of the matrix trigger is described in Section 2.9.

2.4.2 Tracking detectors

Three tracking detectors were used for the measurement of the beam momentum. A beam fiber tracker (BFT) was placed at the entrance of the $QQDQQ$ system and two multi-wire drift chambers (BC3 and BC4) were at the exit. Table 2.3 and 2.4 list specifications of the tracking detecters of K1.8 beam line spectrometer. BFT had one plane and measured the horizontal position of each particle. The analysis procedure of the beam momentum reconstruction using BFT, BC3 and BC4 is described in Section 3.2.3.

Table 2.3: Specifications of BFT.

	Sensitive area (W×H [mm])	Scintillator	Photon detector (Hamamatsu Photonics K.K.)
BFT	160×80	Scintillation fiber ($\phi = 1mm$) Kuraray SCSF-78M	1×1 mm^2 MPPC: S10362-11-100P

Table 2.4: Specifications of BC3 and BC4.

	Sensitive area (W×H [mm])	Wire spacing [mm] Anode –Anode	Anode –Cathode	Orientation	Tilt angle [deg]
BC3	192×100	3	2	$xx'vv'uu'$	0, -15, 15
BC4	192×100	3	2	$uu'vv'xx'$	15, -15, 0

BFT

BFT (Beam Fiber Tracker) [58] is a finely segmented scintillation hodoscope placed at the entrance of the K1.8 beam line spectrometer. BFT consists of 320 cylindrical scintillation fibers with a diameter of 1 mm. The scintillation fibers are arranged in an alternate position with an overlap of 0.5 mm as shown in Figure 2.11. These fibers are fixed with holes of the fixing frame. The size of effective area was designed to be 160 mm (horizontal) × 80 mm (vertical) by considering the beam size at the BFT position. MPPCs (Hamamatsu S12571-100P) were connected on one end of each fiber and nothing on the other end. EASIROC was used for an operation of MPPCs and data aquisition in the similar scheme to that for FBH.

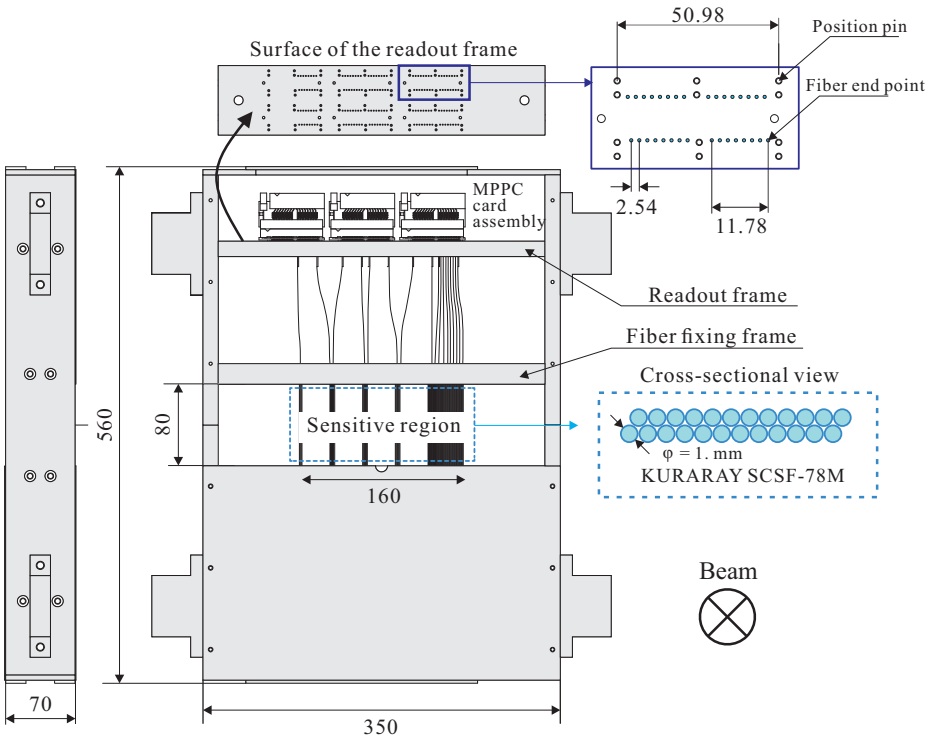

Figure 2.11: Schematic drawing of BFT.

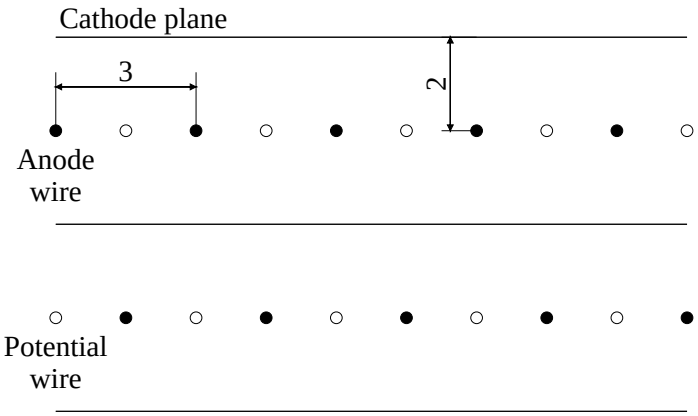

Figure 2.12: Schematic view of the pair plane of BC3 and 4.

BC3 and BC4

Two BCs (Beam Chambers), BC3 and BC4, were multi-wire drift chambers (MWDC) with an anode-anode spacing of 3 mm. The chambers had the same structure and arranged facing each other. They were installed at the exit of the K1.8 beam line spectrometer. Each chamber had six layers (xx', uu' and vv'), where wires in the u and v layers are tilted by 15° and -15°, respectively. A pair of two layers such as xx', uu' or vv' is called as a pair plane. In the pair plane, their wire positions are shifted by a half wire spacing as shown in Figure 2.12 to solve the left/right ambiguity of each hit. Anode wires consisted of gold-plated tungsten (Au-W) wires with a diameter of 12.5 μm. Gold-plated beryllium copper (Au-BeCu) wires with a diameter of 75 μm were used for potential wires. The cathode planes were carbon-coating Mylar films with thickness of 12 μm. 12.5-μm-thick aluminized Mylar films were attached on window frames. An anode-cathode spacing was 2 mm. Anode and potential wires had a tension of 20 g and 80 g, respectively. As for the gas, we mixed argon (Ar: 76%), iso-butane (C_4H_{10}: 20%) and dimethoxy-methane ($C_3H_8O_2$: 4%) at room temperature and 1 atm. Dimethoxy-methane, also called methylal, was mixed to prevent anode wires from sputtering caused by beam particles. The operation voltage of the cathode planes and the potential wires were -1.20 kV and -1.22 kV, respectively, for both BC3 and BC4. Amplifier-shaper-discriminator (ASD) chips were mounted on a readout card, which was attached to the chamber. The ASD chip was developed for the ATLAS experiment [59].

2.4.3 Collimator

The irradiatable track density in emulsion is limited to keep the transparency of the emulsion plate after the development. Therefore, the purity of K^- beam was essential for the experiment. In order to reduce the beam halo, we installed the 400-mm-long collimator made of tungsten-alloy blocks and lead blocks at the downstream of the Q13 magnet between BC3 and BC4 as shown in Figure 2.13. The gap was 30-mm high to fit the horizontal beam focusing.

2.5 Diamond target

The diamond was used to produce Ξ^- hyperons via the quasi-free $p(K^-, K^+)\Xi^-$ reaction. The forward angular cross section of the (K^-, K^+) reaction was measured to be proportional to $A^{0.38}$. The diamond also played the role of an energy degrader for the Ξ^- hyperons in order to bring them to rest in the emulsion module. The material with a small mass number and a high density was suitable to obtain a larger number of Ξ^- hyperon stopping events.

The diamond pieces were used as the experimental target, which was 9.869 ± 0.039 g/cm^2 in thickness. The size was 50.6-mm wide, 30.3-mm high and 30.4-mm thick. The volume and weight were 46.679 ± 0.225 cm^3 and 151.40 g, respectively. The density was calculated to be 3.243 ± 0.016 g/cm^3. The diamond target was located between FBH and SSD1. The target was fixed to a frame of FBH.

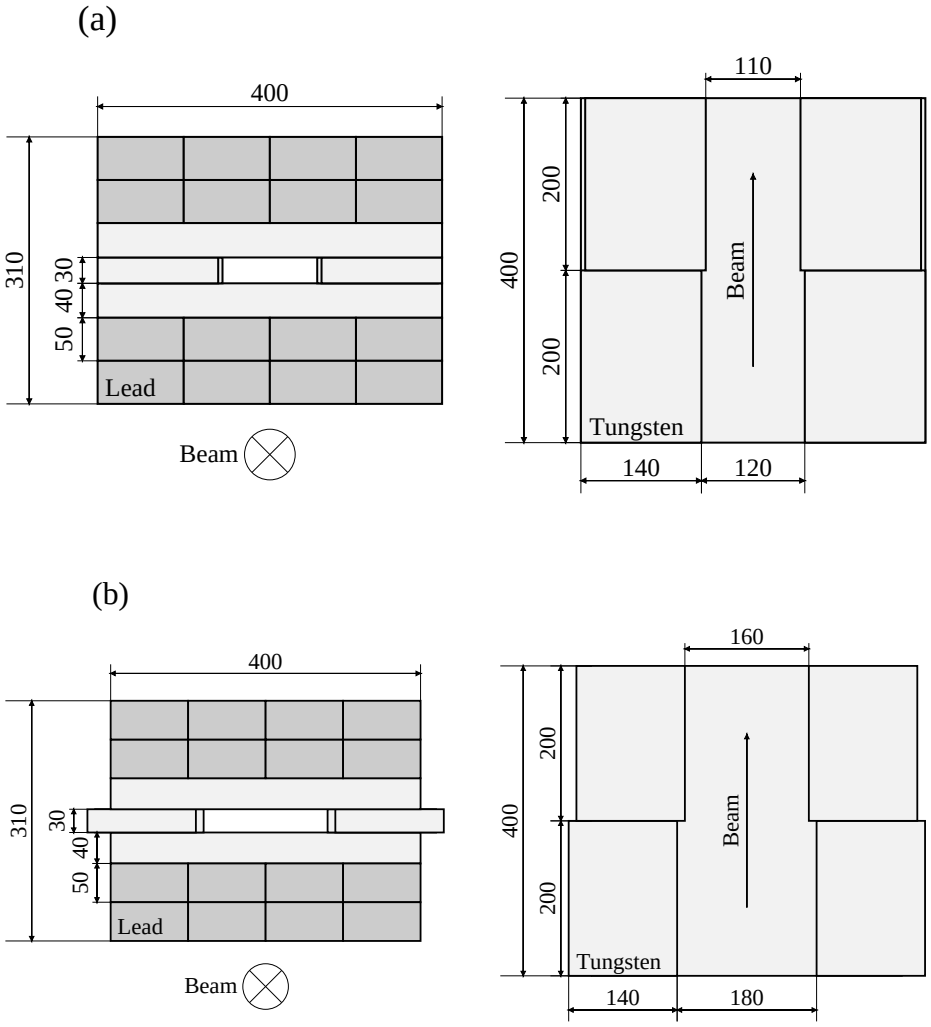

Figure 2.13: Schematic view of the collimator. (a) and (b) are for the run cycle of 2016 and 2017, respectively. Left shows the front view. Right shows the cross-sectional view. The squares of light gray and dark gray indicate tungsten-alloy blocks and lead blocks, respectively.

2.6 KURAMA spectrometer

The scattered K^+ produced via the (K^-, K^+) reaction was analyzed with downstream KURAMA spectrometer. Figure 2.14 shows a schematic view of KURAMA spectrometer. For analyzing the momenta of outgoing particles, we used a large acceptance spectrometer magnet, KURAMA. The size of the gap was 80-cm high, 100-cm wide, and 80-cm long. It was operated with the central magnetic field of 0.762 T. The momentum resolution of the spectrometer was $\Delta p/p = 2.8 \times 10^{-2}$ (FWHM). The acceptance was 280 msr. The spectrometer consisted of the KURAMA magnet, trigger counters (PVAC, FAC, SCH, and TOF), and five tracking detectors (SSD1, SSD2, SDC1, SDC2, and SDC3). Nuclear emulsion was placed downstream the target, between SSD1 and SSD2. Hyperball-X, X-ray detector, was installed upstream of the target to measure X-rays from Ξ atoms.

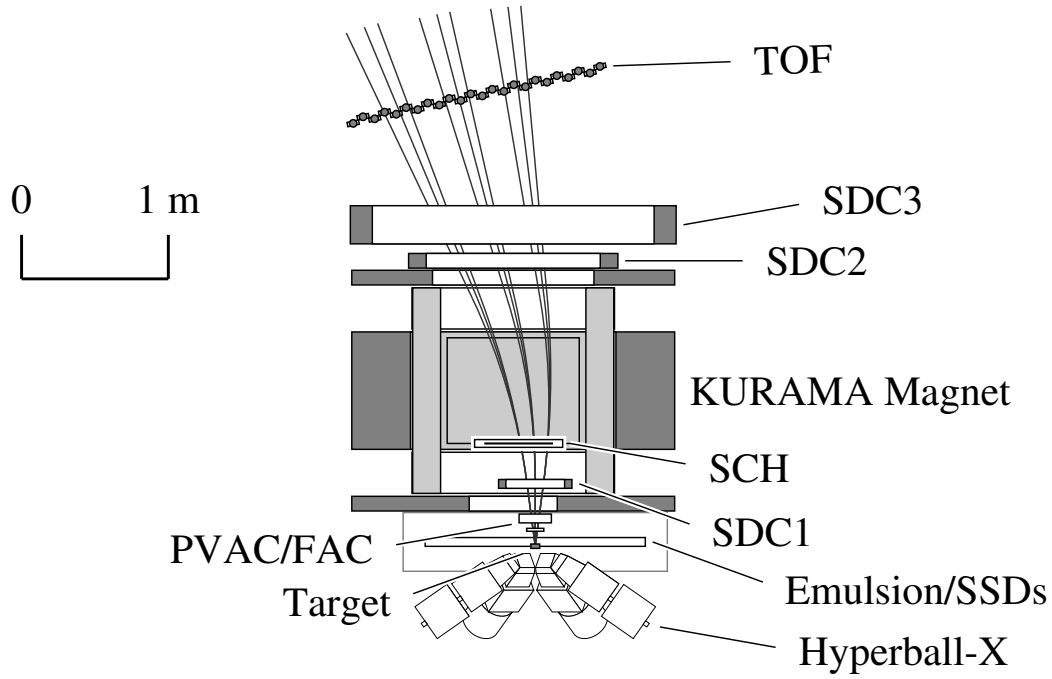

Figure 2.14: Schematic view of KURAMA spectrometer.

2.6.1 Trigger counters

Four trigger counters, PVAC, FAC, SCH, and TOF, were installed in KURAMA spectrometer. Table 2.5 lists specifications of the trigger counters of KURAMA spectrometer.

PVAC and FAC

PVAC (Proton Veto Aerogel Čerenkov counter) is a threshold-type silica aerogel Čerenkov counter for the veto on protons in scattered particles. PVAC was installed at an entrance of KURAMA magnet in front of the upstream end guard. Silica aerogel plates with the index of 1.12 were used for PVAC. The sensitive area was 117-mm wide and 117-mm high. Four fine-mesh phototubes

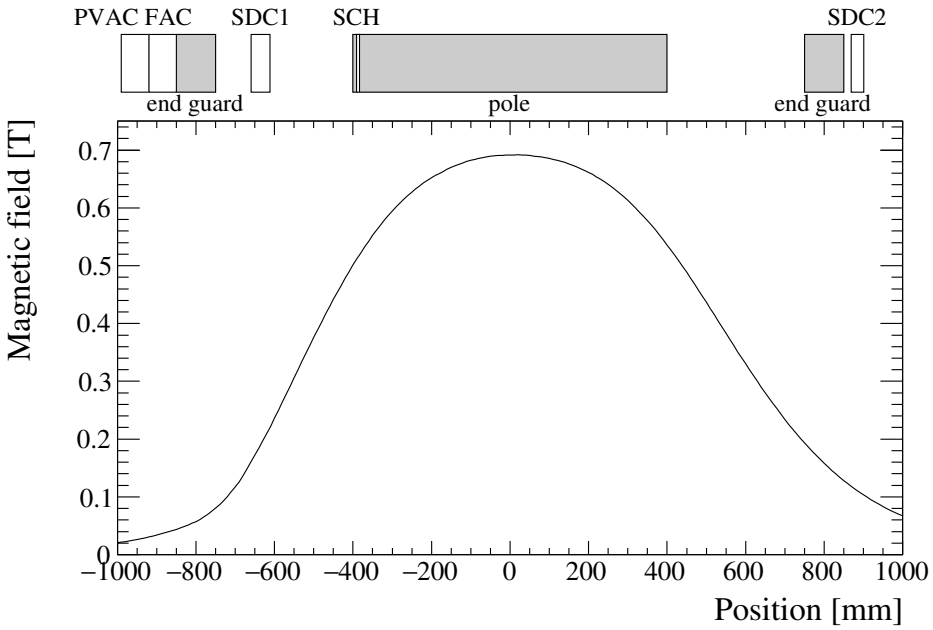

Figure 2.15: Magnetic field of KURAMA magnet. Field strength of Y-direction (vertical) along the beam direction at X=0, Y=0. The position of detectors are illustrated above the histogram.

Table 2.5: Specifications of trigger counters of KURAMA spectrometer.

	Sensitive area (W×H×T [mm])	Scintillator/Radiator	Photon detector (Hamamatsu Photonics K.K.)
PVAC	$117 \times 117 \times 14$	Silica aerogel ($n = 1.12$)	$2.5''$ PMT: R6682
FAC	$225 \times 162 \times 60$	Silica aerogel ($n = 1.05$)	$2.5''$ PMT: R6682
SCH	$673 \times 450 \times 2$	Plastic scintillator: EJ-212	1×1 mm^2 MPPC: S10362-11-100P
TOF	$1805 \times 1800 \times 30$	Plastic scintillator: EJ-210	$2''$ PMT: H1949

(Hamamatsu R6682) in total were connected on both top and bottom sides. On the inner surfaces, teflon sheets were attached as a diffusive reflector to guide a Čerenkov light toward phototubes. Four analog signals of phototubes were mixed with an analog mixer (ORTEC AN308/NL). The momentum threshold of kaons and protons are 0.98 and 1.86 GeV/c as shown in Figure 2.8. The detection efficiencies were obtained to be 99.4% and 99.4% for pions and kaons, respectively.

FAC (Forward Aerogel Čerenkov counter) was placed at just downstream of PVAC to select scattered kaons in the trigger level. FAC consists of silica aerogel plates with the index of 1.05. The sensitive area was 220-mm wide and 180-mm high. Six fine-mesh phototubes (Hamamatsu R6682) in total were connected on both top and bottom sides. Teflon sheets were attached on the inner surfaces in the same way as PVAC. All six analog signals of phototubes were mixed and sent to the trigger logic. The momentum threshold of kaons is 1.54 GeV/c. The detection efficiency was obtained to be 99.4% for beam kaons.

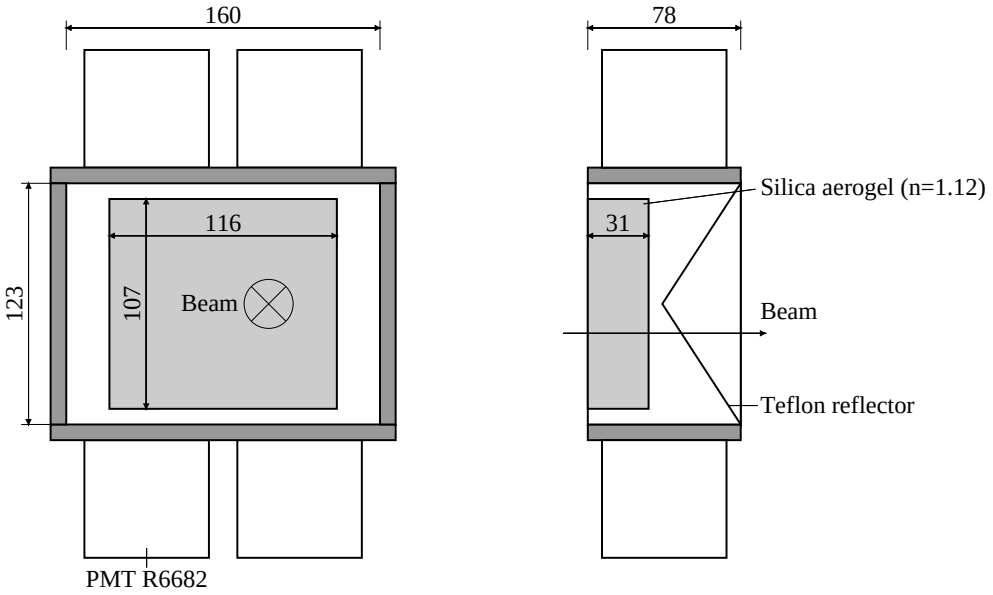

Figure 2.16: Schematic view of PVAC.

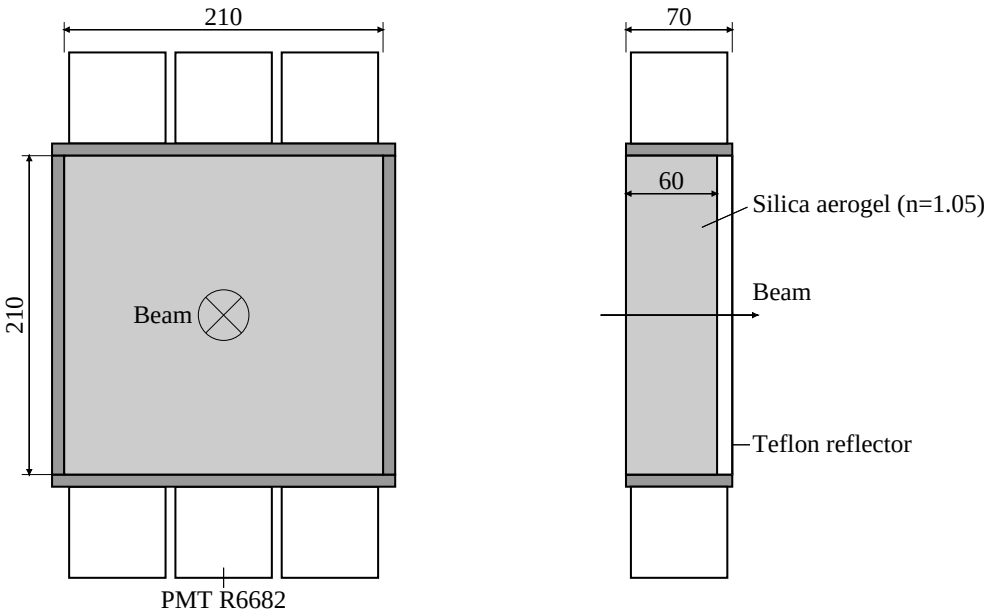

Figure 2.17: Schematic view of FAC.

SCH

SCH (Scattered Charge Hodoscope) is composed of 64 plastic scintillators (Eljen Technology EJ-212) with 2-mm thickness. The scintillator size was 11.5-mm wide and 450-mm high. SCH was segmented into sixty-four and overlapped with the next segments by 1 mm as shown in Figure 2.18. A wavelength shifting fiber (Kuraray PSFY-11J) with a diameter of 1 mm is fixed in a groove on each scintillator. The scintillator and fiber were wrapped by teflon sheets. The size of a sensitive area is 673-mm wide and 434-mm high. Since SCH was installed in KURAMA magnet, MPPC readout system was adopted to operate in the magnet field. Four MPPC circuit boards were connected on a top end of the fiber, where sixteen MPPCs (Hamamatsu S10362-11-100P) were surface-mounted on each board. Figure 2.19 shows a schematic layout of the MPPC circuit board. An electric circuit of the board was the same as that of the FBH in Figure 2.10. For the multi-MPPC operation, we used an EASIROC readout system. SCH was one element of a matrix coincidence trigger. The detail of the trigger is described in Section 2.9.

TOF

TOF (Time-Of-Flight wall) was placed at the most downstream in the KURAMA spectrometer in order to measure the time-of-flight from BH2 to TOF. Figure 2.20 shows a schematic drawing of TOF. TOF consisted of 24 bars of plastic scintillator (Eljen Technology EJ-200) with the thickness of 30 mm. The scintillator size was 80-mm wide and 1800-mm high. Scintillating lights were detected with phototubes (Hamamatsu H1949) which were connected on both ends through acrylic light guides. TOF was placed to be horizontally rotated 12 degrees to optimize the acceptance as shown in Figure 2.14. The typical timing resolution between BH2 and TOF was 150 ps (σ) for protons.

2.6.2 Tracking detectors

SSD1 and SSD2

Two SSDs (Silicon Strip Detectors) were used to reconstruct vertex positions and tracks of particles with high precision. Since SSD was an essential detector for the hybrid emulsion–counter method, SSD had been studiously developed [60, 61]. We installed two SSDs, called SSD1 and SSD2, to interpose emulsion. SSD1 was located between the target and emulsion to measure the positions and angles of Ξ^- hyperons produced at the target. We also used SSD1 to measure tracks of scattered kaons. SSD2 was placed at the downstream position of emulsion to measure the positions and angles of particles passing through emulsion. SSD1 and SSD2 had the same strip pitch of 50 μm. The thickness was 320 μm. Both sensitive areas were 76.8-mm wide and 76.8-mm high. The specification is listed in Table 2.6.

The silicon sensor is single-sided and a p-in-n type manufactured by Hamamatsu Photonics. Each SSD had four layers of silicon sensors stacked on a circuit board in the directions of x–y–x–y in order to put them together as close as possible. The flight path length of Ξ^- hyperons was necessary to be short for reduction of the decay probability. Considering the trade off relation between the decay probability and the angular resolution, SSD1 had a closer structure than SSD2 as shown in Figure

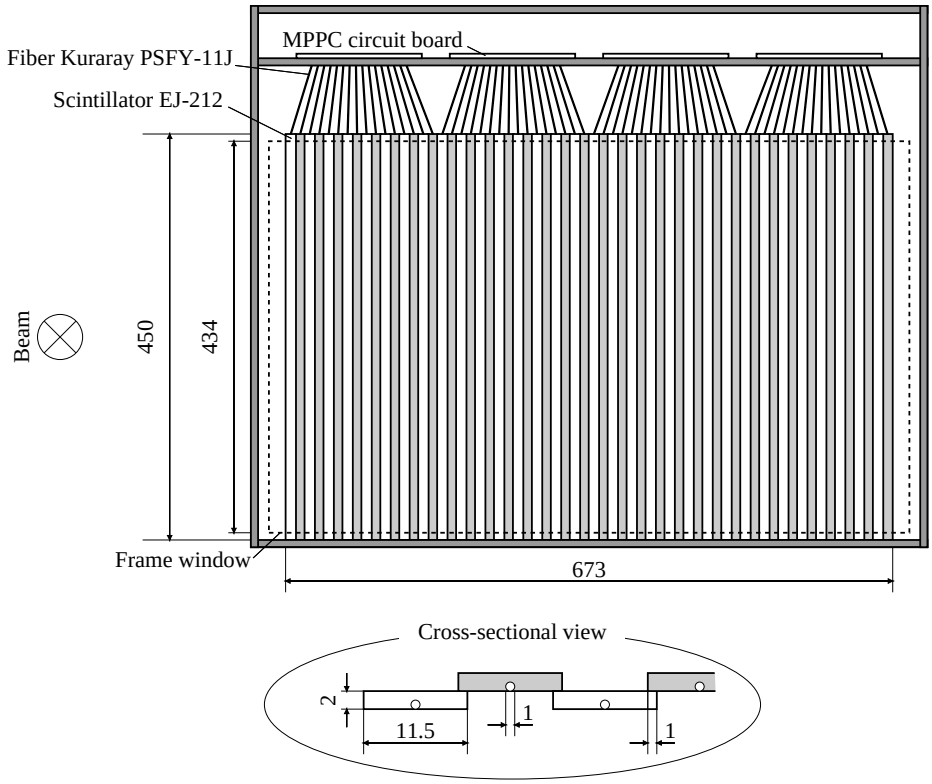

Figure 2.18: Schematic view of SCH.

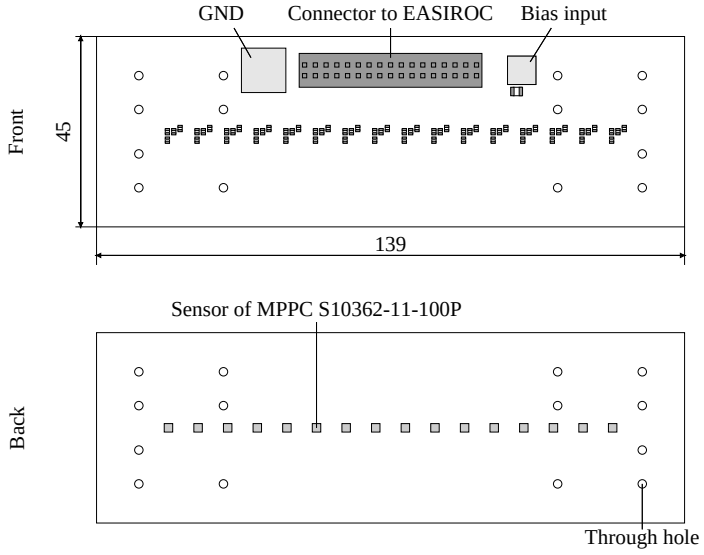

Figure 2.19: Layout of MPPC circuit board of SCH.

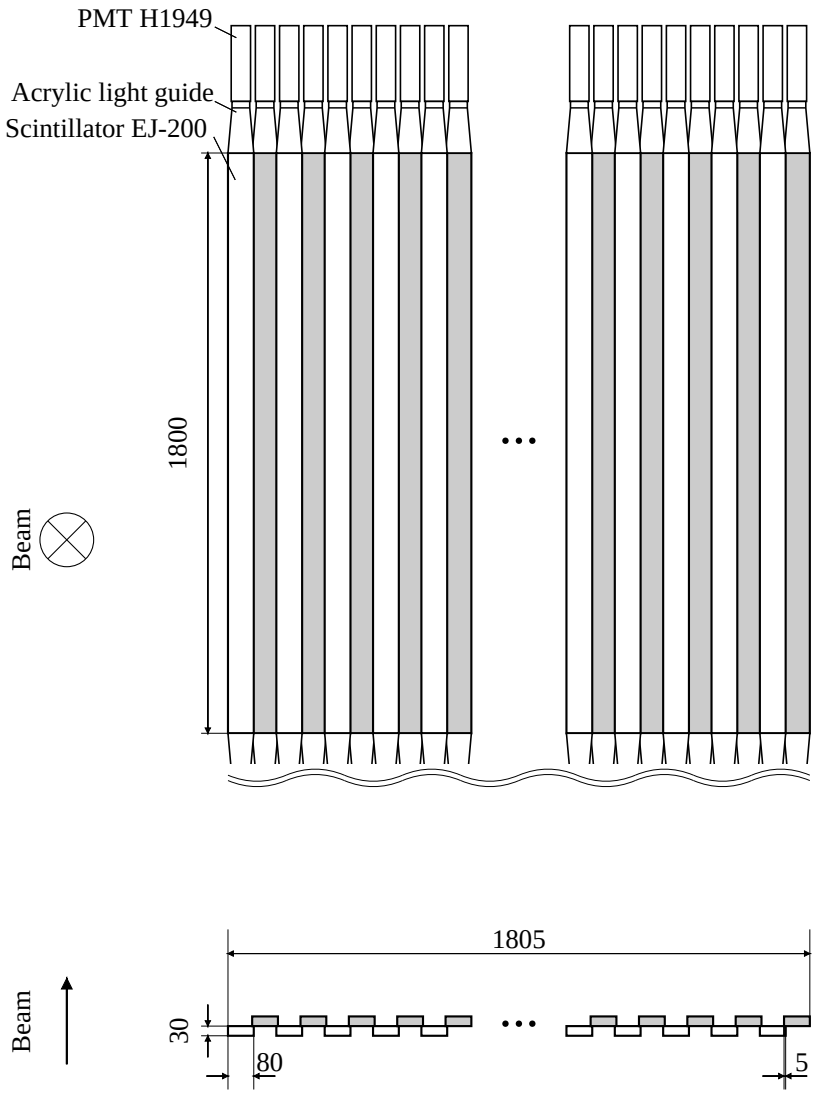

Figure 2.20: Schematic drawing of TOF.

2.21. The distance between layers was 500 μm for SSD1 and SSD2. Only the distance between y and x' layers was 1000 μm for SSD2. The bias voltage of 80 V was applied for all layers of SSD1 and SSD2.

The front-end readout chips (APV25-s1 [62]) received signals from silicon sensor strips. The chips processed and transferred the analog data to APVDAQ VME modules via a network. Since the data was distorted due to the length of the Ethernet cables, we applied the finite impulse response filter (FIR Filter [63]) to recover the data structure. Furthermore, a zero-suppression logic was implemented in APVDAQ module to reduce the size of the data to be transferred.

In the experiment, the emulsion module was moved near SSDs. Therefore, the noise level of SSDs often changed during the emulsion exposure. The noise level strongly affected the efficiency of the data acquisition. The zero-suppression threshold was frequently adjusted to keep both the detection and data acquisition efficiency. The detection efficiency was kept to be more than 97%.

Table 2.6: Specifications of SSD1 and SSD2

	Sensitive area (W×H [mm])	Strip pitch [mm]	Orientation	Tilt angle [deg]
SSD1	76.8×76.8	0.05	$yxy'x'$	90, 0, 90, 0
SSD2	76.8×76.8	0.05	$xyx'y'$	0, 90, 0, 90

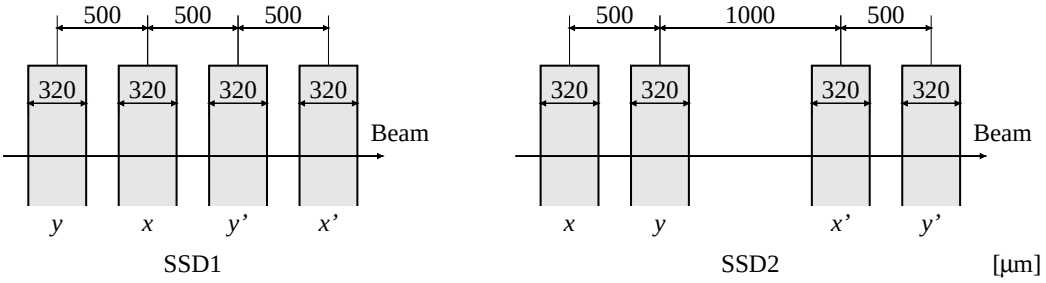

Figure 2.21: Cross-sectional layout of the sensor plane of SSD

SDC1, SDC2 and SDC3

We used three SDCs (Scattered Drift Chambers) in the KURAMA spectrometer. Since scattered particles came into the chambers with an angle, the honeycomb structure of drift cells was preferred to the planar structure. Figure 2.22 (a), (b) and (c) show schematic drawings of SDC1, SDC2 and SDC3, respectively. Each anode wire was surrounded by six potential wires forming a hexagonal cell structure. Two planes of shield wires were perpendicular to the anode wires. Three SDCs all had the pair plane structure.The specification is listed in Table 2.7.

Table 2.7: Specifications of tracking detecters of KURAMA spectrometer

	Sensitive area (W×H [mm])	Wire spacing [mm] Anode -Anode	Anode -Cathode	Orientation	Tilt angle [deg]
SDC1	384×264	6	2	$vv'xx'uu'$	15, 0, -15
SDC2	1152×1152	9	2	$xx'yy'$	0, 90
SDC3	1920×1280	20	2	$yy'xx'$	90, 0

SDC1 had six layers ($vv'xx'$ and uu'), where wires in the u and v layers are tilted by 15° and -15°, respectively. Anode wires consisted of gold-plated tungsten-rhenium (Au-W/Re) wires with a diameter of 20 μm. Gold-plated aluminum (Au-Al) wires with a diameter of 80 μm were used for potential and shield wires. Anode, potential and shield wires had a tension of 50 g, 80 g, and 80 g, respectively. For SDC1, we used the same mixed gas as BC3 and BC4. The operation voltage of the potential and shield wires were -1.6 kV.

SDC2 consisted of four layers (xx' and yy'). Anode wires consisted of gold-plated tungsten (Au-W) wires with a diameter of 20 μm. The potential and shield wires were gold-plated aluminum (Au-Al) wires with a diameter of 100 μm. Anode, potential and shield wires had a tension of 40 g, 80 g and 80 g, respectively. The gas was a mixture of 50% argon and 50% ethane. The voltage for the potential and shield wires were -2.05 and -1.5 kV, respectively. The detail was also described in

Ref [64] as named W3-W5.

SDC3 was also composed of four layers (yy' and xx'). Anode wires were made of gold-plated tungsten (Au-W) wires with a diameter of 30 μm. The potential and shield wires gold-plated beryllium copper (Au-BeCu) wires with a diameter of 50 μm. Anode, potential and shield wires had a tension of 100 g. The same gas mixture as SDC2, 50% argon and 50% ethane, was used for SDC3. The voltage for the potential and shield wires were -2.6 and -1.5 kV, respectively.

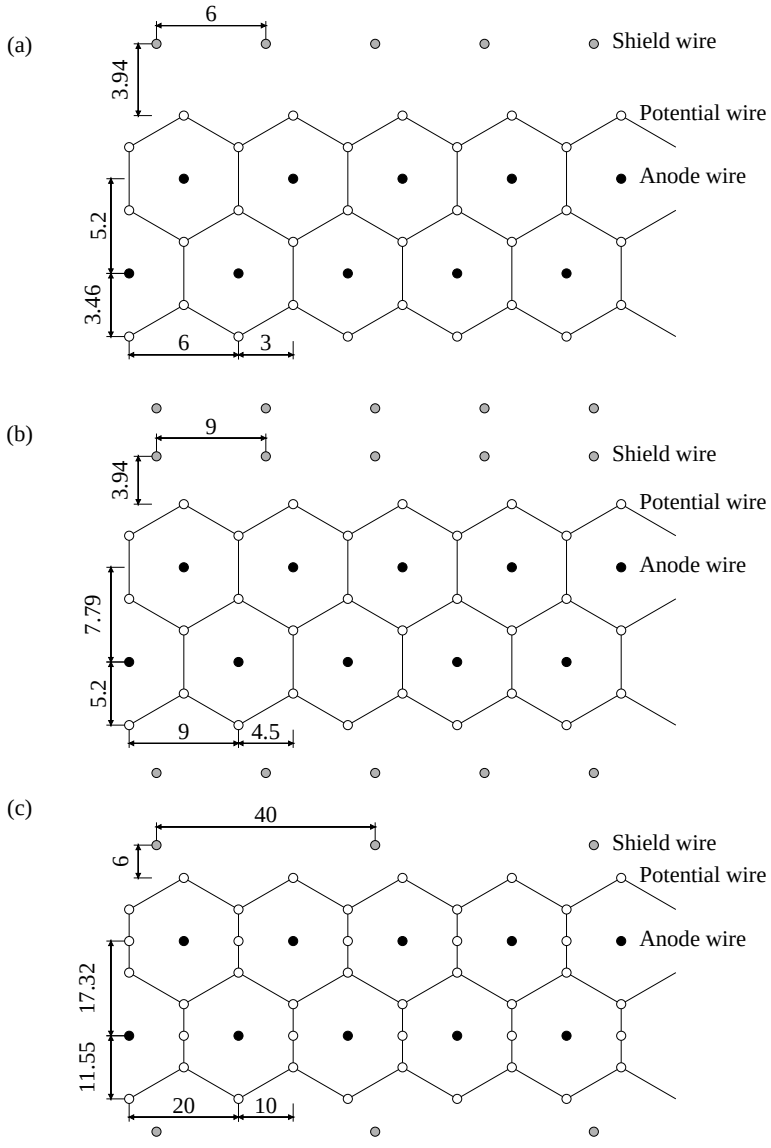

Figure 2.22: Schematic drawing of the pair plane of SDC3. (a), (b) and (c) show drawings of SDC1, SDC2 and SDC3, respectively.

2.7 Nuclear emulsion

An emulsion module consisted of two thin-type sheets and eleven thick-type sheets with 34.5 × 35.0-cm^2 area. Figure 2.23 illustrates the constitution of an emulsion module and the layout around the diamond target. Since the most upstream sheet was used to connect Ξ^- hyperon tracks from SSD1, it was necessary to minimize the distortion or deformation of the emulsion sheet. Therefore, a thin-type sheet was placed upstream followed by eleven thick-type sheets. The most downstream sheet was also used to connect tracks to SSD2 if decay daughters of hyperfragments go out from an emulsion module. The thin-type sheet was located in the most downstream part of an emulsion module. The thin-type sheet had 100-μm-thick emulsion layers on both sides of a 180-μm-thick polystyrene base film. The thick-type sheet had 480-μm-thick emulsion layers on both sides of a 40-μm-thick polystyrene base film.

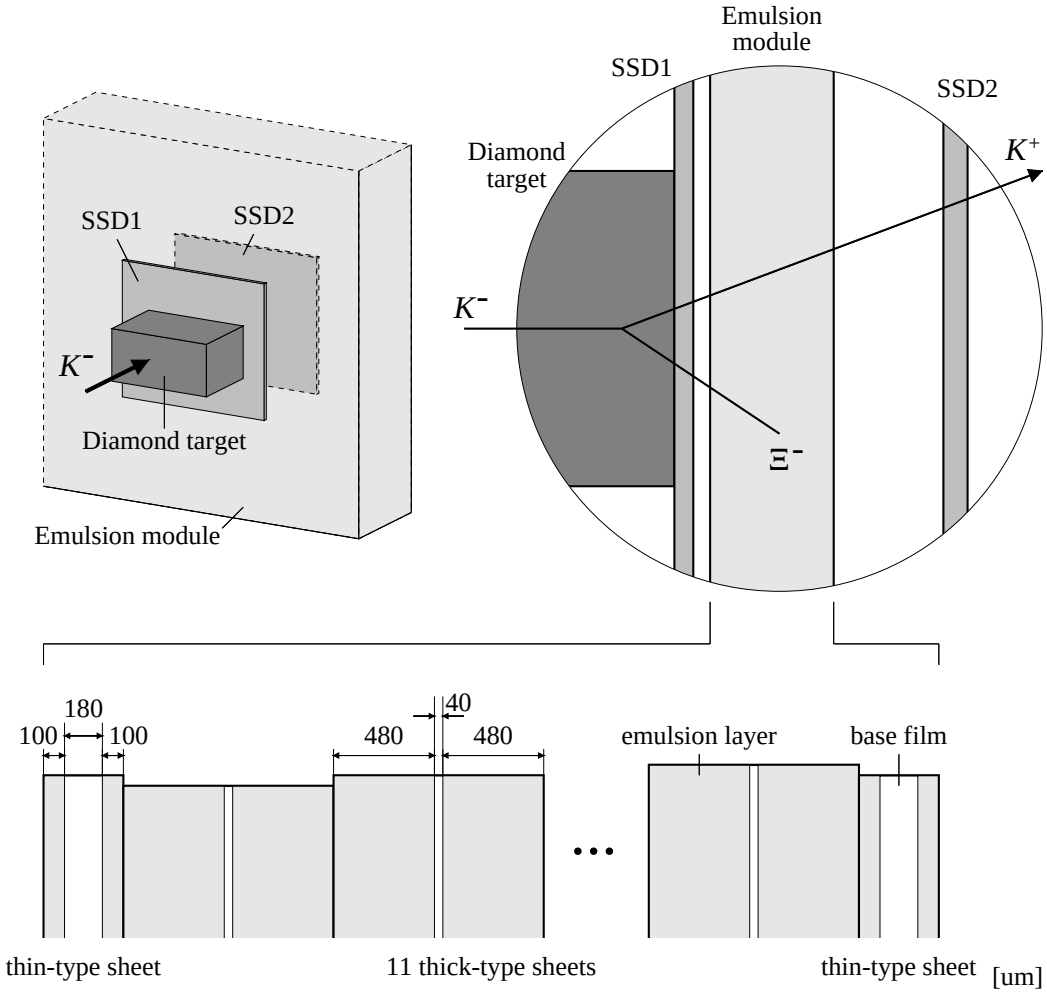

Figure 2.23: Schematic illustration of the emulsion module and the vicinity.

The emulsion gel developed by Fuji-film, called Fuji GIF, was used. The size of AgBrI crystals was 0.2 μm in the Fuji GIF emulsion. The design value of weight ratio of Ag to gelatin was 3.16.

The typical density was 3.53 g/cm^3. Table 2.8 lists the composition of the Fuji GIF emulsion. Since the values in Table 2.8 were the calculation, the actual constitution depended on the situation such as water content. All emulsion sheets were produced in Gifu University. The base film was coated with an emulsion on one side at first. After drying the emulsion gel, the other side was coated and dried in the same manner. The emulsion sheets were cut into four sheets with the size of 34.5 $\times$ 35.0-cm^2. The total amount of emulsion was 118 modules in total, whose 238 thin-type sheets and 1298 thick-type sheets were exposed to beams.

Table 2.8: Design value of the composition of the Fuji GIF emulsion. The actual constitution depended on the water content.

Material	Density [g/cm^3]
H	0.05
C	0.326
N	0.11
O	0.23
Br	1.166
Ag	1.60
I	0.033
others	0.015

An emulsion module was packed in a stainless vacuum chamber, Emulsion cassette, in order to keep the flatness and the relative positions between the emulsion sheets during the experiment. Figure 2.24 shows the schematic drawing of the emulsion cassette. An upstream surface of the cassette was sealed with a 100-μm-thick stainless foil. Since it was necessary to uniformly irradiate the whole area of the emulsion with a track density of 10^6 tracks/cm^2, an emulsion mover system was developed. Duration of the beam extraction was around 2 seconds in every 5.52 seconds in the experiment. The emulsion module was moved the distance, which was according to the beam intensity, by the emulsion mover during off-spill. Although the detail is described in Section 4.2.3, the pattern matching method was used to align the emulsion module and SSD with $\overline{p}$ beam. Since the irradiation areas for the pattern matching were four corners of the emulsion module, the emulsion module was moved to keep out of the corners. The emulsion mover was controlled with a Linux PC having control boards. The position of the emulsion module was measured with linear encoders in horizontal and in vertical. The accuracy was 10 μm.

2.8 Germanium detector array - Hyperball-X

Hypernuclear γ spectroscopy has recently been developed. A germanium detector array, called Hyperball, was constructed in 1998. Hyperball was used to observe hypernuclear γ transitions. We installed Hyperball-X, upgraded Hyperball, around the target to detect Ξ^- atomic X-rays, when stopped Ξ^- events are clearly identified with the emulsion analysis. Hyperball-X was unused in this thesis.

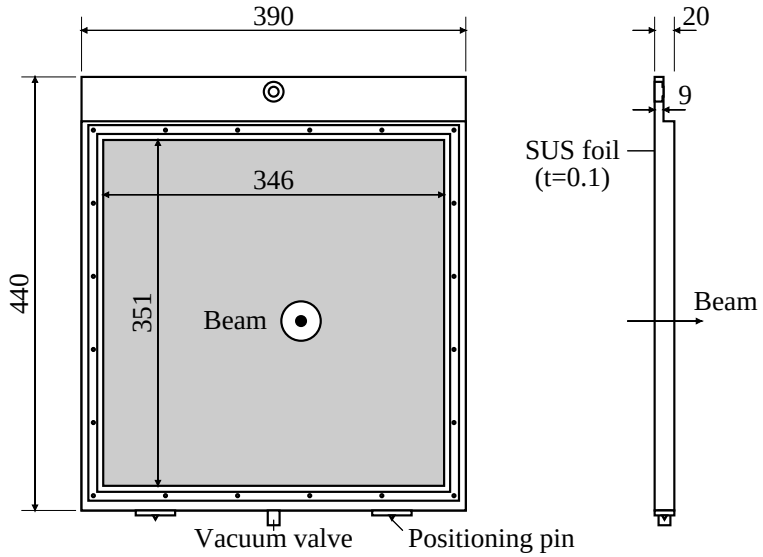

Figure 2.24: Schematic drawing of the emulsion cassette.

2.9 Trigger

A (K^-, K^+) reaction trigger was composed of hit information of the plastic scintillators and the aerogel Čerenkov counters. The trigger was comprised of a K^- beam part, a scattered K^+ meson part, and a matrix coincidence part. Figure 2.25 shows the logic diagram of the (K^-, K^+) reaction trigger. The K^- beam part was defined as

$$KBEAM \equiv BH1 \times BH2 \times \overline{BAC1} \times \overline{BAC2}. \tag{2.1}$$

Using mean timer modules, the timing of BH1 and BH2 was made to be independent of the hit positions. Since beams with negative charge were transported, contamination of K^- beams was mainly π^- mesons. Since the difference of their time-of-flight was only 1.2 ns at the beam momentum of 1.81 GeV/c, BAC1 and BAC2 discriminated the incident K^- beam by using as a veto. The scattered K^+ part was defined as

$$KSCAT \equiv PVAC \times \overline{FAC} \times TOF. \tag{2.2}$$

Mean timer modules were also used for TOF. Scattered protons and non-interacting beam particles were rejected with discrimination of PVAC and FAC, respectively. The matrix coincidence trigger joined the (K^-, K^+) reaction trigger for more efficient selection. The (K^-, K^+) reaction trigger was defined as

$$KK \equiv KBEAM \times KSCAT \times MATRIX. \tag{2.3}$$

where, $MATRIX$ was the matrix coincidence trigger.

In addition, other triggers were mixed such as $UNBIASED \equiv BH1 \times BH2 \times TOF$ and $KPI \equiv BH1 \times BH2 \times PVAC \times FAC \times TOF$. Such triggers were used for calibration. All the trigger timing was determined with the BH2 timing.

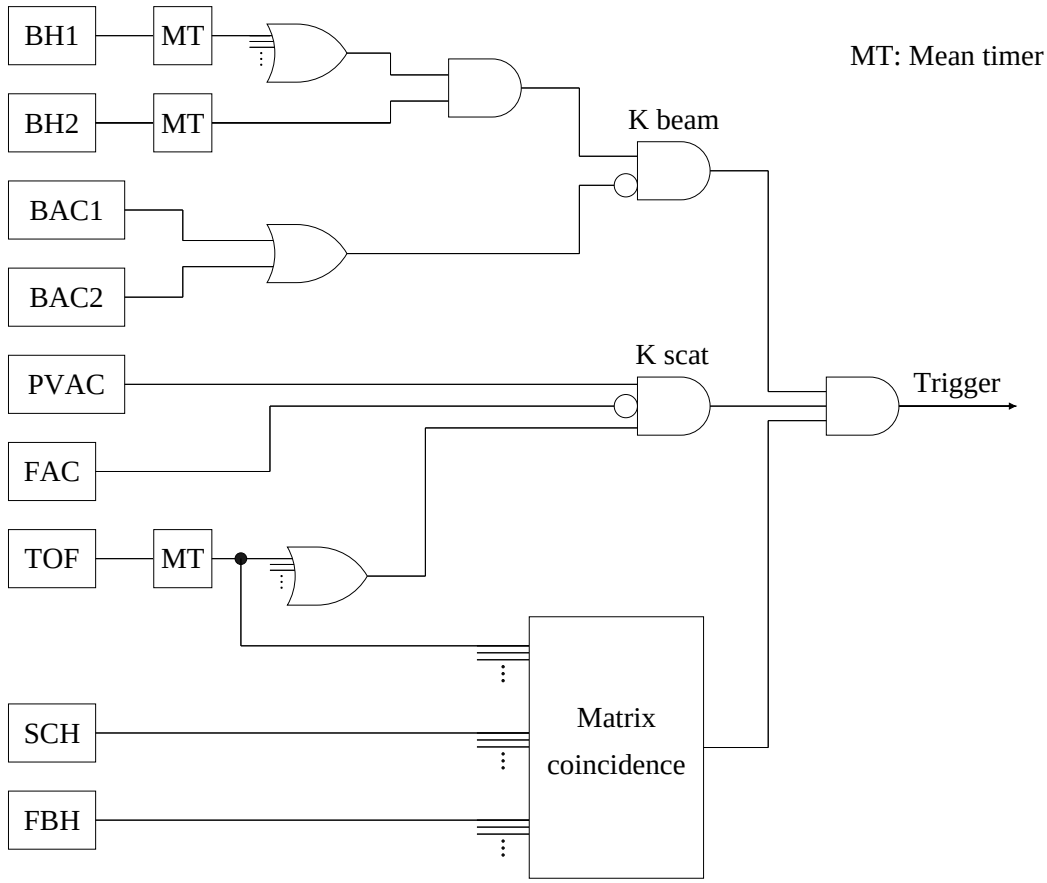

Figure 2.25: (K^-, K^+) reaction trigger logic diagram.

Matrix coincidence trigger

To efficiently select (K^-, K^+) reaction events, the matrix coincidence trigger was essential. The matrix consisted of hit signals of three detectors, FBH, SCH, and TOF. Since a K^- beam passed through all trigger counters, (K^-, K^+) reaction events selected with a trigger of $KBEAM \times KSCAT$ had many background events induced by the beam. Figure 2.26 shows the diagram of the trigger logic. For a reduction of the trigger rate, we used two kinds of matrix patterns. One was a two-dimensional matrix coincidence, which selected the scattered particles using SCH and TOF. The other was a three-dimensional matrix coincidence, which rejected the beam particles using FBH, SCH and TOF. The matrix coincidence trigger was defined as

$$MATRIX \equiv MATRIX2D \times \overline{MATRIX3D}, \tag{2.4}$$

where $MATRIX2D$ and $MATRIX3D$ were the two-dimensional and three-dimensional matrix coincidence trigger, respectively.

HUL (Hadron Universal Logic) is a newly developed and general purpose logic module [65, 66]. The logic of the matrix coincidence trigger was developed with an FPGA (Kintex-7 160T-1FBG676) on HUL. Each detector signal was synchronized by the 200 MHz system clock. The mean-timer output signals were used for inputs of TOF. In the case of FBH, both up and down signals were sent

as the inputs. A coincidence between the up and down signals was made inside FPGA. The signals were clustered with the neighbor segments after making the coincidence. Therefore, the signals of FBH was segmented into thirty-one. In total, the numbers of matrix elements were 24 × 64 (1536) for $MATRIX2D$ and 24 × 64 × 31 (47616) for $MATRIX3D$. Matrix elements were set via SiTCP. The relative timing among three detectors was also adjusted in HUL. We selected the scattered K^+ trigger with $MATRIX2D$ while rejecting the K^- beam trigger with $MATRIX3D$ veto.

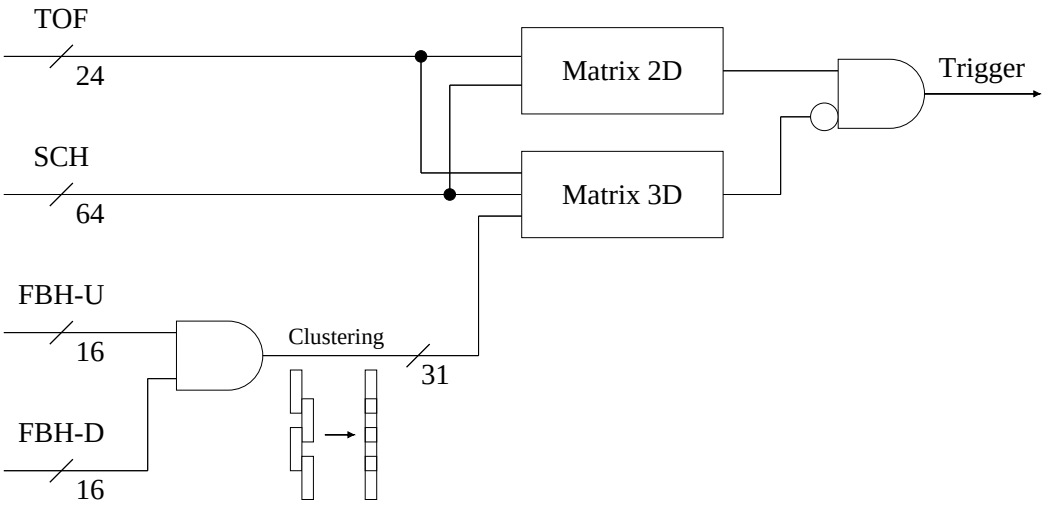

Figure 2.26: Logic diagram of the matrix coincidence trigger.

Figure 2.27 shows a hit pattern of SCH and TOF segments without the matrix coincidence trigger. The blue line indicates the veto region, which was made by hits of non-interacting beams. The accepted region is indicated in red lines, where the region was determined so as to save the positively charged particles with momentum of 0.9-1.5 GeV/c. The veto region shows the case of a representative segment of FBH.

2.10 Data aquisition system

Various readout modules such as a conventional VME, COPPER, EASIROC and HUL, were used in a data aquisition (DAQ) system of the experiment. Such subsystems were managed and integrated by a network-based software, Hadron DAQ (HDDAQ). The network is one of the most common way to communicate among electronic devices. Data from each subsystem were gathered through network interfaces with TCP/IP protocol. However, since the network is an asynchronous communication, the event synchronization becomes an issue. Therefore, we adopted a trigger managing system with a master trigger module (MTM) and a receiver module (RM) [67]. The trigger managing system distributed an event tag to each subsystem. Figure 2.28 illustrates the entire scheme of the DAQ system. The data transfer was performed for each event.

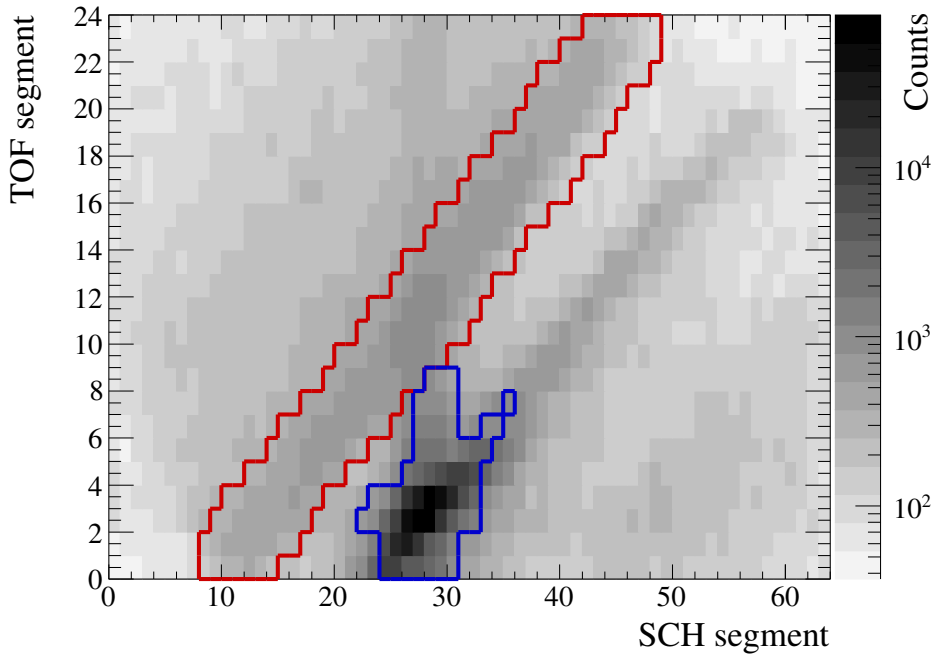

Figure 2.27: Hit combination of TOF and SCH segments. The red and blue lines indicate the accepted and rejected regions, respectively. The veto region shows the case of a representative segment of FBH.

2.10.1 Trigger managing system

The trigger managing system consisted of MTM and RM. For a control of the DAQ system, MTM managed signals such as a trigger, a busy and an event tag. These signals were distributed using twisted pair cables (Ethernet cables) between MTM and RM of subsystems. The trigger was used for a gate of ADC and start/stop timing of TDC. MTM transmitted the trigger in a spill gate and a DAQ gate while the busy was off. The length of the spill gate was 2.41 s, which covered the beam-extraction time. The DAQ gate was asserted and deasserted with DAQ Controller. During taking the data, the DAQ gate was always true. The busy signals were asserted by the subsystems and merged for a mask of the trigger on MTM. The event tags were decoded and added to the data as an event number in RM. The consistency of the event numbers of all subsystems was monitored.

2.10.2 DAQ subsystem

As the DAQ subsystem, we constructed VME, COPPER, EASIROC, and HUL subsystems in the experiment. All subsystems transmitted the data to the main DAQ server with the network for each event.

VME

Three VME subsystems participated in the DAQ system. One was for signals of BH1, BH2, BAC, PVAC, FAC, and TOF. VME modules of ADC (CAEN V792) and TDC (CAEN V775) were used

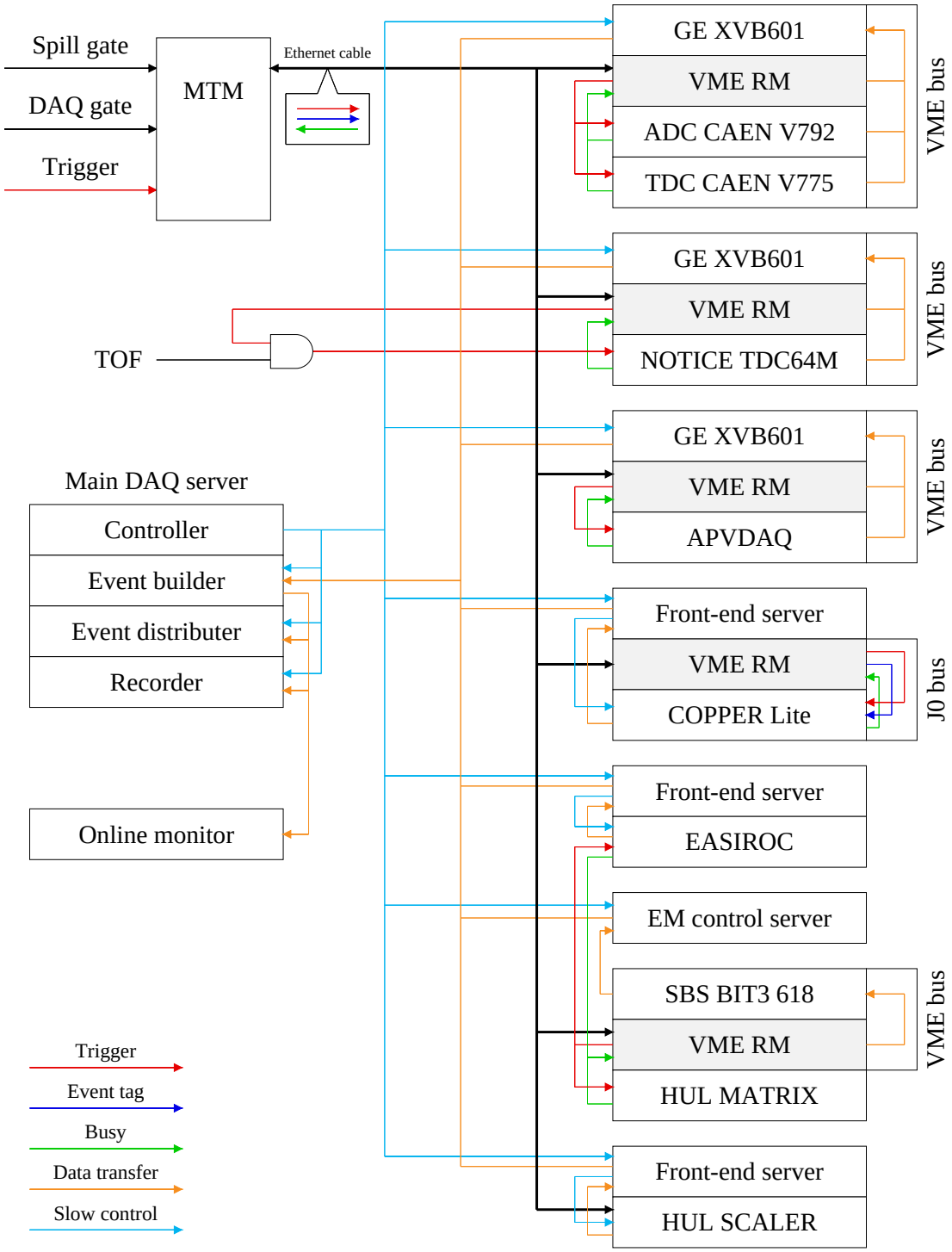

Figure 2.28: Overview of the data acquisition system.

to read the signals. Timing information of SDC2 and SDC3 was taken with multi-hit TDC (Notice TDC64M). Since the timing depends on a path length and momentum of the scattered particle, the common stop signal was made by TOF. The other subsystem was for readout of SSD. The subsystem consisted of APVDAQ, which was a special VME module developed by HEPHY. The analog signal was digitized to a 10-bit Flash-ADC in the APV25-s1 chip. The digitized data were transferred to APVDAQ. In order to reduce the data size, the zero-suppression, and double-buffer logic were implemented in the FPGA. The on-board CPU VME controller, GE XVB601, transmitted the data in each subsystem.

COPPER

Timing information of BC3 and SDC1 was digitized by the FINESSE multi-hit TDC installed in the COPPER modules. COPPER (COmmon Pipe-lined Platform for Electronics Readout) [68] was a module for the KEK-VME specification that realizes various types of analog-to-digital conversion and pipelines digital data processing functions in a unified scheme. We used the COPPER-Lite whose CPU was replaced with a SiTCP. The MHTDC module encoded the timing information with an accuracy of 1 ns. COPPER works on a platform of 9U KEK-VME crate. KEK-VME is a local extension of the VME bus standard with additional power supplies and timing lines [67]. Trigger information was exchanged between VME-RM and COPPER through the J0 bus.

EASIROC

Using EASIROC module, timing information of BFT, FBH, and SCH was taken by MHTDC implemented in the FPGA (Xilinx SPARTAN6), whose the least significant bit was programmed to be 1 ns.

HUL

We took the timing data of the matrix coincidence trigger using HUL. Furthermore, we used the other HUL module, where the scaler was implemented in FPGA. The HUL module acquired the scaler values of trigger counters and coincidences such as $KBEAM$, $KSCAT$, KK and so on.

2.10.3 Hadron DAQ

The data acquisition was operated using Hadron DAQ (HDDAQ), which was a network-based DAQ software [67]. HDDAQ consisted of the following DAQ components, Event Builder, Event Distributor, Recorder, and Front-end. Each component had two kinds of paths for the data transfer and the slow control. The front-end read data from each readout electronics, and transmitted them to the Event Builder. The Event Builder collected data from all front-ends, and built an event for each event. The built event was transmitted to the Event Distributor. The Event Distributor was a server to distribute the data to clients such as the Recorder and online monitors. The Recorder received the event packets without any loss while the others received the packets as far as they can. The Recorder stores the data to the storage devices with compression. A Front-end process ran

in each DAQ subsystem. The processes of DAQ Controller, Event Builder, Event Distributor, and Recorder were operated in the main DAQ server.

In the experiment, the dead time of the DAQ process was typically 110 μs while it strongly depended on the data size of SSDs. The averaged DAQ efficiency was 82% and 89% for the experimental cycles in 2016 and 2017, respectively.

2.11 Data summary

We took data in two separate experimental cycles, in 2016 and 2017. Table 2.9 shows a data summary of the J-PARC E07 experiment. The emulsion exposure was performed in two cycles of June 2016 and June 2017 for the emulsion module number of 1 to 18 and 19 to 118, respectively. Others were taken for calibration. The polyethylene target was 2.8 g/cm^2 in thickness.

Table 2.9: Summary of the J-PARC E07 experimental data.

Target	Emulsion module	Beam momentum [GeV/c]	Number of incident particles	
			Kaon	Pion
Diamond	#1 to #18	1.81	1.59×10^{10}	3.73×10^{9}
Diamond	#19 to #118	1.81	9.76×10^{10}	2.31×10^{10}
Polyethylene	none	1.81	1.91×10^{9}	3.83×10^{8}
none	none	1.0, 1.2, 1.4		

Chapter 3

Spectrometer analysis

3.1 Overview

For the hybrid emulsion method, incident positions and angles of Ξ^- hyperons were predicted by analyzing the data of spectrometers. The goal of the spectrometer analysis is to obtain positions and angles of Ξ^- stopped at emulsion. The (K^-, K^+) reaction events were tagged with the identification of the beam K^- mesons and the outgoing K^+ mesons. Using SSDs, Ξ^--stopped events were kinematically selected.

In this chapter, the detection efficiency and the single-hit (single-track) ratio are defined as $N(hit \geq 1)/N(all)$ and $N(hit = 1)/N(hit \geq 1)$, respectively.

3.2 Analysis of incident K^- mesons

3.2.1 Timing analysis

Timing information was used to select the (K^-, K^+) reaction events. The timing of BH2 determined the timing of start/stop for the TDC modules of all counters. Figure 3.1 shows the beam time-of-flight distribution between BH1 and BH2. With the time correction using the ADC information, the timing resolution of the beam time-of-flight was 350 ps in FWHM. The time difference between kaons and pions was 1.16 ns at 1.81 GeV/c. However, since pions had been already rejected with BAC1 and BAC2 in the trigger, the dominant component was K^- mesons. The windows were set to be from -2 to 2 ns for the beam time-of-flight.

Timing of BFT was also used for the event selection. Figure 3.2 shows the timing distribution of BFT. The horizontal position at the entrance of the K1.8 beam line spectrometer was measured with BFT for the momentum analysis. The timing resolution of BFT was 1.29 ns in FWHM. To obtain the detection efficiency and the signal-to-noise ratio as higher as possible, the window was set to be from -4 to 4 ns. The detection efficiency and the single-hit ratio were obtained to be 99.5% and 96%, respectively.

3.2.2 BC3 and BC4 analysis

At the exit of K1.8 beam line spectrometer, three-dimensional trajectories of beam particles were reconstructed with hit positions on BC3 and BC4. Such tracking with BC4 and BC4 was called

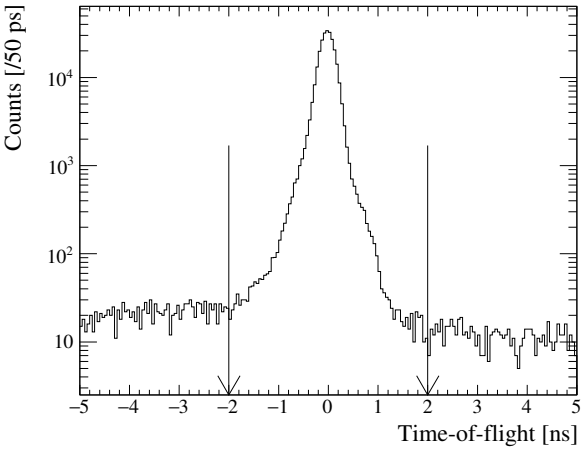

Figure 3.1: Timing distribution of the beam time-of-flight between BH1 and BH2. The arrows represent the time gate for the K^- selection.

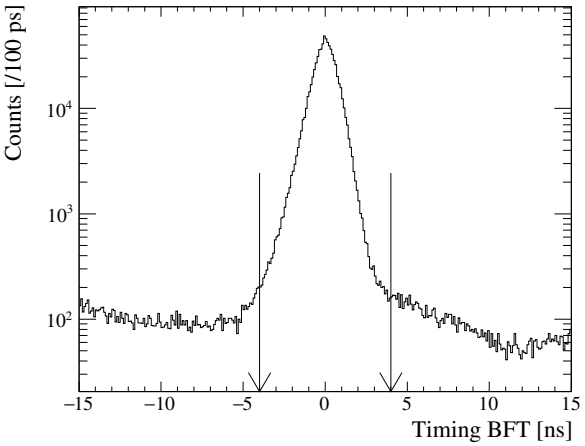

Figure 3.2: Timing distribution of BFT. The arrows represent the time gate.

the BcOut tracking. The straight track was calculated with the method of least squares. All hit combinations were examined to find tracks, where combinations having at least 9 layers out of 12 layers were accepted as candidates. These candidates were sorted according to a chi-squared, χ^2 defined as

$$\begin{aligned}
\chi^2 &\equiv \frac{1}{n-4}\sum_{i=1}^{12} H_i \left(\frac{s_i^{hit} - s^{track}(z_i)}{\sigma_i}\right)^2, \qquad (3.1)\\
n &= \sum_{i=1}^{12} H_i,\\
H_i &= \begin{cases} 1 & \text{(if the } i\text{-th layer has a hit)} \\ 0 & \text{(otherwise)} \end{cases},\\
s^{track}(z_i) &= x(z_i)\cos\alpha_i + y(z_i)\sin\alpha_i,\\
x(z_i) &= x_0 + u_0 z_i,\\
y(z_i) &= y_0 + v_0 z_i,
\end{aligned}$$

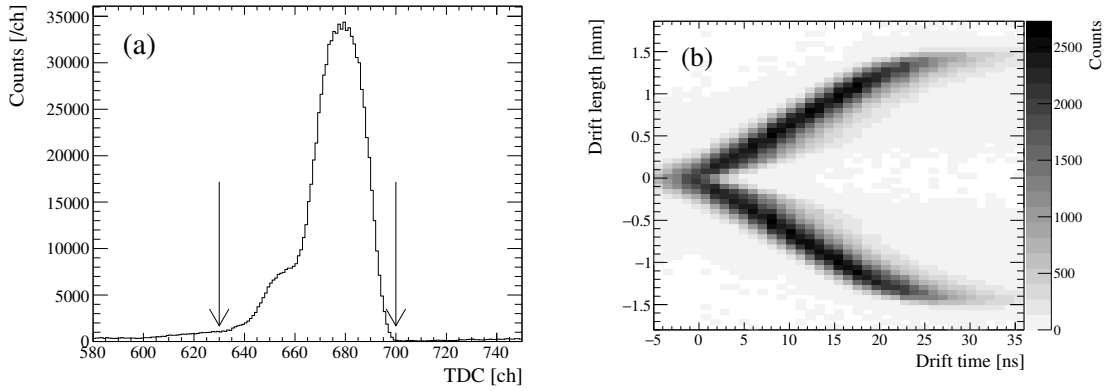

Figure 3.3: (a) TDC distribution and (b) the correlation plot of the drift length versus drift time of BC3. TDC channel had 1-ns LSB.

where, s_i and σ_i are a hit position and position resolution of the i-th layer. $s^{track}(z_i)$ is a calculated position with a wire tilt angle, α_i. The track was parameterized with x_0, y_0, u_0, and v_0, which respectively denote horizontal and vertical positions at the origin of the coordinate and the slopes, dx/dz, and dy/dz. To calculate the hit position of each layer, TDC information was converted to a drift length. Figure 3.3 (a) shows the TDC distribution of BC3. For the reduction of the number of hit combinations, the timing window was set to be from 630 to 700 channel in TDC for both BC3 and BC4. Figure 3.3 (b) shows the plot of the drift length versus the drift time of BC3.

A method of the pair plane analysis was applied to solve the left/right ambiguity. Each pair of xx', uu' and vv' was considered as one unit. The combinations of hits were composed of six pairs in the BcOut tracking. If there are hits in only one layer of a pair, both hit positions of the left/right were calculated.

From the residual distribution of hit positions, intrinsic resolutions for each layer were estimated to be around 180 μm. Thus, a reduced χ^2 distribution was obtained as shown in Figure 3.4. The track candidates were sorted by the χ^2 values. The sorted tracks with duplicate hits were rejected in order. Moreover, in order to reject tracks consisting an error of left/right resolving, the reduced χ^2 value less than 20 were accepted. The detection efficiency and single-track ratio of the BcOut tracking were 99.5% and 99.9%, respectively.

3.2.3 Momentum reconstruction

With the position at the entrance and the track at the exit of the K1.8 beam line spectrometer, momenta of beam particles were reconstructed using a third-order transfer matrix, M calculated by ORBIT [69]. ORBIT had been developed making use of a part of the program TRIO [70]. The third-order transfer matrix M was obtained as

$$\vec{X}_{in} = M(\vec{X}_{out}, \delta), \tag{3.2}$$

$$\begin{aligned} \vec{X}_{in} &= (x_{in}, y_{in}, \frac{dx_{in}}{dz}, \frac{dy_{in}}{dz}), \\ \vec{X}_{out} &= (x_{out}, y_{out}, \frac{dx_{out}}{dz}, \frac{dy_{out}}{dz}), \end{aligned}$$

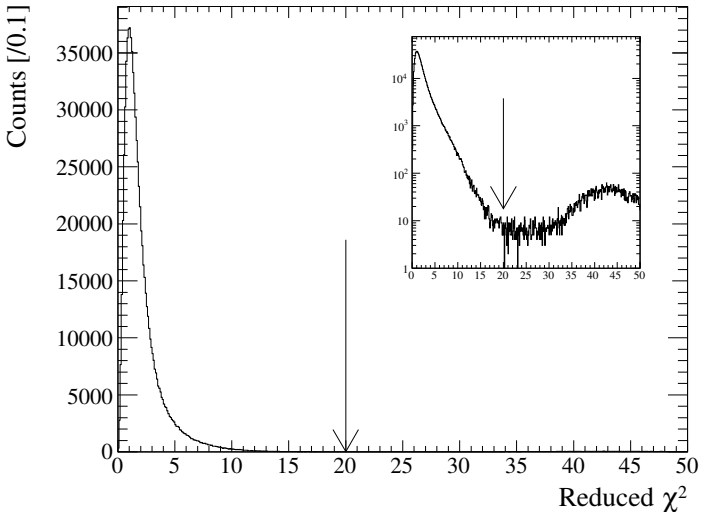

Figure 3.4: Reduced χ^2 distribution of BcOut tracking. The inset shows a logarithmic histogram.

where $\vec{X}_{in}$ and $\vec{X}_{out}$ are the horizontal and vertical positions and their derivatives at the entrance and the exit of the K1.8 beam line spectrometer. δ is momentum deviation from the central momentum denoted as $p = p_0(1+\delta)$, where p_0 is the central momentum. x_{in} was obtained from the position of BFT. The δ value was calculated by solving a cubic equation, $x_{in} = f(\vec{X}_{out}, \delta)$.

In a calculation with the ORBIT program, the properties of magnets were input such as an effective magnetic length, an aperture, a field strength along the central trajectory, and a bending angle.

Figure 3.5 shows the reconstructed beam momentum distribution. The central momentum was 1.81 GeV/c. The momentum bite was 3.4% in FWHM.

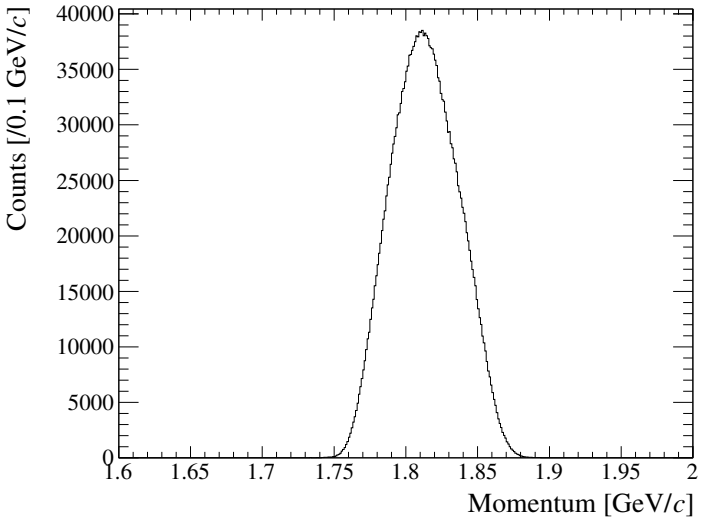

Figure 3.5: Momentum distribution of K^- beam.

3.3 Analysis of outgoing K^+ mesons

3.3.1 SSD1-2 and SDC1 analysis

The straight-line tracking at the entrance of the KURAMA spectrometer, called SdcIn tracking, was performed with SSD1, SSD2, and SDC1. Gathering two tracks at the entrance and the exit of the KURAMA spectrometer, the momentum analysis was performed for outgoing K^+.

SSD

Since SSD1 and SSD2 had the same structures of the detector and the readout system except for the distance between layers as shown in Figure 2.21, the same analysis procedures proceeded for both SSD1 and SSD2. Analog signals of SSD were sampled eight times in APV25-s1 chips with a 40 MHz clock, and digitized with Flash-ADC. A zero-suppression was applied for each waveform to reject waveforms with lower signal height than a threshold.

Figure 3.6 shows a typical waveform of SSD. All ADC count values were subtracted by that of the first sample on the assumption that the first sample was the ground level. The sampling timing was corrected with TDC information of the sampling clock which was also taken in each event. The pulse shape of the waveform was approximated to an ideal CR-RC pulse shape with a 50 ns time constant. For a selection of valid hits, the following function was used to fit each waveform except the first sample,

$$f(t) = a \times (t - t_0) \times \exp\left(-\frac{t - t_0}{\tau}\right), \tag{3.3}$$

$$\begin{aligned} T &= t_0 + \tau \\ A &= a \times \tau \times \frac{1}{e} \\ S &= a \times \tau^2 \end{aligned}$$

where t is time, and t_0 is the start timing. a is the scaling factor. τ is the time constant of 50 ns. T is the peak time. A is the amplitude of the waveform. S is the integration. The value of S was

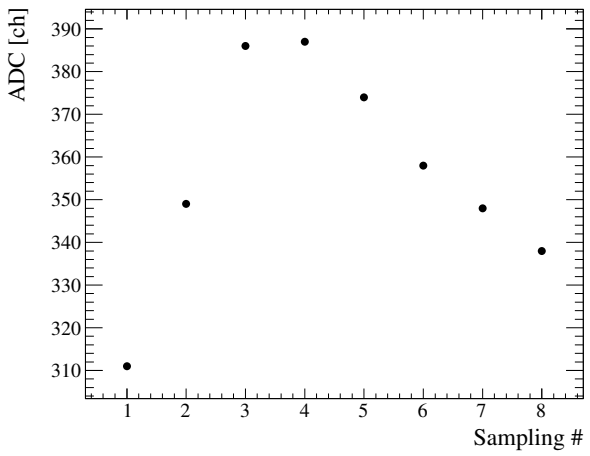

Figure 3.6: A typical waveform of SSD.

treated as a ΔE, and used for the hit selection. The value of the peak time was also used as the timing of the hit. The hits in neighbor strips were clustered, and the clustered ΔE was defined as the sum of them. The cluster position and timing were defined as ΔE-weighted means. Figure 3.7 shows the histogram of the cluster timing versus ΔE. The ΔE was required to be more than 2500 arbitrary unit. The timing window was set from 60 to 120 ns. The time resolution of SSD was found to be 10 ns in FWHM. The hits with the ΔE of about 9000 are corresponding to hits made by the beam kaons.

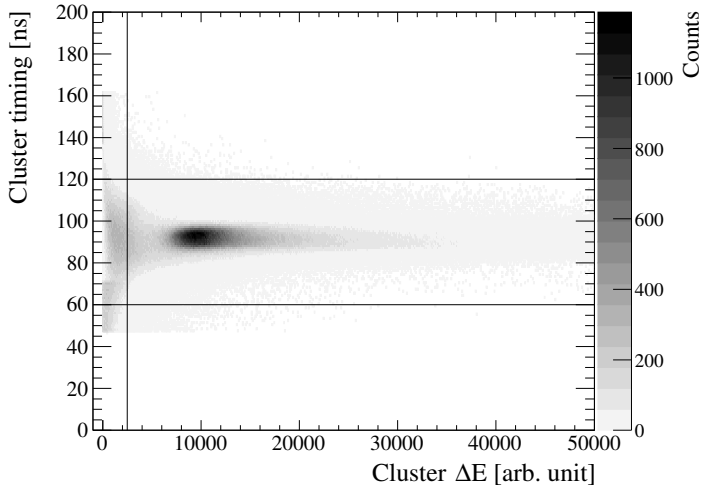

Figure 3.7: Cluster timing versus ΔE plot of SSD. The unit of ΔE is arbitrary.

SDC1

SDC1 was a component of the SdcIn tracking. Since SDC1 was also a drift chamber having a pair plane structure, the analysis proceeded with a similar way as BC3 and BC4. Figure 3.8 (a) shows the TDC distribution of SDC1. The timing window was set to be from 500 to 690 channel in TDC. The correlation plot between the drift length and the drift time is shown in Figure 3.8 (b).

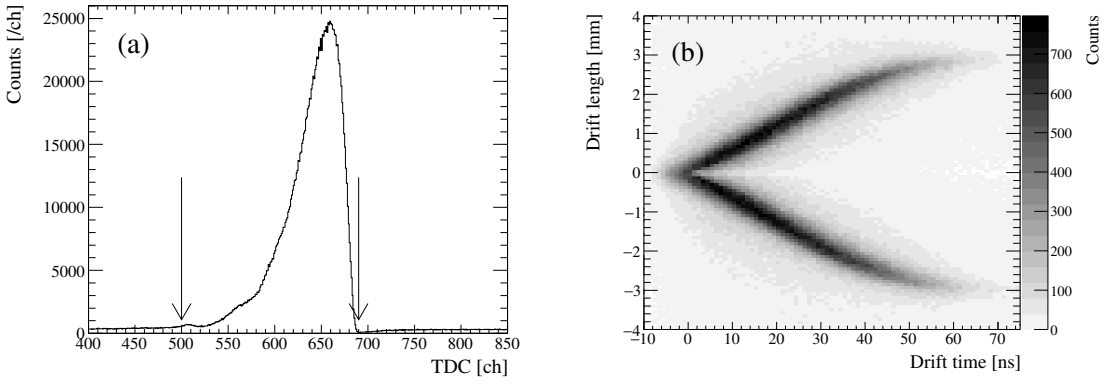

Figure 3.8: (a) TDC distribution and (b) the correlation plot of the drift length versus drift time of SDC1. TDC channel had 1-ns LSB.

SdcIn tracking

The straight-line track at the entrance of the KURAMA spectrometer was searched with SSD1, SSD2 and SDC1. The number of combinations in the SdcIn tracking was higher than in the BcOut tracking, because the number of layers in the SdcIn tracking was larger, fourteen. Moreover, due to the high multiplicity of SSDs, the combination reduction was necessary to search for valid tracks. Although the method of the pair plane analysis was adopted, the method was no longer correct for outgoing particles with large scattering angle, unlike the BcOut tracking.

Owing to the honeycomb-cell structure of SDC1, the hit positions of SDC1 were not on the one-dimensional wire plane. The hit positions were assumed to be a straw, which was the drift length away from the wire. The angle around the wire was iteratively determined so as to be the closest to the track. The ambiguity of the left/right was solved in this process. Figure 3.9 shows the reduced χ^2 distribution of the SdcIn tracking. The tracks were selected by using the same χ^2 sorting method as the BcOut tracking. Intrinsic resolutions for each layer were estimated to be around 20 and 180 μm for SSD and SDC1, respectively. Since SDC1 was placed inside of the magnetic field of the KURAMA magnet, the actual trajectories of scattered particles were affected by the field. However, the SdcIn tracking played only a role of selecting hit candidates for identification of outgoing particles. The minimum number of hit layers was set to be 8 out of 14, because the efficiency was preferred rather than the resolution. The detection efficiency and single-track ratio of the SdcIn tracking were 96.5% and 64.5%, respectively, for the (K^-, K^+) reaction trigger. They were 99.4% and 96.7% for the unbiased trigger.

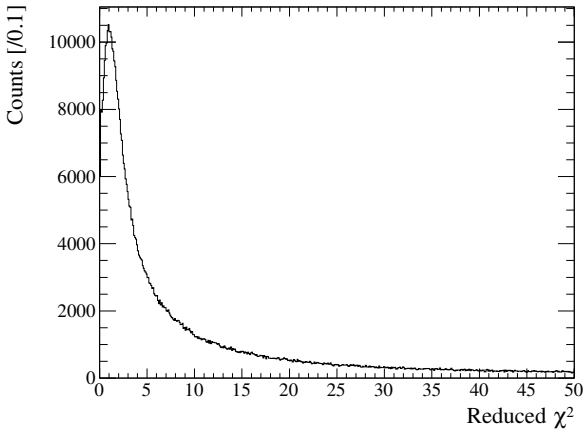

Figure 3.9: Reduced χ^2 distribution of SdcIn tracking.

3.3.2 SDC2-3 and TOF analysis

The straight-line track search at the exit of the KURAMA spectrometer, called SdcOut tracking, was composed of SDC2, SDC3, and TOF. SDC2 and SDC3 consisted of only xx' and yy' pairs. Since the xx' and yy' pairs were arranged to form right angles, x and y were independent of each other. Therefore, TOF joined the SdcOut tracking in order to reject the wrong combination tracks. The hit position of x- and y-direction were calculated by using the scintillator position and the time

difference between up and down signals of TOF, Thus, the ambiguity of the xy combination was solved.

SDC2 and SDC3

The same analysis method was applied to SDC2 and SDC3 as SDC1. Figure 3.10 presents TDC distributions and the correlation plots of the drift length versus drift time, of SDC2 and SDC3. The timing windows of SDC2 and SDC3 was set from 640 to 890, and from 450 to 890 channel of TDC as indicated by arrows in the figure (a) and (c).

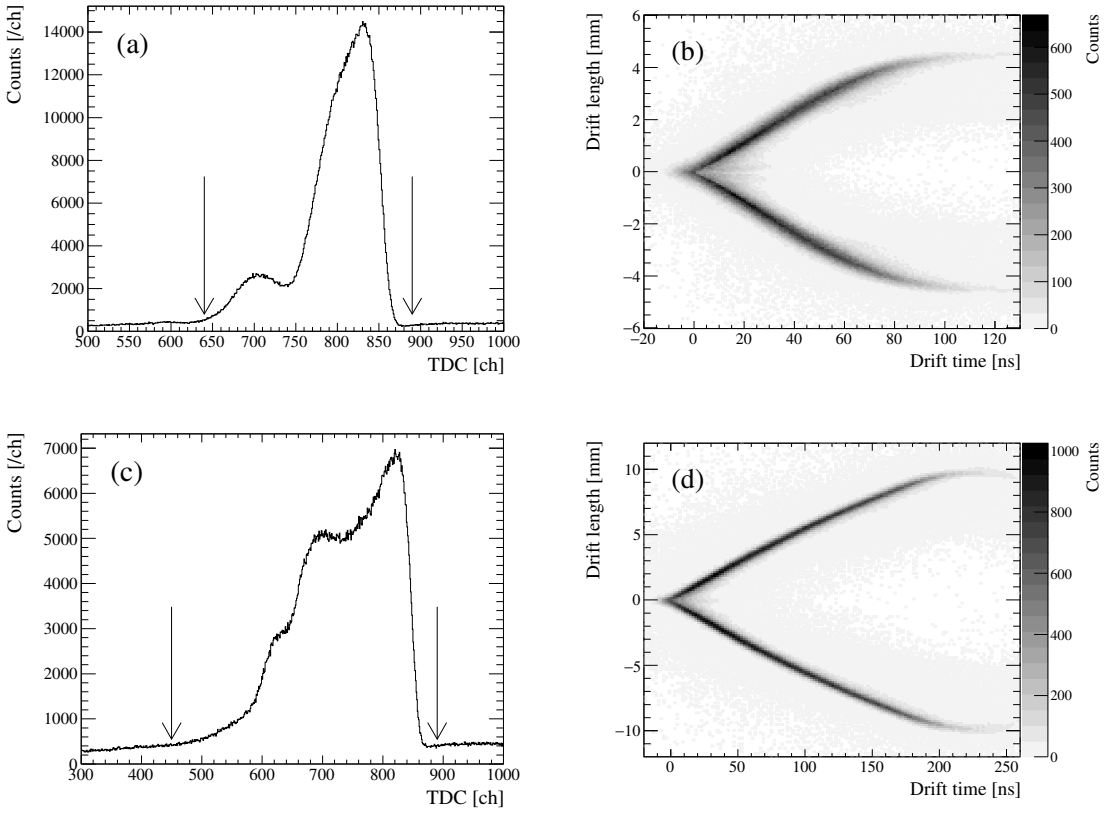

Figure 3.10: (a) TDC distribution and (b) the correlation plot of the drift length versus drift time of SDC2. (c) and (d) are those for SDC3. TDC channel had 1-ns LSB.

SdcOut tracking

The straight-line track search, called SdcOut tracking, was also performed at the exit of the KURAMA spectrometer using SDC2, SDC3, and TOF. Since the drift cell of SDC2 and SDC3 were the same honeycomb structure as SDC1, the hit positions were also calculated with the same procedure. The time difference of up/down signals of TOF enabled to solve the ambiguity of the xy connection. The five layers were required in the SdcOut tracking with regarding SDC2 and SDC3 in total. Figure 3.11 shows the reduced χ^2 distribution of the SdcOut tracking. The tracks were selected by using the same χ^2 sorting method as the BcOut tracking. Intrinsic resolutions for each layer were estimated to be around 180 μm for SDC2 and SDC3, respectively. The detection efficiency and single-track

ratio of the SdcOut tracking were 94.9% and 87.7%, respectively, for the (K^-, K^+) reaction trigger. They were 99.2% and 96.2% for the unbiased trigger.

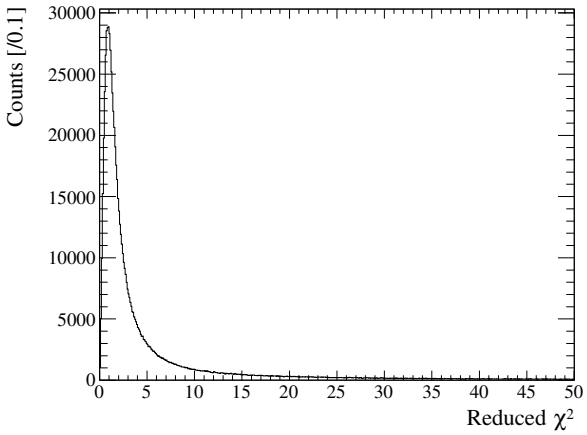

Figure 3.11: Reduced χ^2 distribution of SdcOut tracking.

3.3.3 Momentum reconstruction

Momenta of outgoing particles were reconstructed with the trajectories inside the KURAMA magnet. Using the hits of SdcIn and SdcOut tracks, trajectories of the outgoing particles were reconstructed with the magnetic field. The magnetic field inside KURAMA magnet was made using the electromagnetic field simulation software, ANSYS Maxwell [71] based on the finite element method. The mesh size of the calculated field map was 1 cm.

The reconstruction procedure of the outgoing particles was called the KURAMA tracking. In the KURAMA tracking, the fourth-order Runge-Kutta method [72] was used for the numerical calculation. The tracking started from a virtual plane downstream of TOF. The horizontal and vertical position and angle of the starting vector, and the electric charge divided by the momentum were parameterized. With such five parameters, the χ^2 value defined as

$$\begin{aligned} \chi^2 &\equiv \frac{1}{n-5}\sum_{i=1}^{24} H_i \left(\frac{s_i^{hit} - s_i^{track}}{\sigma_i}\right)^2, \\ n &= \sum_{i=1}^{24} H_i, \\ H_i &= \begin{cases} 1 & \text{(if the } i\text{-th layer has a hit)} \\ 0 & \text{(otherwise)} \end{cases}, \end{aligned} \tag{3.4}$$

were searched for to be iteratively minimized. s_i^{hit} and s_i^{track} are the hit position of the i-th layer and the obtained position from the track, respectively. σ_i is a position resolution of the i-th layer. Initial values of the position and direction were given by the SdcOut tracks. The reduced χ^2 distribution of the KURAMA tracking is shown in Figure 3.12. All combinations between the SdcIn tracks and the SdcOut tracks were calculated The tracks were selected by using the same the χ^2 sorting method as the BcOut tracking. The initial momentum was obtained as a function of the horizontal

bending angle. Since no detector for particle identification such as a cherenkov counter was installed at the exit of the KURAMA spectrometer, in-flight decay of outgoing particles made the χ^2 worse. Since the detection efficiency was essential for the hybrid emulsion method, even events with worse reduced χ^2 were ready to be selected for the emulsion track search. At present, however, the tracks with reduced χ^2 value less than 30 were accepted by considering the signal-to-noise ratio. The single-track ratio of the KURAMA tracking was estimated to be 98.6% with the gate less than 30 for the reduced χ^2 value.

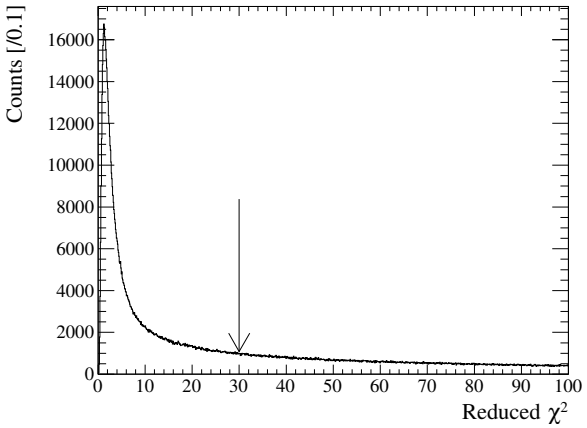

Figure 3.12: Reduced χ^2 distribution of KURAMA tracking. The arrow indicates the accepted value.

Figure 3.13 (a) shows the momentum distribution of outgoing particles. The momentum of outgoing particles was corrected with the method presented in Section 3.4.2. The peaks at 0.4 and 2.0 GeV/c were contributions of π^- and proton as shown in Figure 3.15. The gray area represents the momentum distribution of K^+ with mass selection described in Section 3.3.4. Figure 3.13 (b) shows the momentum distribution of the outgoing K^+ which is corresponding to the gray area in the figure (a). The arrows indicate a momentum gate for the stopped-Ξ^- event selection. Since the high-momentum protons contaminate the kaon region, the particles with the momentum higher than 1.5 GeV/c were rejected. The kaons with the momentum lower than 0.9 GeV/c mainly produced with $\Xi^-\pi$ or $\Xi(1530)^-$ together. Thus, the momentum gate was set to be from 0.9 to 1.5 GeV/c.

3.3.4 Mass reconstruction

Using the Runge-Kutta method, the trajectory of outgoing particles was reconstructed in the KURAMA tracking. The flight path length and flight time were also calculated in the tracking. The flight time was obtained from the time difference between BH2 and TOF. Since the position of BH2 was 1 m away from the target, the time-of-flight of that distance was subtracted as K^-. The velocity and the mass squared of an outgoing particle were reconstructed as

$$\begin{aligned} \beta &= \frac{L}{Tc}, \\ M^2 &= \left(\frac{p}{\beta}\right)^2 (1-\beta^2), \end{aligned} \tag{3.5}$$

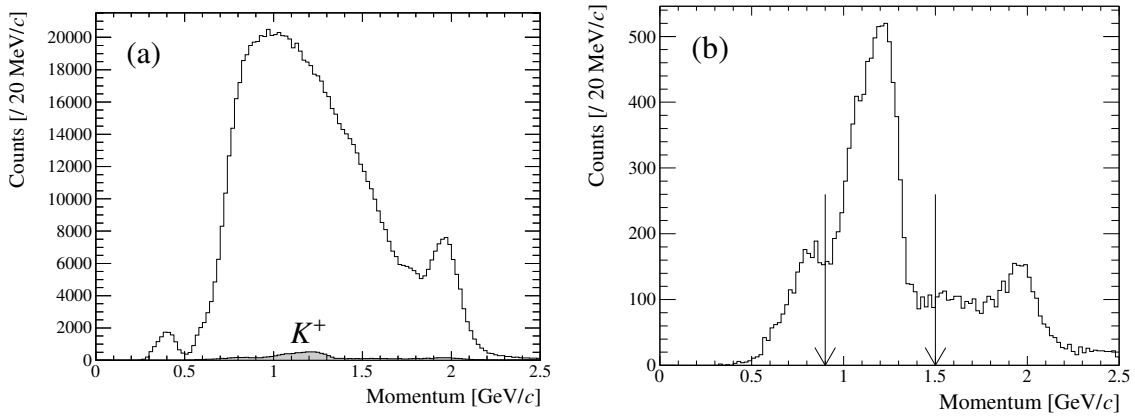

Figure 3.13: (a) Momentum distribution of outgoing particles. The gray area represents the momentum distribution of K^+ with mass selection described in Section 3.3.4. (b) Momentum distribution of the outgoing K^+. The arrows indicate a momentum gate.

where L and T are the flight path length and the flight time. p is the momentum. The sign of the electric charge was given by the bending direction in the KURAMA spectrometer. Figure 3.14 shows the reconstructed mass spectrum of outgoing particles multiplied by the charge sign. The white and gray area corresponds to those before and after the momentum selection, respectively.

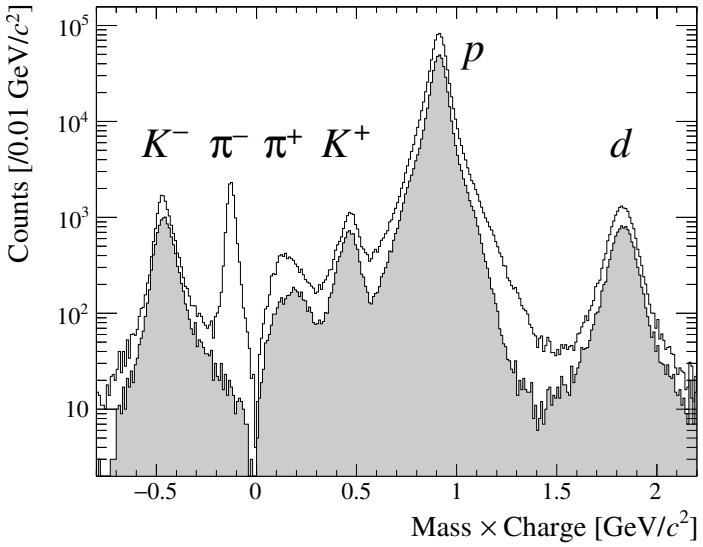

Figure 3.14: Mass spectrum of outgoing particles multiplied by the charge sign. The white and gray area correspond to those before and after the momentum selection, respectively.

The correlation plot of the momentum and mass were shown in Figure 3.15. Since the protons with the momentum of around 2.0 GeV/c contaminated the K^+ region. the particles with the momentum higher than 1.5 GeV/c were rejected. The K^+ with the momentum lower than 0.9 GeV/c were mainly produced with $\Xi^-\pi$ or $\Xi(1530)^-$ together. Moreover, the pion contamination was larger in the lower momentum region. Therefore, the particles with the momentum lower than 0.9 GeV/c were rejected. Figure 3.16 shows the squared mass spectrum of the outgoing particles, where the positive charge was required. The squared mass resolution was 78.4 (MeV/c^2)^2 in FWHM

for the K^+ meson. The arrows indicate the selection window for K^+ mesons. The squared mass within the 3 σ region from the K^+ mass was accepted.

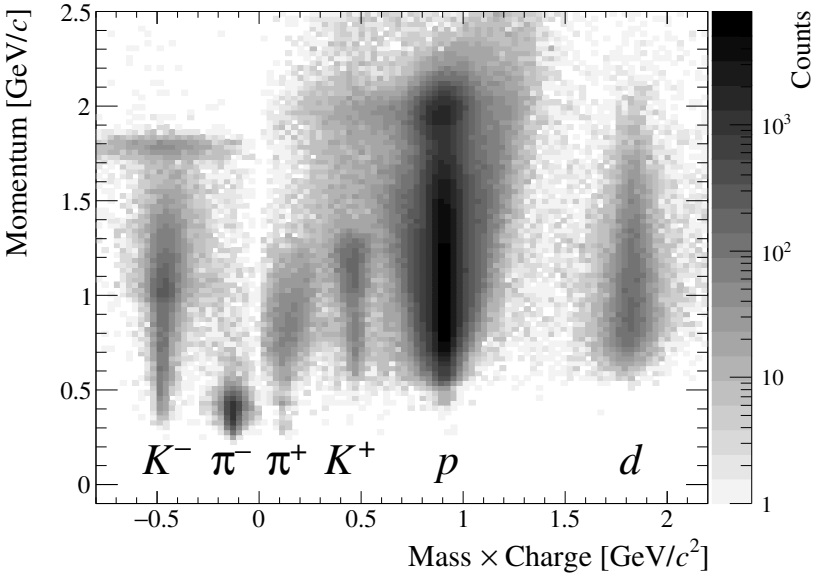

Figure 3.15: Correlation plot of the momentum and mass of outgoing particles.

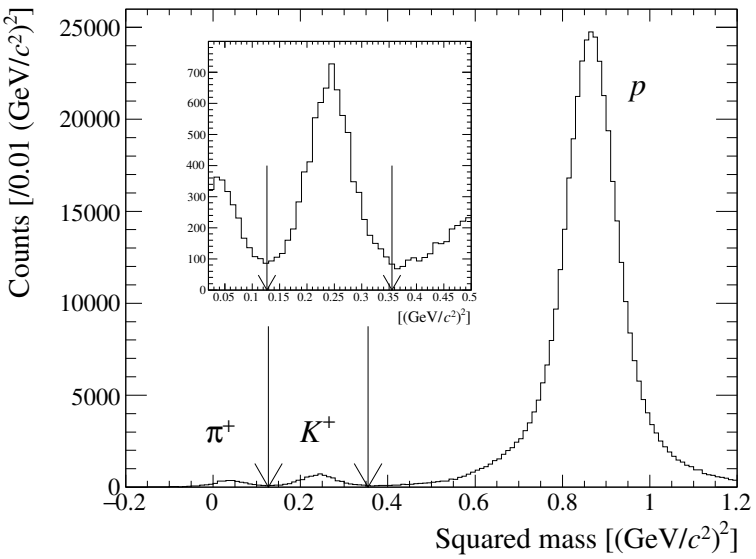

Figure 3.16: Squared mass spectrum of the outgoing particles. The arrows indicates the selection window for K^+.

3.4 Identification of (K^-, K^+) reaction

3.4.1 Vertex reconstruction

From the analysis in Section 3.2 and 3.3, the momenta of the incident K^- meson and outgoing K^+ meson were obtained. The (K^-, K^+) reaction vertex was reconstructed by calculating the closest distance between two tracks of the beam and outgoing particles. Figures 3.17 show the vertices for the (K^-, K^+) reaction and the closest distance distribution between two tracks. The origin of the x, y and z-vertex axes are the center position of the diamond target. Since the x-vertex distribution reflects the beam profile, it seems asymmetric. The x, y and z-vertex windows were ± 50, ± 30, ± 80 mm, respectively, as indicated by arrows. The dashed lines indicate the actual target size. The closest distance was gated to be smaller than 10 mm. Since the position resolution of the BcOut tracking became worse with the extrapolation to the target position, the analysis cut condition of the vertex for the (K^-, K^+) reaction was set wider than the actual target size.

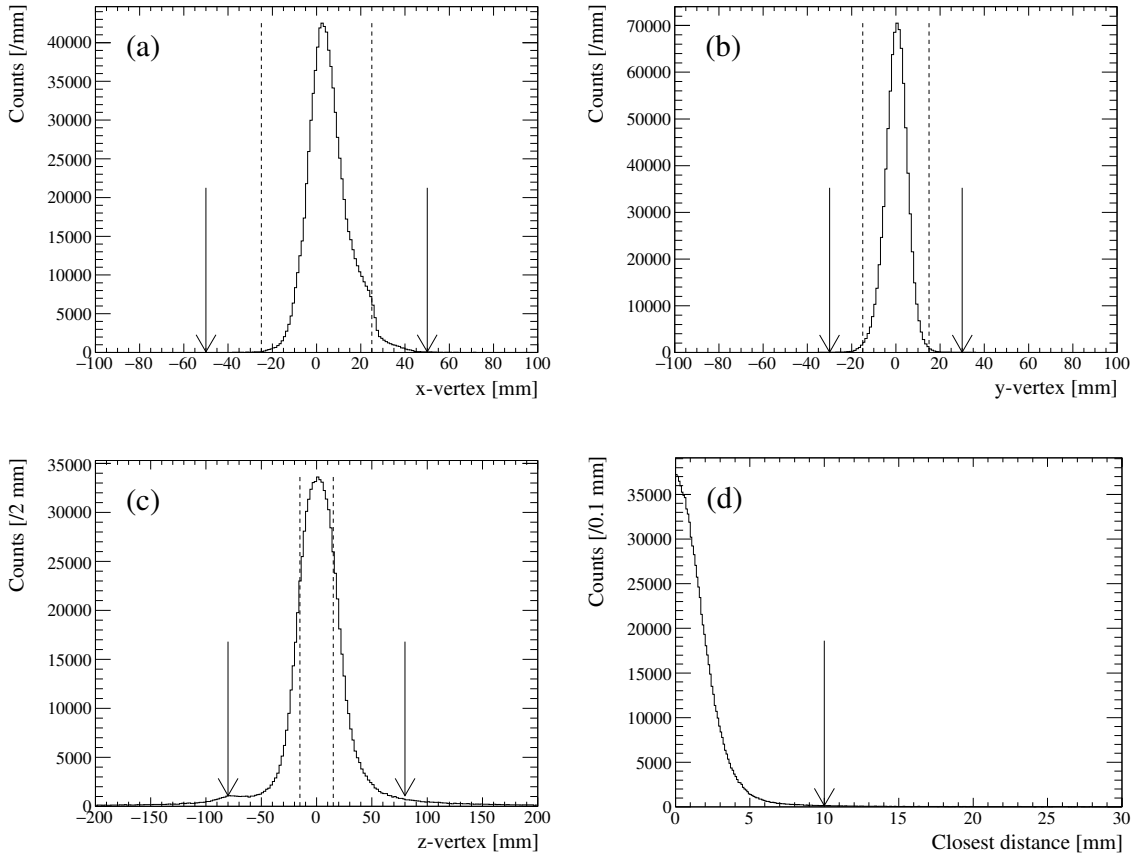

Figure 3.17: Vertex and closest distance distributions for (K^-, K^+) reaction. (a) x-, (b) y- and (c) z-vertex distributions. (d) closest distance distribution between two tracks of the beam and outgoing particle. The arrows indicate the selection windows. The dashed lines present the actual target size.

3.4.2 Momentum correction

The momenta of the outgoing particles were reconstructed by using the calculated magnetic field map for the KURAMA magnet. The calculated field map might not completely reproduce the actual value of the magnetic field. Such a momentum residual between the measured and actual momenta was defined as $\Delta p_{K^+} = p_{K^+}^{measured} - p_{K^+}^{calculated}$. The value of $p_{K^+}^{calculated}$ was calculated with the momentum of K^- and K^+ by assuming the kinematics of the $p(K^-, K^+)\Xi^-$ reaction. The value of $p_{K^+}^{measured}$ was obtained the momentum of K^+ by the KURAMA tracking. In the present experiment, the correlation between Δp_{K^+} and the horizontal angle of outgoing particles was found. Since the proton in the $p(K^-, K^+)\Xi^-$ reaction was assumed to be rest, the Δp_{K^+} distribution with the carbon nucleus target became broader than that with the proton target due to the nucleon Fermi motion. Therefore, the data with the polyethylene target was utilized in order to estimate correction parameters. Figure 3.18 (a) shows a correlation plot between horizontal angles of outgoing particles (dx/dz) and the Δp_{K^+} value. By fitting the momentum residual using a phenomenological function of the fourth order polynomial ($f(dx/dz)$), the corrected momentum was obtained to be $p_{K^+}^{corrected} = p_{K^+}^{measured} - f(dx/dz)$. Figure 3.18 (b) shows the correlation plot after the correction.

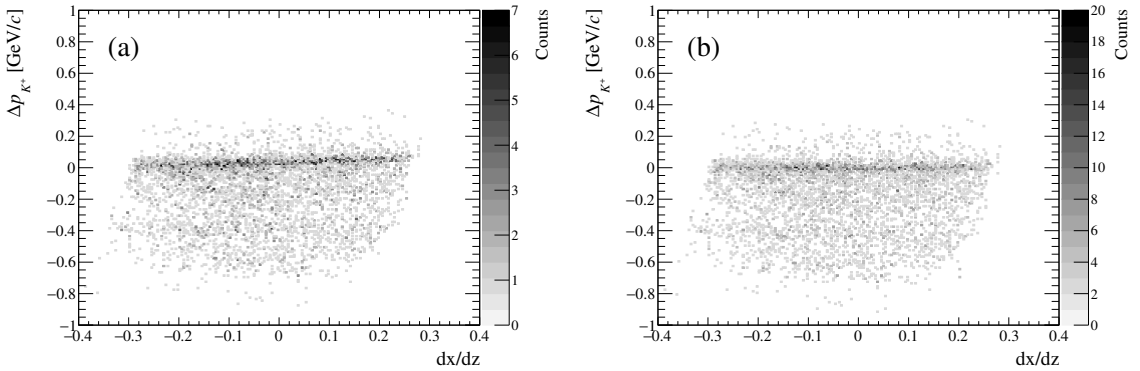

Figure 3.18: Correlation plot between the horizontal angle of outgoing particles (dx/dz) and the momentum residuals with the polyethylene target. (a) and (b) show the correlations of before and after correction, respectively.

The momentum of each outgoing particle was corrected so as to remove the correlation between the horizontal angle and the missing mass in the $p(K^-, K^+)X$ reaction. The missing mass in the $p(K^-, K^+)X$ reaction was obtained as

$$M_X = \sqrt{(E_{K^-} + M_p - E_{K^+})^2 - (p_{K^-}^2 + p_{K^+}^2 - 2p_{K^-}p_{K^+}\cos\theta_{K^-K^+})}, \tag{3.6}$$

where E_{K^-} and p_{K^-} are the total energy and momentum of a K^-, and E_{K^-} and p_{K^-} are those of a K^+, respectively. M_p is the mass of the proton. $\theta_{K^-K^+}$ is the scattering angle of the reaction. Figures 3.19 (a) and (b) show correlation plots between horizontal angles of outgoing particles (dx/dz) and the missing mass in $p(K^-, K^+)X$ reaction at the polyethylene target before and after the momentum correction, respectively. Figure 3.20 shows the missing mass spectrum in the $p(K^-, K^+)X$ reaction at the polyethylene target after the momentum correction. The peaks of Ξ^- and $\Xi(1530)^-$ were observed to be consistent with the PDG value [73]. The events making components under the

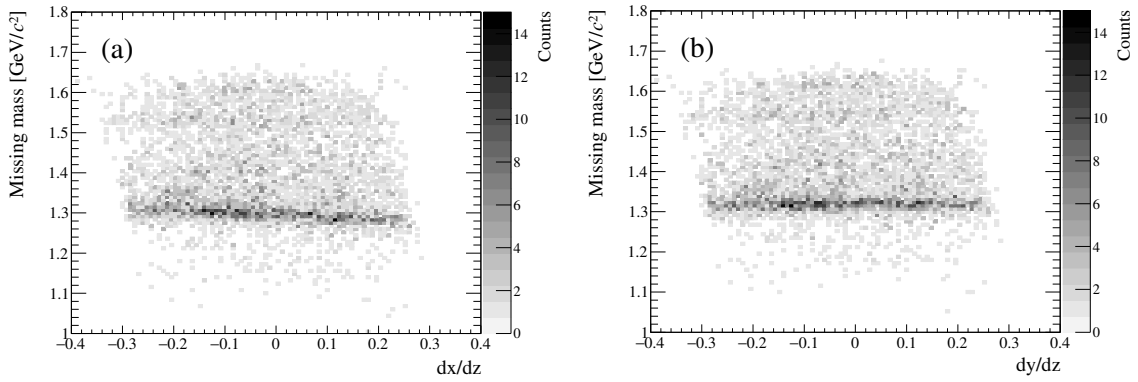

Figure 3.19: Correlation plot between horizontal angles of outgoing particles (dx/dz) and missing mass in $p(K^-, K^+)X$ reaction at the polyethylene target. (a) and (b) show the correlations of before and after correction, respectively.

peaks were the contribution of the carbon nucleus in the polyethylene target and $\Xi\pi$ production. The missing mass spectrum was fitted with two Gaussian functions assuming that the narrow and broad peaks were attributed to free protons and quasi-free reactions in carbon nuclei, respectively. The narrow peak width was obtained to be 24.1 MeV/c^2 in FWHM. The momentum correction for the outgoing K^+ was applied to the analysis of whole data.

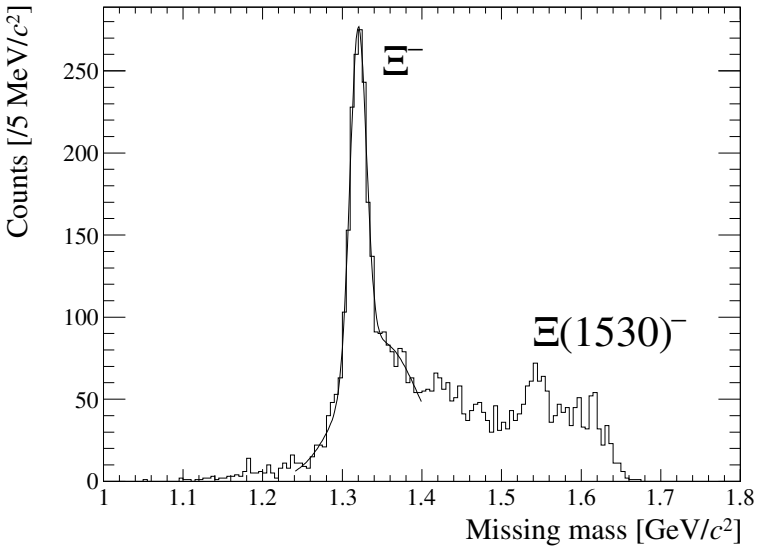

Figure 3.20: Missing mass spectrum in the $p(K^-, K^+)X$ reaction at the polyethylene target. The peak width of Ξ^- was obtained to be 24.1 MeV/c^2 in FWHM.

3.5 Event selection of stopped-Ξ^-

3.5.1 Kinematic selection

The Ξ^- hyperons produced via the (K^-, K^+) reaction passed through SSD1, and stopped at the emulsion. In order to select the Ξ^--stopped events, the missing momentum direction of the $p(K^-, K^+)X$ reaction was very important information. In such events, SSD1 should have an additional hit except for the K^+ meson. Since Ξ^- deposits a large ΔE on SSD, the other threshold was set for the ΔE of SSD1–2 to distinguish the Ξ^- signal from others. For the Ξ^- analysis, the ΔE of SSD1 was required to be more than 15000 arbitrary unit, which is corresponding to the energy loss of 1.5 MIP.

Ξ^- tracking

The tracking of Ξ^- was performed using four layers of SSD1. Since the chi-squared method was unavailable for the Ξ^- tracking, the Kinematic consistency was applied to select the Ξ^- tracks.

Figure 3.21 shows the correlation plot of angular residuals of horizontal dx/dz and vertical dy/dz between the Ξ^- track and the missing momentum direction in the (K^-, K^+) reaction. The tracks were accepted within the 3 σ region indicated by the ellipse line.

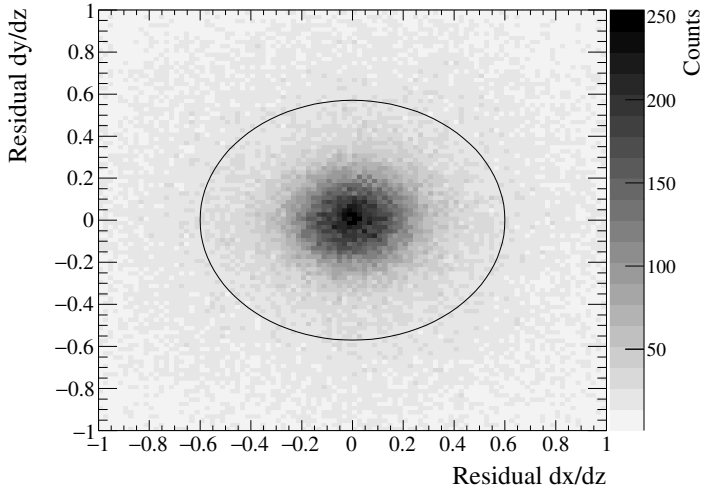

Figure 3.21: Correlation plot of angular residuals of dx/dz and dydz between the Ξ^- track and the missing momentum in the (K^-, K^+) reaction. The ellipse line indicates the 3 σ region.

Owing to the good position resolution of SSD, the vertex resolution between the K^+ and Ξ^- tracks was much better than that between the K^- and K^+ tracks. Figures 3.22 show the vertices and the closest distance distribution between the K^+ and Ξ^- tracks. The origin of the x, y and z-vertex axes are the center position of the diamond target. The x, y and z-vertex windows were ± 30, ± 20, ± 40 mm, respectively, as indicated by arrows. The dashed lines indicate the actual target size. The x and y distributions are similar to those of the K^--K^+ vertex. The z-vertex distribution was biased to a downstream side due to the decay and absorption of Ξ^- hyperons inside the diamond

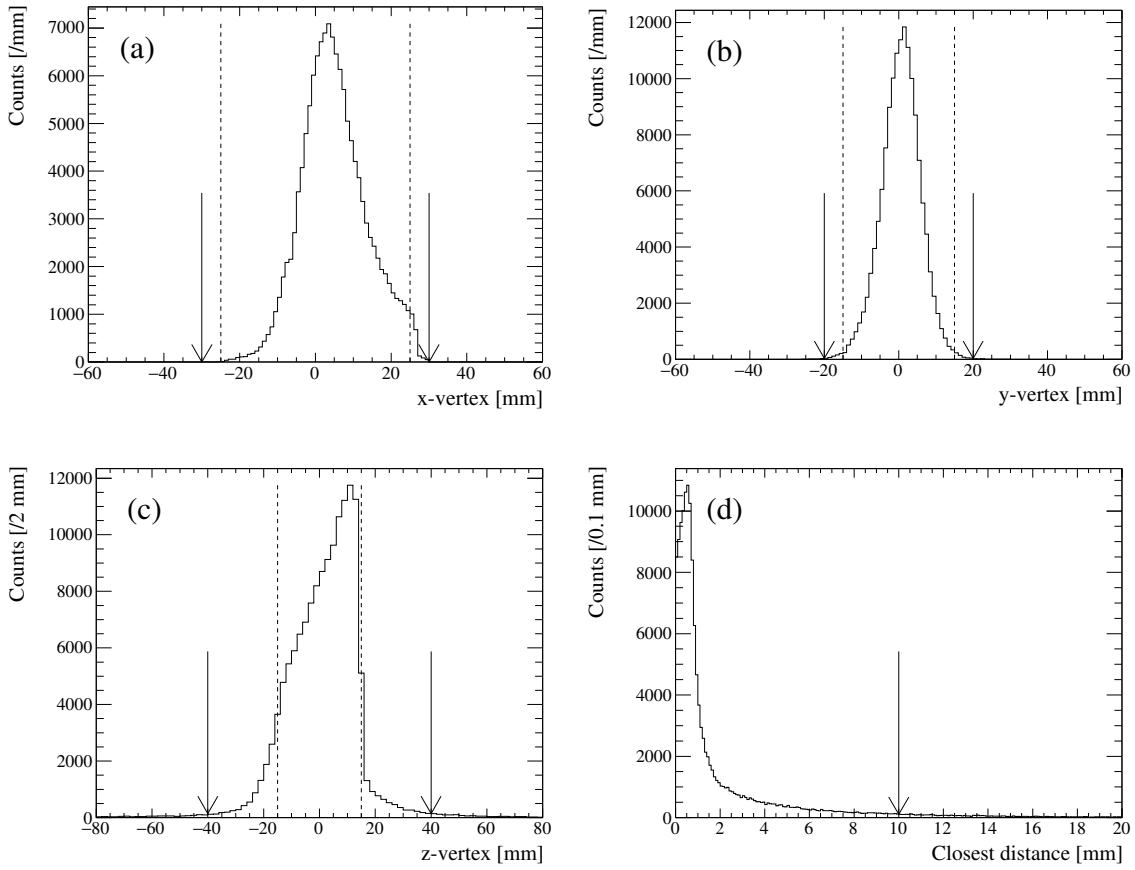

Figure 3.22: Vertex and closest distance distributions between K^+ and Ξ^- tracks. (a) x-, (b) y-, and (c) z-vertex distributions. (d) closest distance distribution between two tracks of K^+ meson and Ξ^- hyperon. The arrows indicate the selection windows. The dashed lines present the actual target size.

target. The closest distance was gated to be smaller than 10 mm.

The position residuals between two vertices of K^--K^+ and K^+-Ξ^-, were also used to improve the quality of the Ξ^- tracks. Figures 3.23 show the position residuals. The residual value of the 5 σ region was accepted as indicated by the arrows in each figure.

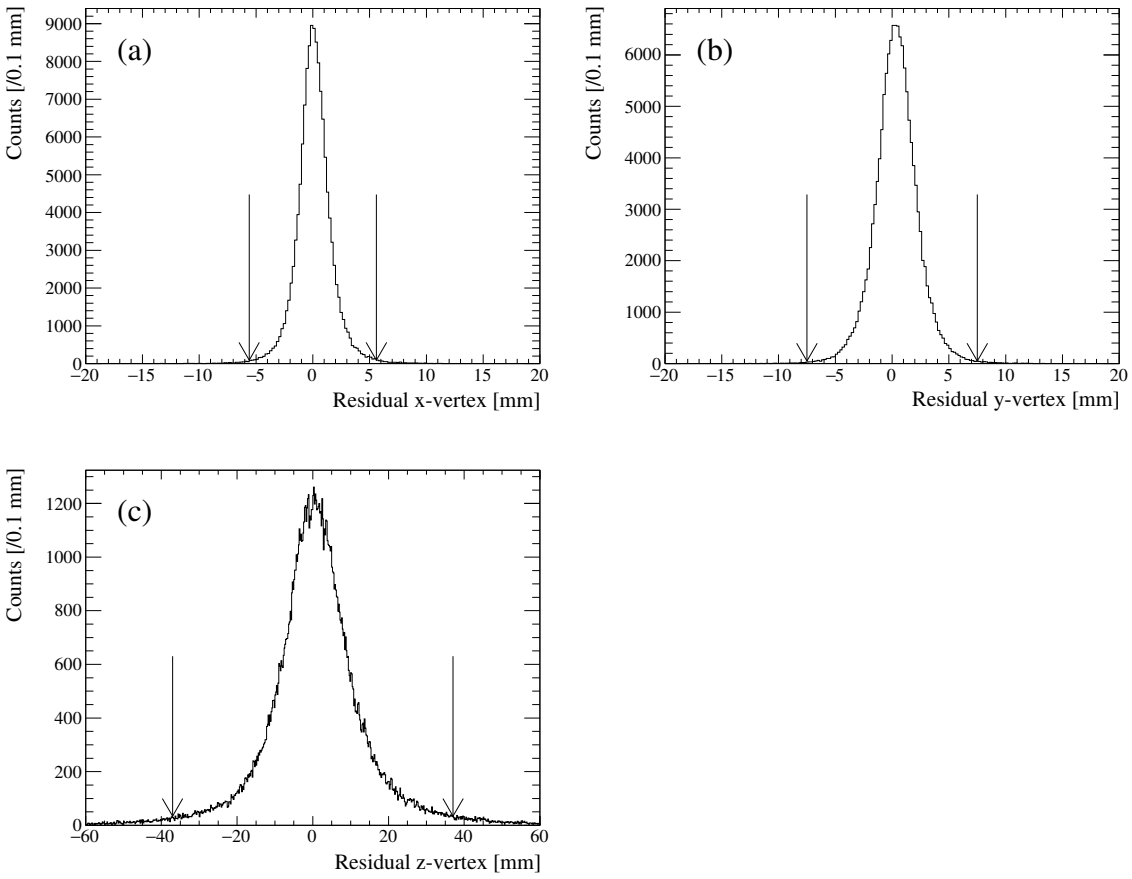

Figure 3.23: Residual distributions between two vertices of K^-–K^+ and K^+–Ξ^-. (a) x-, (b) y-, and (c) z-vertex residual distributions. The arrows indicate the selection windows.

3.5.2 Detection of Ξ^- passing through emulsion

When Ξ^- hyperons passed through the emulsion module, those Ξ^- hyperons may also penetrate SSD2. Therefore, hit information of SSD2 was used as a flag of the detection of Ξ^- hyperons passing through the emulsion module. Figure 3.24 shows the correlation of the ΔE of SSD2 and the position residual, where the position residual is defined as the position difference between the hit position of SSD2 and the extrapolated position of the Ξ^- track. The ΔE value of SSD2 was required to be more than 20000 arbitrary unit, which was corresponding to around the energy loss of 2 MIP. The vertical lines indicate the selected 3 σ region of the position residual. Such hits were treated as a Ξ^- penetration. In order to select the stopped Ξ^- tracks, 0 or 1 of the number of hit layers were accepted. In the case that the number of hit layers was 2, the tracks were allowed only when those two layers were $x(x')$ and $y(y')$. In the case that the number of hit layers was 3 or 4, the Ξ^- was

regarded as penetrating, and the track was rejected.

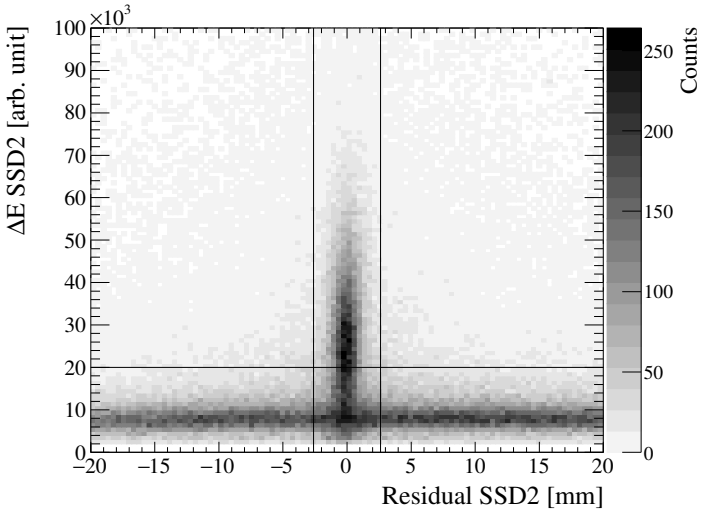

Figure 3.24: Correlation of ΔE and position residual of SSD2 between hit position and extrapolated position from the SSD1 track. The ΔE value of SSD2 was required to be more than 20000 arbitrary unit. The vertical lines indicate the accepted gate of the position residual.

3.5.3 Stopped-Ξ^- event

According to the identification of the (K^-, K^+) reaction events and the kinematic selection of the Ξ^- hyperons, the Ξ^- track candidates were obtained for the emulsion analysis. Table 3.1 summarizes the result of the event selection.

Table 3.1: Result of the event selection.

Events with Ξ^- track candidates	70726
Ξ^- track candidates	81034
Background contamination of K^+	10.0%
Acceptance of the emulsion module	98.4%

Figures 3.25 show spectra of missing mass and missing momentum of the $p(K^-, K^+)X$ reaction for the selected events. Since the kaons with the momentum lower than 0.9 GeV/c were mainly produced together with $\Xi^-\pi$ or $\Xi(1530)^-$, the momentum of K^+ was selected to be higher than 0.9 GeV/c. Hence, the higher missing mass and momentum were suppressed.

Figure 3.26 shows the squared mass spectrum of the outgoing particles for the selected events only without the mass selection. The spectrum was fitted with a Gaussian function and background which was assumed to be a linear function. The background contamination within the mass gate was estimated to be 10.0%.

The xy distribution of the selected Ξ^- candidates on the emulsion coordinate is shown in Figure 3.27. The solid square line indicates the sensitive area of the emulsion module. Since the four corners of the emulsion module were utilized for the $\overline{p}$ beam pattern matching, the number of the Ξ^- tracks

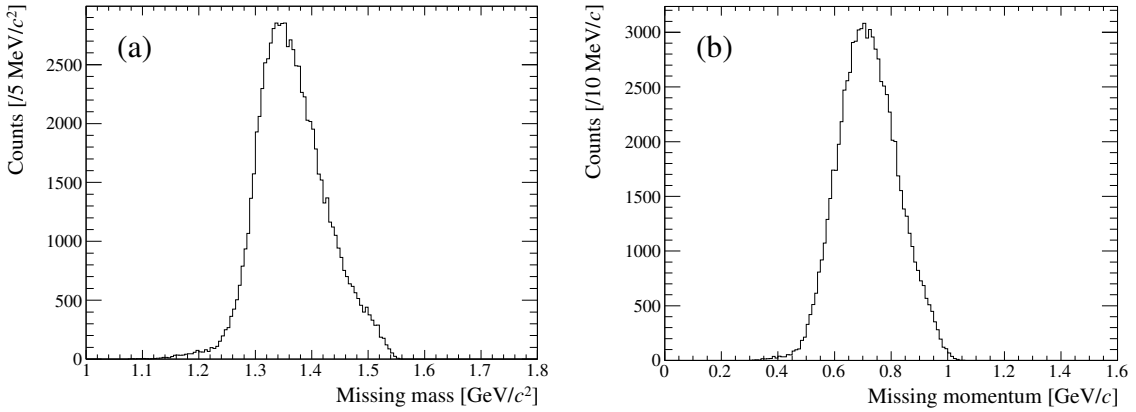

Figure 3.25: Spectra of (a) missing mass and (b) missing momentum of the $p(K^-, K^+)X$ reaction for the selected events.

is smaller than other regions. The acceptance of the emulsion module for the selected Ξ^- tracks was obtained to be 98.4%. The position and angle at the surface of the emulsion module were calculated for each Ξ^- candidate. The relative position between SSD1 and the emulsion module was corrected with the $\overline{p}$ beam pattern matching to be described in Section 4.2.3. The distance between SSD1 and the emulsion module was slightly different in each emulsion module. However, the distance correction was difficult with the analysis of SSD1. Therefore, the distance was corrected using the track position and angle in emulsion. Considering the distance correction, the tracks inside of the acceptance of the emulsion module were accepted. Even if we tightly select events of stopped Ξ^- hyperons by the above analysis, events of decay Ξ^- hyperons near or after passing SSD1 were mixed. The ratio of Ξ^- hyperons stopping at an emulsion module was estimated from Geant4 simulation using a Monte Carlo method [74]. Around ten thousand Ξ^- hyperons were expected to stop at emulsion in total.

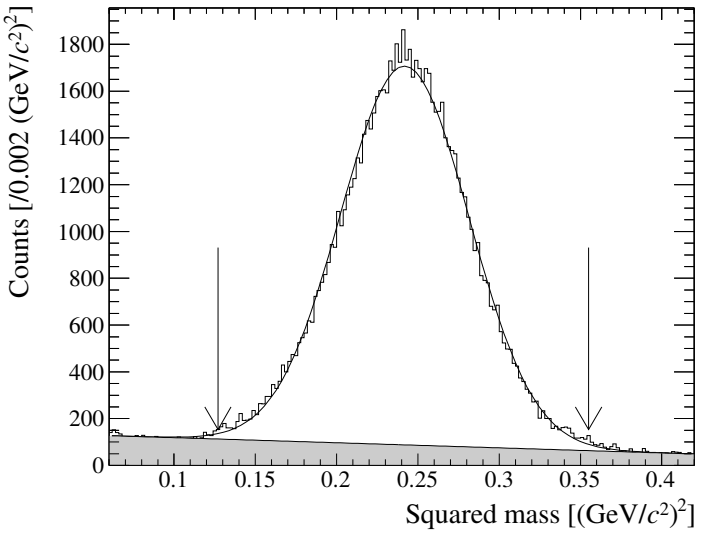

Figure 3.26: Squared mass spectrum of outgoing particles for the selected events without mass selection. The arrows present the same mass gate as shown in Figure 3.16. The gray area indicates the background contamination of 10.0% in the mass gate.

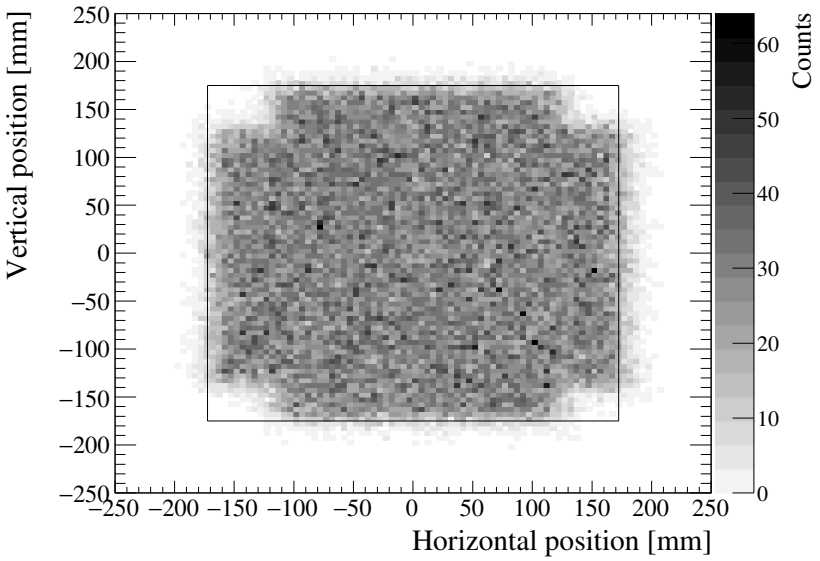

Figure 3.27: Predicted position distribution of incident Ξ^- tracks on the upstream surface of the emulsion module. The region inside lines indicates the sensitive area of the emulsion. The acceptance of the emulsion module for the selected Ξ^- tracks was estimated to be 98.4%.

Chapter 4
Emulsion scanning and analysis

4.1 Hardware configuration

The hardware configuration of the emulsion scanning system is presented in Figure 4.1. An image-processing board (Renesas VP-910) and a motor-control board (ADTEK aPCI-M59) were mounted on a control server (Windows 7). A scanning stage equipped an optical microscope was movable in the horizontal direction (x/y) within a 350×350-mm^2 area with stepping motors (Oriental motor PK566-NBC). The vertical direction, thickness direction, (z) was moved with another stepping motor (Oriental motor PK543-NBC). The stepping motors were controlled by a motor driver (Oriental motor DFU1514). The positions of the motors were measured with linear encoders (Heidenhain LS406) and an incremental length gauge (Heidenhain MT2501) for the horizontal and vertical direction, respectively. Those accuracies were 3 μm and 0.2 μm. An interface electronics (Heidenhain EXE 602E) interpolated and digitized the signals from the encoders. The motor driver and the interpolate-digitizer were connected to the motor-control board. The photographs of a CCD camera (SONY XC-HR300) were digitized with an image-processing board (Renesas VP-910). An LED light source (LUXEON) was controlled through a serial port converted from a USB interface on the server. The flash timing of the LED was synchronized with the timing of taking a photograph. An objective lens with the magnification of 50 was used for the scanning.

4.2 Position alignment

An emulsion sheet is shrunk and deformed during the development process. Moreover, the position of emulsion sheets in the cassette were slightly different module by module. Therefore, the position alignment was quite necessary to connect tracks between SSD1 and the first emulsion sheet, or between the emulsion sheets. For the Ξ^- track search, the following corrections were carried out.

4.2.1 Deformation correction of emulsion sheet

In the development process, an emulsion sheet is shrunk in the vertical (z) direction. The shrinkage factor was estimated by measuring the thickness of the sheets just before the exposure time in the experiment. In the horizontal (xy) direction, the deformation was corrected with the positions of

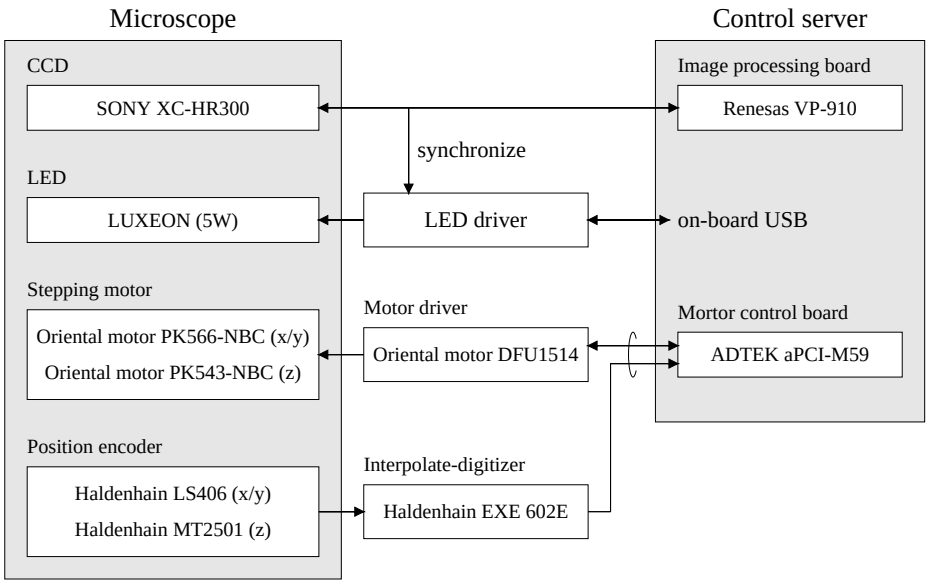

Figure 4.1: Hardware configuration of the microscope system.

grid marks with a diameter of 50 μm. The grid marks were printed in grid pattern with 10 mm pitch using a strobe light with an emitting time of 18 μs $\times$ 172 flashes = 3 ms for each emulsion sheet. Aluminum and copper plates were used as the grid template.

Figure 4.2 shows the deformation of grid marks. The arrows indicate directions and magnitude of the deformation at the position. Start points of the arrow are the grid positions before the development, and end points show those after the development. The scale of the deformation is emphasized. The grid marks of the thin-type emulsion sheet were deformed around 100 μm, while those of the thick-type emulsion sheet was deformed around 500 μm due to the difference of the thickness. The thick-type sheet was deformed in almost proportion to the distance from the center.

Before starting the emulsion scanning, the horizontal (xy) position was corrected by performing the affine transformation with the grid mark measurement of the nearest three grid marks.

4.2.2 Alignment between SSD1 and emulsion module

In order to connect Ξ^- track candidates to the first sheet of the emulsion module, alignment of their relative position was essential. For the position calibration, we used $\overline{p}$ beam with the momentum of 1.8 GeV/c through both SSD1 and the emulsion module in the experiment. In order to make a dark track in emulsion, proton beam with lower momentum is more suitable than $\overline{p}$ beam with the momentum of 1.8 GeV/c. However, it took time to change the condition of beam line magnets. Therefore, $\overline{p}$ beam with the momentum of 1.8 GeV/c was adopted so as to keep the same charge sign and momentum.

When the emulsion module was mounted on the emulsion mover, four corners of the emulsion module were exposed to the $\overline{p}$ beam before the K^- beam exposure. The intensity of the $\overline{p}$ beam was around 700 per spill adjusted with the beam line slits. In order to keep high signal-to-noise ratio of the pattern matching, the track density of the total irradiated $\overline{p}$ beam was 10^4 tracks/cm^2 for each

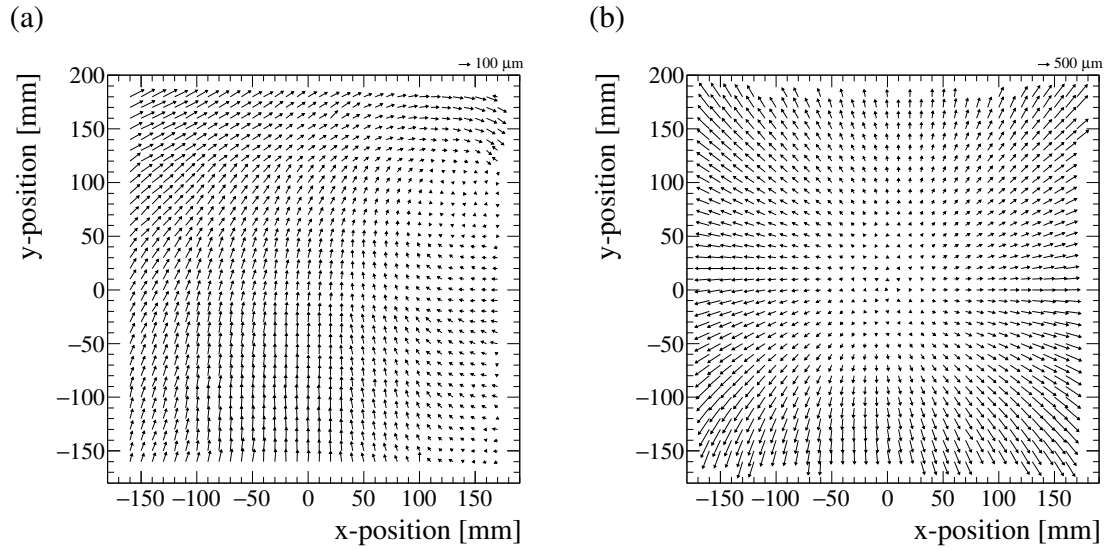

Figure 4.2: Deformation of (a) thin-type emulsion sheet and (b) thick-type emulsion sheet. The start and end points of the arrows present the positions of the grid mark before and after the development, respectively.

corner of the emulsion module. The DAQ efficiency was 93% on average.

The $\overline{p}$ beam patterns tracked with SSD1 and the first thin-type emulsion sheet were compared one by one. Using two track lists of SSD1 and the first sheet, the position residuals of x- and y-directions were calculated for all track pairs as shown in Figure 4.3. The typical scan area was 5 mm $\times$ 5 mm. In those plots of x- and y-residuals, a peak appears as a position offset between SSD1 and the first emulsion sheet. From the widths of the peaks, the alignment precisions were deduced to be 36.8 μm and 35.5 μm in FWHM for x- and y-direction, respectively.

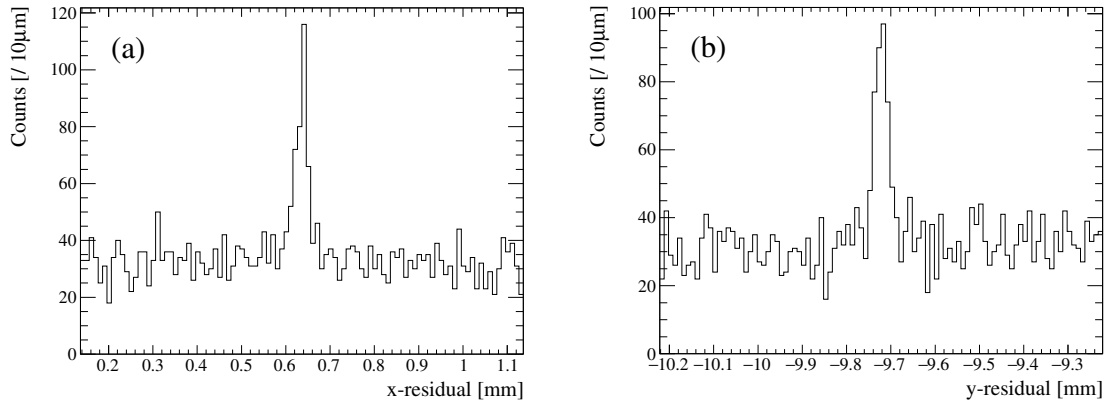

Figure 4.3: (a) x and (b) y position residual distributions between SSD1 and the first thin-type emulsion sheet using the $\overline{p}$ beam pattern matching..

4.2.3 Alignment between adjacent emulsion sheets

Edges of the emulsion sheets were uneven in the emulsion cassette. Therefore, the relative positions of emulsion sheets were necessary to be aligned with each other. Since the cassette was evacuated by a vacuum pump, each emulsion sheet was enough close to neighbors. The relative position between emulsion sheets was fixed during the beam exposure. In regard to the position alignment between two emulsion sheets, any beam tracks were available for the beam pattern matching. In the Ξ^- tracking process, we selected straight beam tracks near the Ξ^- track. The beam pattern matching of two emulsion sheets was performed in the same manner as the $\overline{p}$ beam pattern matching. The track positions at the emulsion surface were used as the beam pattern in contact with the neighbor sheet. Figure 4.4 shows the position residual distributions between two emulsion sheets. The typical scan areas were 1 mm × 1 mm for the downstream sheet and 2.4 mm × 2.4 mm for the upstream sheet. Each peak position presents a value of the position offset. With the peak widths, the alignment precisions were obtained to be 1.7 μm and 1.5 μm in FWHM for x- and y-direction, respectively.

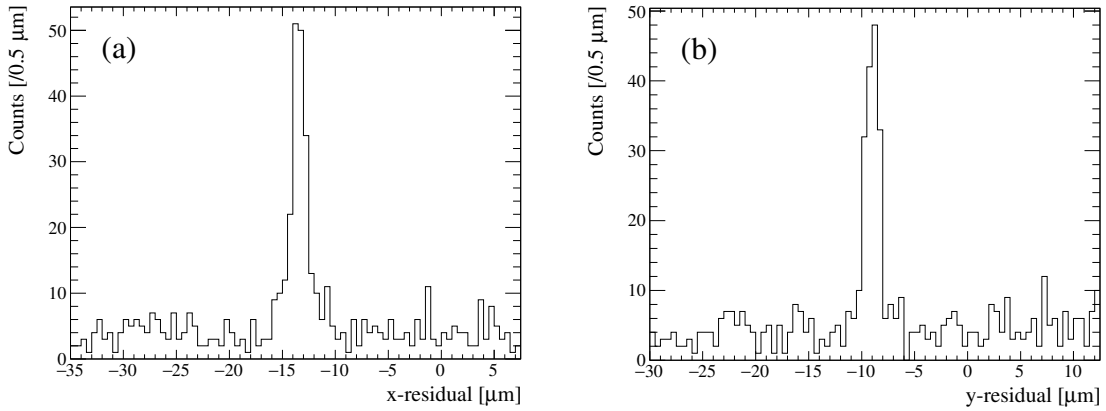

Figure 4.4: (a) x and (b) y position residual distributions between two emulsion sheets using beam tracks near a Ξ^- track.

4.3 Track following in emulsion

4.3.1 Track selection at the first thin-type sheet

Using the positions and angles of the Ξ^- track candidates predicted with SSD, Ξ^- tracks were searched for in 400 × 400-μm^2 along the track direction around the predicted position in the first thin-type emulsion sheet. The searched area was constructed by regions with the view size of the microscope (145 × 125 μm^2). The view images were overlapped with the next images by 20 μm. The predicted position was corrected with the distance between SSD1 and the thin-type sheet. Since the surface position of the thin-type sheet slightly depended on the packing condition or the cassette, the distance parameter was optimized for each emulsion module so as to minimize the position residual by using angled SSD1 tracks. The angle (tanθ) of candidates was selected to be 0.18 to 1.2. Tracks having the angular residual (Δtanθ) of less than 0.08 were sought for in the search region. The

multiplicity of track candidates was presented in Figure 4.5. The efficiency of the track search at the first thin-type sheet gradually decreased as the angle increased. All candidates were followed to the next thick-type sheet even if more than one tracks were found.

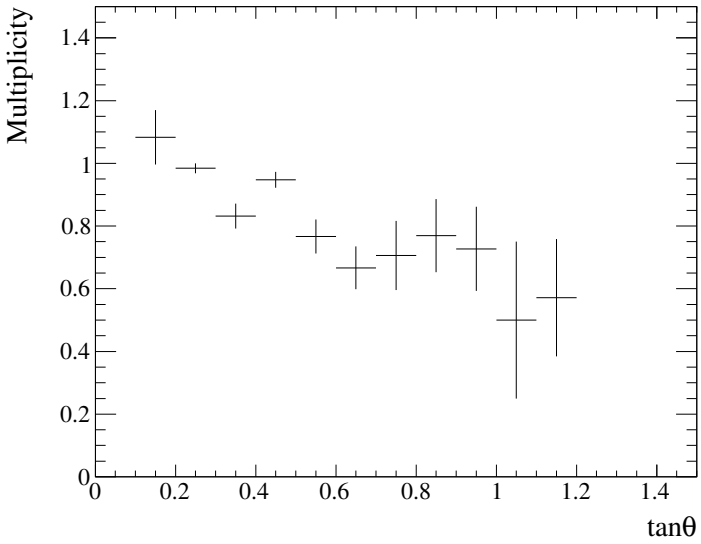

Figure 4.5: Multiplicity distribution of tracks found on the first thin-type emulsion sheet. θ is an angle of the found track formed with the emulsion plane.

Figures 4.6 show the position and angular residual distributions between the prediction and the found track. The precision became worse than the alignment precision due to the Ξ^- hyperon decay and the multiple scattering. The peak widths were 180 μm and 200 μm in FWHM for x and y position, respectively. The FWHMs of angular residuals were 60 mrad on both x and y axis. For the next thick-type emulsion sheet, the positions and angles were predicted with those found tracks.

4.3.2 Track following system

Using the positions and angles of the Ξ^- track candidates predicted with SSD, the emulsion module have been scanned for the search of twin Λ hypernuclei and double-Λ hypernuclei. Soe et al. [75] developed a track following system. The emulsion scanning was performed with the further developed system. Figure 4.7 shows the conceptual drawing of the track following system.

The track following of the thick-type emulsion sheets began using the predictions from the first thin-type sheet. As for the tracking in the $(i+1)$-th emulsion sheet, the track was searched on the emulsion surface at first. From the top surface of the emulsion sheet, ten micrographic images were taken with each interval of 3 μm/cos θ along the z-axis. The interval was changed depending on the track angle. Each image was shifted in the image processing to keep the track on the center using the track angle of the (i)-th emulsion sheet. The position and angle of the followed track were renewed with the processed ten images. The following was repeated until the track end or the bottom of the sheet.

Thus, using the track-following system, the Ξ^- track candidates were traced. Since tracks of Ξ^- hyperons with low-momentum are largely affected by the multiple scattering, the track-following

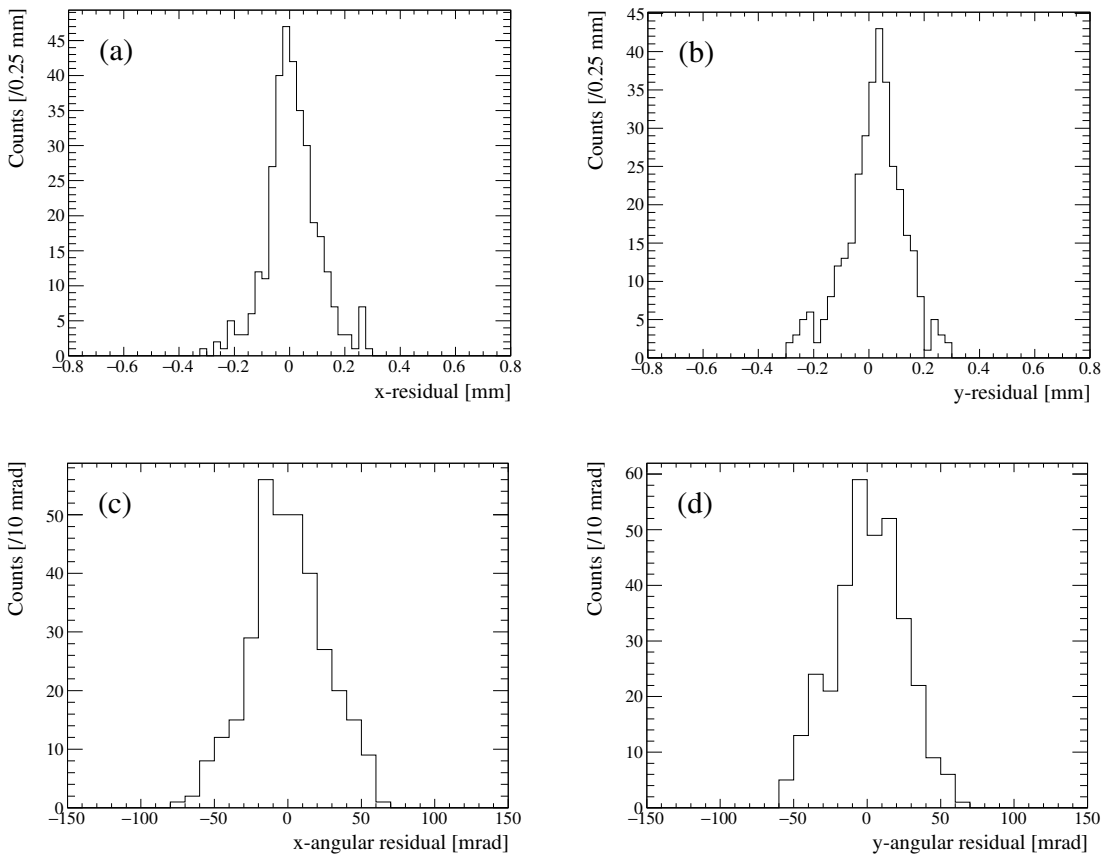

Figure 4.6: (a) x and (b) y position, and (c) x- and (d) y-angular residual distributions between the prediction and the found track.

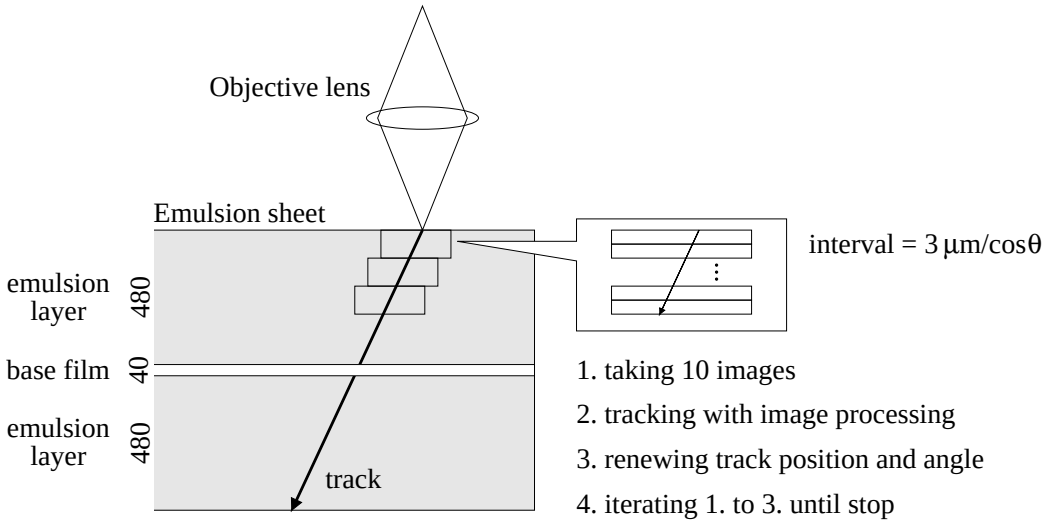

Figure 4.7: Conceptual illustration of the track following system.

system sometimes returned the wrong end points. Hence, the reasons why the following was ended were judged by human eyes with a superimposed image around the end point. The image was created by superimposing images from the upper 60 μm to lower 85 μm.

4.3.3 Event categorization

The features of the end points were categorized according to the topology and straightness of tracks as the following items. The criteria of the categorization are simplified in Table 4.1. Figures 4.8 and 4.9 present microscopic images of the example for the event categorization. The magnification and the size of the image are 50 and 145 μm $\times$ 125μm, respectively.

- ρ-stop
  No additional track of a nuclear fragment is observed from the stopping point. If an Auger electron is emitted, it presents a negative-charged particle stopped such as Ξ^- hyperon. Otherwise, there remains the possibility of a proton in addition to Ξ^-.
- σ-stop
  At least one additional charged-particle track is emitted from the stopping point. The σ-stop is discriminated with an in-flight reaction by the grain density and distortion of the track near the vertex. Owing to the large multiple scattering, the Ξ^- track becomes thick and dizzy in the case of σ-stop. Hypernuclear production is categorized as σ-stop.
- decay
  The track decays into a thin track. It presents the Ξ^- hyperon decays into a π^- meson and an invisible Λ hyperon. Since the Ξ^- decay happens in flight, the followed track is straight in most cases.
- beam interaction
  A beam particle interacts with a nucleus in emulsion. The followed track was supposed to be produced at the vertex. When the beam track is recognized as a perpendicular track to the emulsion sheet, it is interpreted as beam interaction.
- secondary interaction
  The followed particle interacts with a nucleus in emulsion. No beam track is recognized on the vertex point. The followed track is straight to be discriminated with σ-stop.
- through
  The track is followed until the most downstream surface of the emulsion module. The particle escaped from the emulsion module without interaction and decay.
- other
  The other cases are categorized such as the connection failure between two emulsion sheets, or the track lost in the base film.

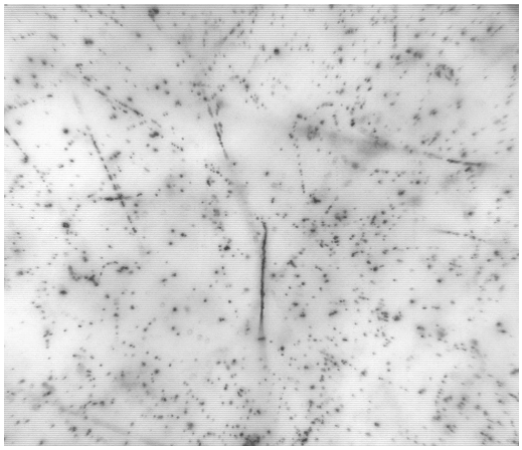

(a) ρ-stop

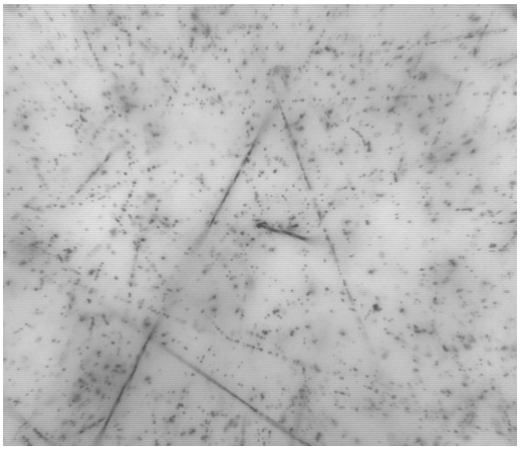

(b) ρ-stop with Auger electron

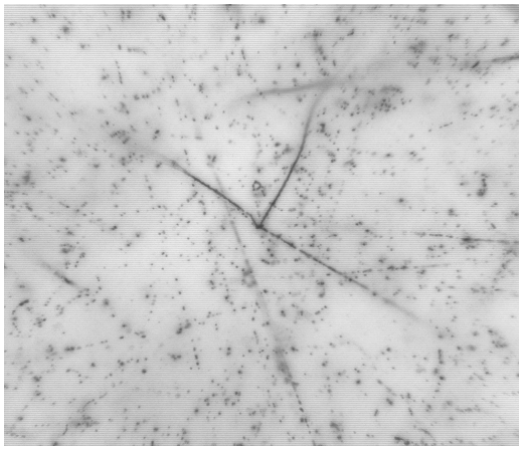

(c) σ-stop

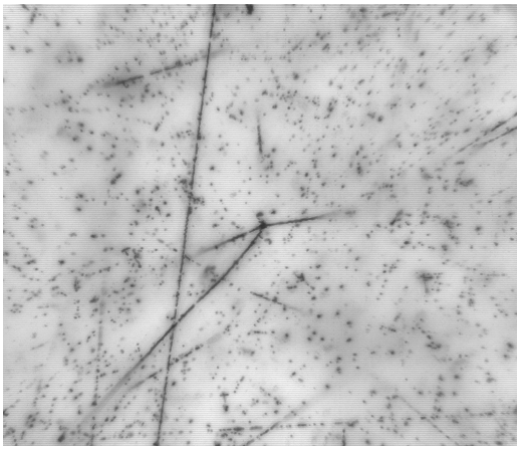

(d) σ-stop with Auger electron

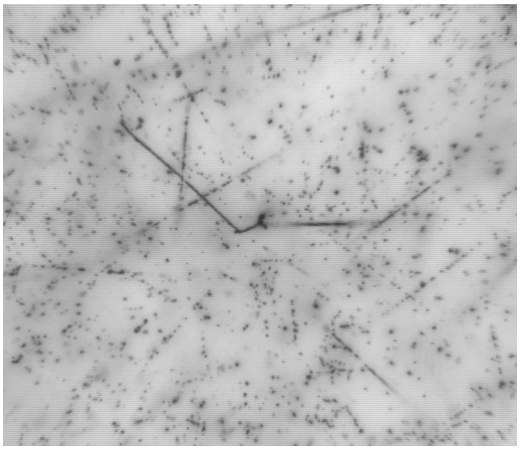

(e) σ-stop with hyperfragment

Figure 4.8: Microscopic images of examples of the event categorization Part1.

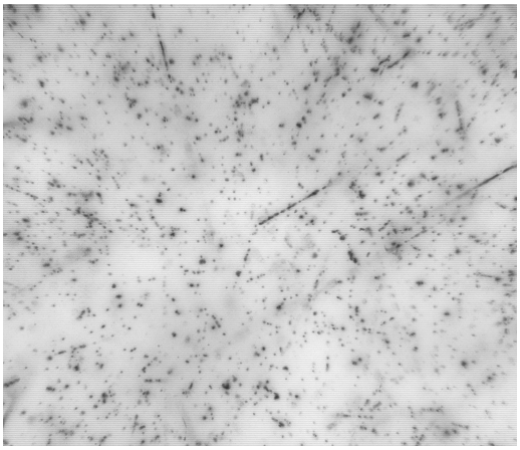

(a) decay

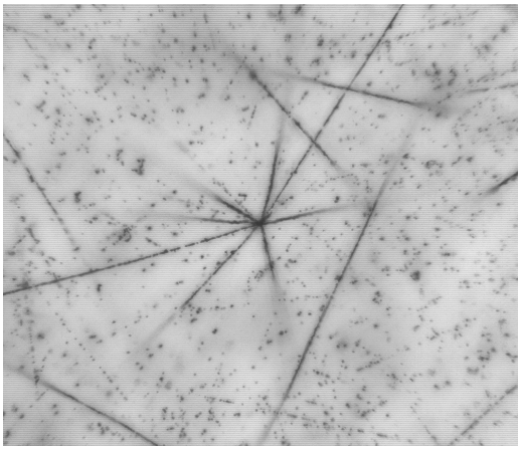

(b) beam interaction

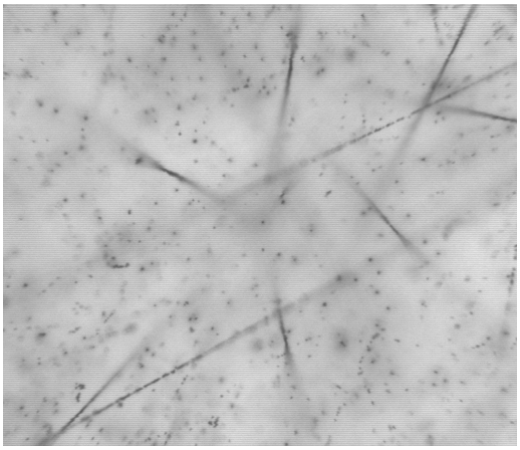

(c) beam track of beam interaction

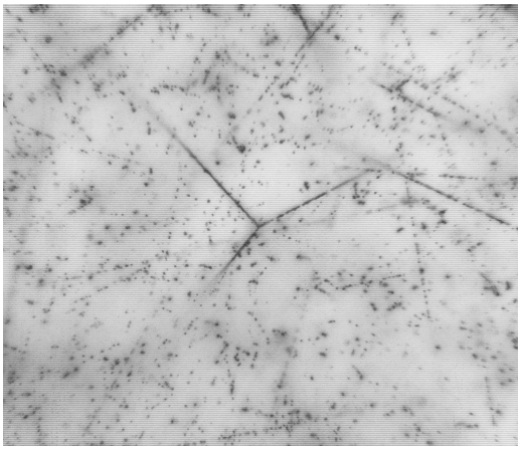

(d) secondary interaction

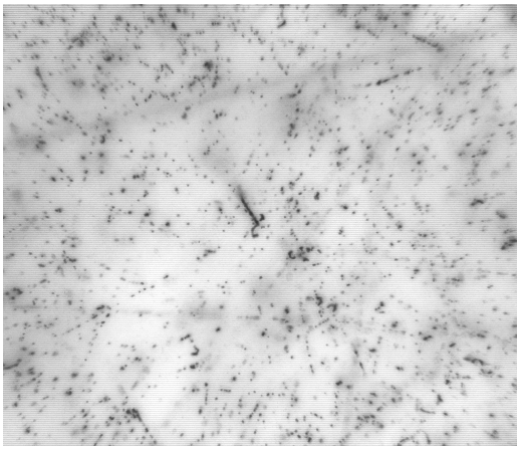

(e) secondary interaction with Auger electron

Figure 4.9: Microscopic images of examples of the event categorization Part2.

Table 4.1: Criteria of the event categorization.

category	followed track	charged-particle emission	beam track
σ-stop	dizzy	with	without
ρ-stop	dizzy	without	without
decay	straight	with a thin track	without
beam interaction	straight	with	with
secondary interaction	straight	with	without

The scanning progress is summarized in Table 4.2 while the emulsion scanning is underway. From followed twenty thousand and six hundred ninety-seven tracks, one hundred seventy-five events having multiple vertices were observed, which were hyperfragment candidates. Among them, eight events having a topology of twin Λ hypernuclei and nine events having a topology of double-Λ hypernucleus.

Table 4.2: Result of the event categorization.

followed event	15418
followed track	20697
σ-stop	1226
ρ-stop	5931
decay	4198
beam interaction	839
secondary interaction	818
through	4237
other	3448
multiple vertices	175
twin hyper nuclei	8
double hyper nucleus	9

4.4 Range-energy relation in emulsion

The observables in emulsion are a range, an angle, and a grain density. In order to calculate the masses of hypernuclei, the energy of the decay daughters are necessary. The kinetic energy of a charged particle is provided by measuring the range if we assume the nuclear species. The range-energy relation is essential for emulsion analysis.

4.4.1 Calculation of range-energy relation

For the calculation of the range-energy conversion, the following method was used. The relation was based on the practically approximated calculation for protons with the Ilford G5 emulsion, called the standard emulsion with the density of 3.815 g/cm^3. The calculation converts the energy to the range. The ranges and energy-loss rates of all real particles are expressible in terms of those for the proton. The correction terms and factors, and normalization of mass and charge are considered.

The formula of the range calculation in emulsion presented as

$$R = \frac{M}{Z^2}\lambda(\beta) + MZ^{2/3}C_Z(\beta/Z), \tag{4.1}$$

where R and Z are the range and charge. M is mass in a unit of the proton mass. C_Z is an empirical function that corrects for the extension in range caused by the neutralization of the ionic charge as electrons are captured at low velocities. The quantity C_Z was studied as a function of β/Z. Heckman et al. [76] experimentally provided accurate and detailed information for various ions. From the experimental result, all the correction factors were practically determined. $\lambda(\beta)$ is the range of a proton with velocity of βc, expressed as [77, 78]

$$\frac{\lambda_s}{\lambda} = \frac{rd-1}{rd_s-1} + \frac{r(d_s-d)}{rd_s-1}\frac{\lambda_s}{\lambda_w}, \tag{4.2}$$

where d is the emulsion density. d_s denotes the density of the standard emulsion. λ_s and λ_w are the proton range in the standard emulsion and water, respectively. where r $(= \Delta V/\Delta W)$ is the ratio of the volume increment in cubic centimeters to the weight increment in grams brought by the addition of moisture to emulsion. The range curve for water had been calculated [77, 78]. We made our range corrections using $r = 0.884$ cm^3/g. However, energy was calculated from range in the emulsion analysis. Therefore, the approximated polynomial function was practically utilized.

Even if identical particles with the same energy produce tracks in emulsion, the measured lengths of the tracks are not the same owing to the straggling. Therefore, it is necessary to consider the energy error derived from the range straggling. Barkas mentioned the range straggling effect [78] as in the following equation,

$$M\sigma_s^2/R^2 = f(\beta). \tag{4.3}$$

σ_s is the straggling. $M\sigma_s^2/R^2$ is expressed as a function of the velocity. The quantity $M^{1/2}\sigma_R/R$ was obtained for a proton at various energies as a numerical table. The relation is applicable to other particles of the same velocity. The function approximating those values with a polynomial was practically utilized. The measurement error and range straggling were combined into the energy error.

4.4.2 Range measurement with microscopic image

According to the judgment with human eyes, hypernuclear production was observed at the end point of the track following. For the precise measurement, the microscopic images were retaken with an objective lens with the magnification of 100 at the vertices. The five hundred images were taken while changing the focusing depth, z. The z-interval was 0.1 μm. The conversion factor of a pixel to actual length was 0.073955 μm/pixel, which was obtained with a glass micrometer scale. The image size was 2048×2048 for the hypernuclear events. As for the calibration data, the size of 1024×1024 was used.

The range was measured with an image processing. Figure 4.10 shows an example of the raw and processed images. Each image was processed with a Gaussian blur. The Gaussian blur is widely used to reduce image noise. Applying a Gaussian blur has the effect of reducing high-frequency components of the image. In order to enhance the contrast of the image, brightness subtraction of

the raw image from the blurred image was applied for pixel by pixel. Such image processing acted a role of a high pass filter. Owing to the processing, image noise was reduced. Brightness was inverted. Using the five hundred processed images, a track was recognized. The position of both edges of a track was manually provided as an initial parameter. The tracking using the brightness distribution was performed for every 10 μm. The range R and its error σ were calculated as the total length of partial tracks,

$$\begin{aligned} R &= \sum_i \Delta r_i = \sum_i \sqrt{\Delta x_i^2 + \Delta y_i^2 + (s \cdot \Delta z_i)^2}, \\ \sigma &= \frac{1}{R} \sum_i \Delta r_i \cdot \sigma_i = \frac{1}{R} \sum_i \sqrt{(e_x \cdot \Delta x_i)^2 + (e_y \cdot \Delta y_i)^2 + (e_z \cdot s \cdot \Delta z_i)^2} \end{aligned} \tag{4.4}$$

where Δx_i, Δy_i, and Δz_i are the length of the i-th partial track on x-, y- and z-axis, respectively. s is the shrinkage factor of the emulsion sheet. e is a range error to be 0.05 μm and 0.08 μm on xy- and z-direction. The different error values were taken into account for xy- and z-direction due to the difference of the image resolution on xy- and z-direction. Since the deformation of the xy-direction was corrected with the grid mark, the only shrinkage of z-direction was considered. Figures 4.11 present the 2-dimensional illustration of the partial tracks at the time of the measurement by microscope and the beam irradiation.

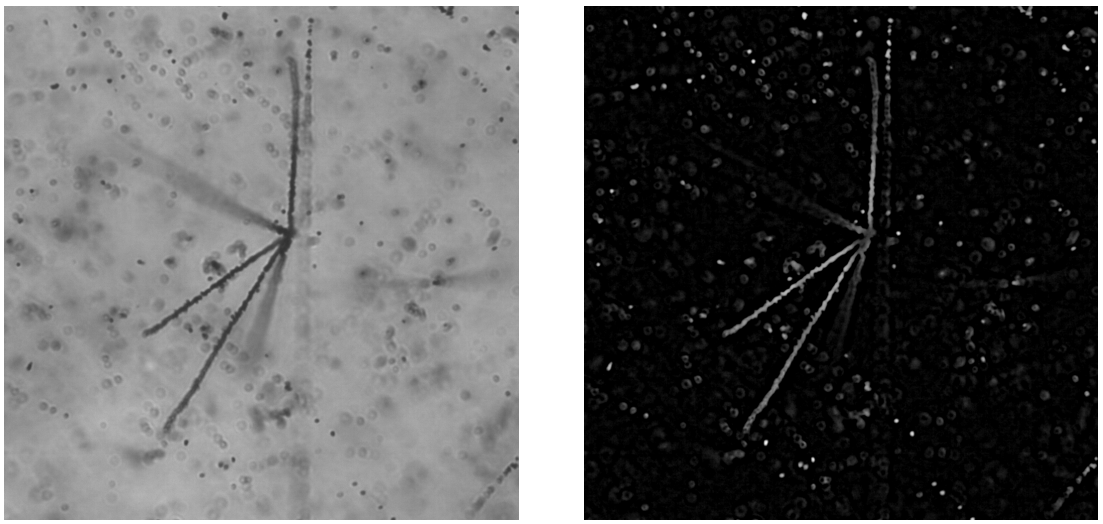

(a) Raw (b) Processed

Figure 4.10: Microscopic image processing.

4.4.3 Calibration with alpha decay

The range for the energy calculation was measured with microscopic images. However, the emulsion layer shrunk during the photographic development. The actual range of the beam exposure time was obtained from the shrinkage correction. Furthermore, the actual density of the emulsion layer was necessary to convert a range to energy.

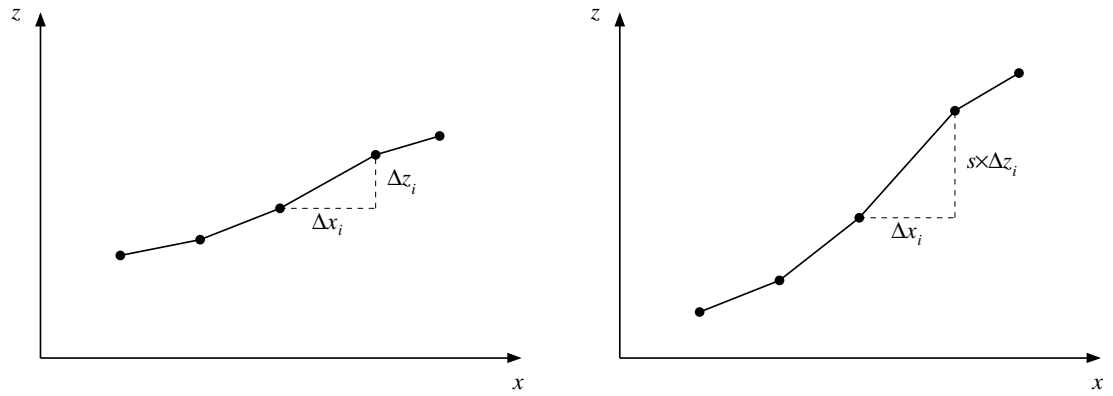

(a) At the time of measurement by microscope (b) At the time of beam irradiation

Figure 4.11: Illustration of partial tracks at the time of (a) measurement by microscope and (b) beam irradiation. The emulsion sheet is shrunk in the z direction in the development process.

The α tracks with monochromatic energy of 8.785 MeV from the decay of ^{212}Po were used for the energy calibration. Since the α has the largest kinetic energy in thorium series, the α track from the α decay of ^{212}Po is discriminated with those from other decay. Figure 4.12 shows the decay chain of the thorium series [79–84]. Five alpha decay tracks chained from ^{228}Th were observed in the emulsion layers. ^{224}Ra atoms may move thermally in emulsion due to the life time of 3.63 days. The alpha track of ^{228}Th may be observed at a little different point from others. Thus, the five-alpha-decay tracks from thorium series were observed in the emulsion layers as a five-prong star. A superimposed image of the star is shown in Figure 4.13.

The calibration with alpha decay is performed when twin Λ hypernuclei or double-Λ are found. As described in the next chapter, an event of twin Λ hypernuclei was analyzed, which was found at the emulsion sheet#10 of module#47. Therefore, alpha decay event was searched for in that emulsion sheet. Yoshida et al. [85] have developed a new scanning system. Using the image processing, images having a vertex-like feature are collected efficiently. Finally, with human eyes, one hundred thirty-two alpha-decay events were selected in total. Figure 4.14 (a) shows the range distribution of alpha decay of ^{212}Po. Without the shrinkage correction, the measured range became short depending on the angle. Considering the shrinkage effect, residuals between measured and actual range were minimized with two parameters of the shrinkage factor s and the actual range R^a instead of the emulsion density. With letting a range of the j-th alpha track to R_j, the χ^2 was defined using Eq. (4.4) as

$$\chi^2 = \sum_j^{132} \left(\frac{R_j(s) - R^a}{\sigma_j} \right)^2 = \sum_j^{132} \left(\frac{\sum_i \sqrt{\Delta x_i^2 + \Delta y_i^2 + (s \cdot \Delta z_i)^2} - R^a}{\sigma_j} \right)^2, \tag{4.5}$$

where the number 132 represents the number of α-decay tracks. Figure 4.14 (b) shows the correlation between the shrinkage factor and the actual range. From the minimization of the χ^2, the shrinkage factor and the actual range were obtained to be 2.079 ± 0.021 and $50.25 \pm 0.11 \mu$m with the reduced χ^2 of 1.61. Figure 4.14 (c) shows the range distribution with the shrinkage factor. The FWHM of the range distribution was found to be 2.35 μm.

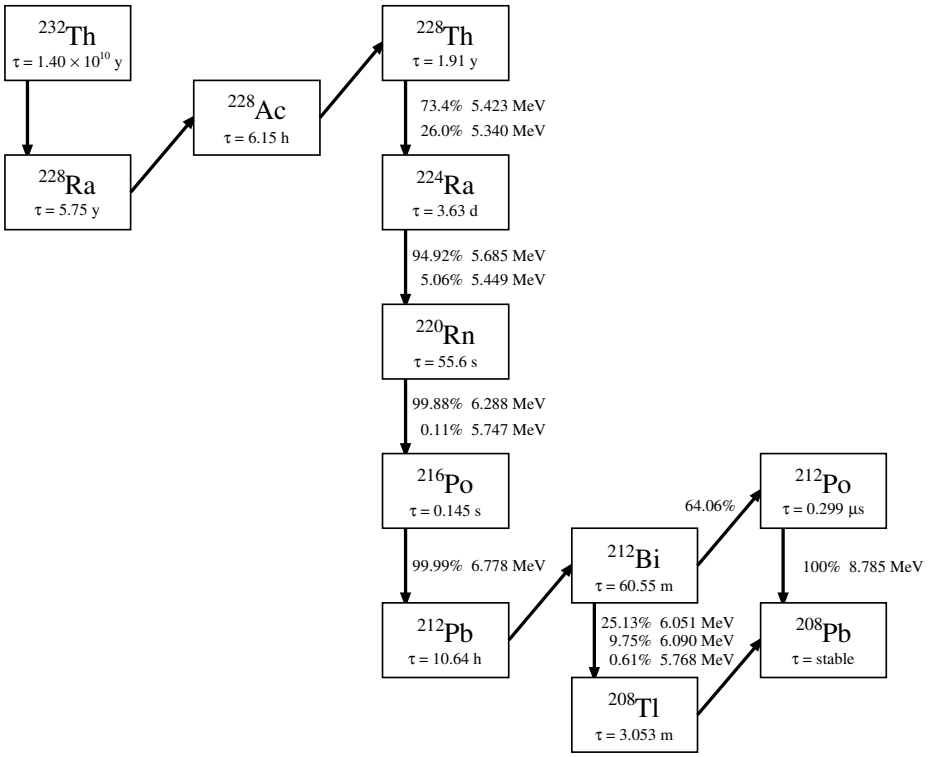

Figure 4.12: Decay chain of Thorium series.

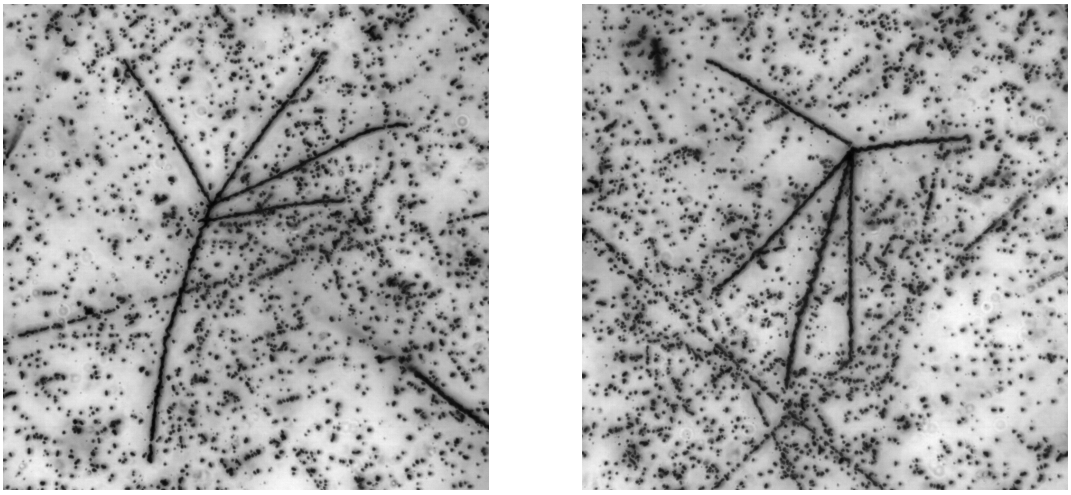

Figure 4.13: Typical superimposed image of alpha decay of thorium series.

Using energy and range of the alpha particle, the emulsion density was determined with Eq. (4.1) and (4.2). The density of the emulsion layer was obtained to be 3.544 ± 0.012 g/cm^3, as the mean value.

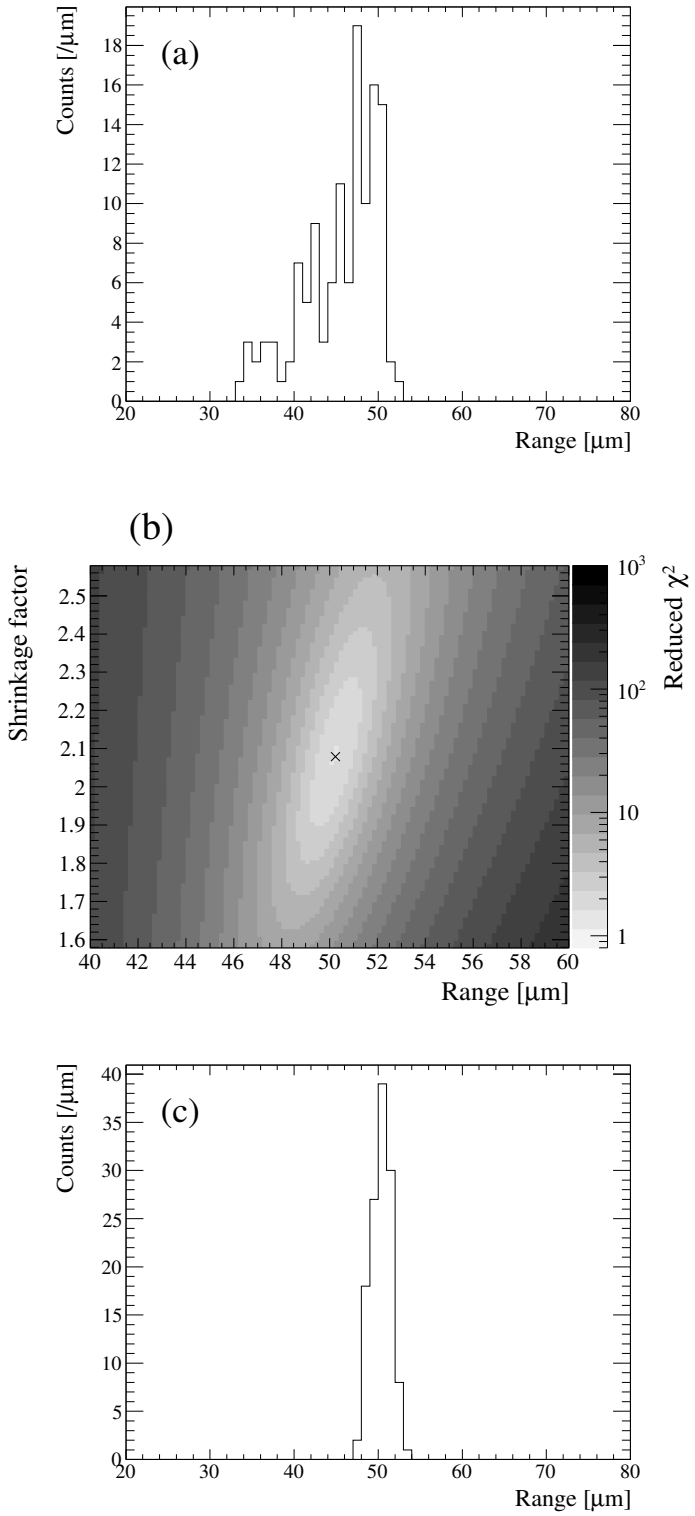

Figure 4.14: Range distributions of alpha decay of ^{212}Po. (a) without the shrinkage correction. (b) correlation of shrinkage factor versus range. (c) with the shrinkage correction.

Chapter 5

Twin Λ hypernuclei event

We have observed eight twin Λ hypernuclei events. This chapter describes the detail focusing on one of them.

5.1 Event description

The event of twin Λ hypernuclei was found at the emulsion sheet#10 of module#47. The event was reconstructed by the spectrometers as listed in Table 5.1. An incident K^- beam with the momentum of 1.806 GeV/c entered the diamond target. An outgoing K^+ meson with the momentum of 1.273 GeV/c was produced. The reconstructed mass of the K^+ meson was 0.531 GeV/c^2. A Ξ^- hyperon was produced with the K^+ meson together. The missing mass and momentum of the $p(K^-, K^+)X$ reaction were 1.338 GeV/c^2 and 0.545 GeV/c, respectively. Both of the reconstructed tracks of the K^+ meson and the Ξ^- hyperon were single. At the first thin-type emulsion sheet, two track candidates were found and traced. One stopped at the sheet#10 with the topology of twin Λ hypernuclei emission. The other passed through the last emulsion sheet. No Ξ^--like track was observed on the Ξ^- direction in SSD2. Thus, the consistency with the analysis of the spectrometers was confirmed.

Table 5.1: Analysis results of the twin Λ hypernuclei event.

K^- momentum	1.806 GeV/c
K^+ momentum	1.273 GeV/c
K^+ reconstructed mass	0.531 GeV/c^2
Ξ^- missing mass	1.338 GeV/c^2
Ξ^- missing momentum	0.545 GeV/c

Figure 5.1 shows a photograph and a schematic drawing of the twin Λ hypernuclei event, named "IBUKI event" [1]. The photograph is an overlaid image taken at various focusing depths of the microscope. The Ξ^- came to rest at vertex A, from where two charged particles, track #1 and #2, were emitted. Track #1 decayed into four charged particles, tracks #3–6, at vertex B. Since track #3 had a very short range, it is difficult to identify the topology. Both topology with/without track #3 were analyzed. Track #2 also shows a topology of decay into three charged particles, tracks #7–9, at vertex C. Hence, both track #1 and #2 were identified as a single-Λ hypernucleus. All tracks were traced manually and found the stopping points in the emulsion layer. The end of track #5 was found in sheet #11 as the ρ-stop. Track #6 stopped in sheet #3 as the ρ-stop. Track #8

[1] The name of a mountain on the border of Gifu prefecture, where the event was observed.

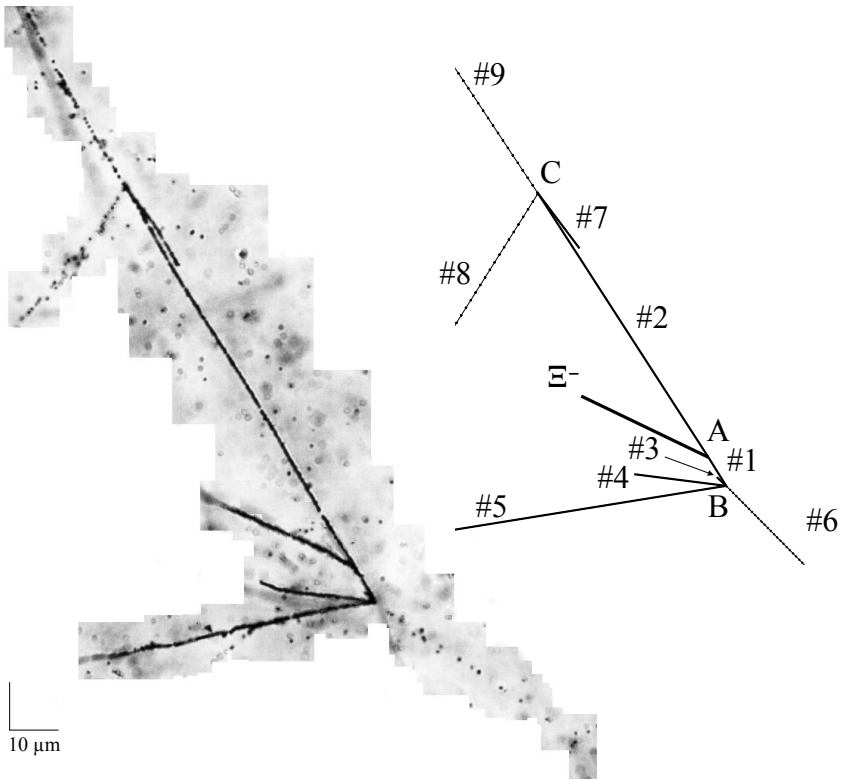

Figure 5.1: Photograph and schematic drawing of IBUKI event. See text for detailed description.

ended in sheet #12 as shown in Figure 5.2, which was recognized as the σ-stop. A charged particle was emitted to the upper-left direction. Therefore, track #8 was identified as a negative-charged particle, π^- meson. The end of track #9 was found in sheet #9 as the ρ-stop. Thus, the twin Λ hypernuclei event was observed.

The range measurement of short tracks within a microscopic view was performed with the manner described in Section 4.4.2. In order to avoid an effect of distortion aberration, images of track #2 were divided into two data sets. In the case of long tracks out of a microscopic view, the tracks were manually traced to the stopping points. The positions of the points on the track were measured at intervals of around 50 μm. The range of long tracks was calculated as the length of a polygonal line. Table 5.2 summarizes the measured ranges and the emission angles of all tracks. The angles are expressed by a zenith angle (θ) and an azimuthal angle (ϕ) in respect to the angle perpendicular to the emulsion sheet. For track #6, #8, and #9, the ranges in a base film were converted to those in the emulsion layer.

When a hypernucleus decays into three particles, those three tracks are observed on the coplanar plane. The coplanarity of three tracks from vertex C is defined as

$$c = (\boldsymbol{v_7} \times \boldsymbol{v_8}) \cdot \boldsymbol{v_9}, \tag{5.1}$$

where c is the coplanarity. $\boldsymbol{v_7}$, $\boldsymbol{v_8}$, and $\boldsymbol{v_9}$ are the unit vectors of track #7–9, respectively. The value of coplanarity was 0.061 ± 0.030. Three tracks from vertex C were coplanar with 2 σ tolerance.

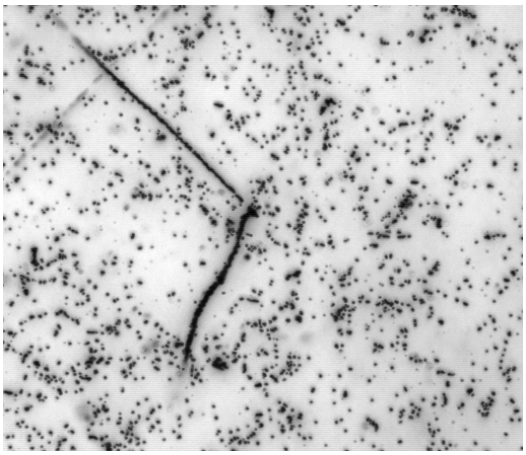

Figure 5.2: Photograph of the end point of track #8. Track #8 came to rest from the bottom. A charged particle was emitted to the upper-left direction.

Table 5.2: Measured ranges and emission angles of the tracks. The angles are expressed by a zenith angle (θ) and an azimuthal angle (ϕ) in respect to the angle perpendicular to the emulsion sheet.

Vertex	Track	Range [μm]	θ [deg]	ϕ [deg]	Comments
A	#1	8.16 ± 0.40	90.60 ± 1.88	301.85 ± 2.07	Single hypernucleus
	#2	88.49 ± 0.28	93.49 ± 1.97	122.85 ± 1.45	Single hypernucleus
B	#3	3.56 ± 1.10	124.57 ± 7.43	136.98 ± 6.41	
	#4	25.86 ± 0.29	109.82 ± 2.25	172.77 ± 1.50	
	#5	961.1 ± 4.6	49.63 ± 2.03	189.17 ± 1.96	
	#6	20508.9 ± 33.8	111.59 ± 2.66	325.53 ± 2.22	
C	#7	19.22 ± 0.14	86.75 ± 1.63	307.03 ± 1.16	
	#8	2159.0 ± 19.1	30.56 ± 1.52	237.79 ± 2.79	π^- with σ-stop
	#9	2179.0 ± 3.6	106.74 ± 1.58	123.54 ± 1.22	

5.2 Event reconstruction

If the species of a particle is known, the kinetic energy is calculated from the range using the manner described in Section 4.4.1. For each vertex points, the kinematics of all possible decay modes were examined including both mesonic and non-mesonic decay. The particle table considered in the event reconstruction is listed in Table 5.3. The initial state of the Ξ^-–nucleus system is treated as one particle in the calculation. Various nuclear species composed of the emulsion as listed in Table 2.8. However, the minimum energy of emission of charged particles differs depending on Coulomb potential. In the case of being captured by a heavy emulsion nucleus such as Ag or Br, the minimum energy corresponds to a proton range of 95 μm and α particle range of 32 μm [17]. Therefore, the existence of a short prong indicates a capture in a light emulsion nucleus such as C, N, or O. Since the length of track #1 is as short as 8.16 ± 0.40 μm, the Ξ^- hyperon was assumed to be captured in a light nucleus. Furthermore, an emission of the neutral particles was necessary to be considered. The possibilities of the emission of up to three neutral particles were included in the kinematic calculation. As for the mass of the Λ hypernuclei, the values obtained from the experimental data were utilized [9, 20, 86–92]. Mass values of some undiscovered hypernuclei were also taken into account as the estimation with the interpolation or extrapolation. The error of the estimated mass was assumed to be 0.5 MeV/c^2 uniformly. Excited states of nuclei were considered after this calculation because a nucleus with excited state makes little difference for the range measurement.

Table 5.3: Particles table considered in the event reconstruction

Type	# of particle	Elements
Ξ^-–nucleus system	7	$\Xi^- + {}^{12}$C, ^{13}C, $\cdots$ ^{17}O, and ^{18}O
Charged-particle without strangeness	66	$\pi^-, p, d, t, {}^3$He, $\cdots$ ^{19}C, ^{19}N, and ^{19}O
Neutral particle	10	$n, 2n, 3n, \pi^0, \pi^0 + n, \pi^0 + 2n, \Lambda, \cdots$ none
Single-Λ hypernuclei	41	${}^{3}_{\Lambda}$H, ${}^{4}_{\Lambda}$H, ${}^{4}_{\Lambda}$He, ${}^{5}_{\Lambda}$He $\cdots$ ${}^{17}_{\Lambda}$N and ${}^{18}_{\Lambda}$N
Double-Λ hypernuclei	40	${}^{3}_{\Lambda\Lambda}$H, ${}^{4}_{\Lambda\Lambda}$H, ${}^{5}_{\Lambda\Lambda}$He, $\cdots$ and ${}^{18}_{\Lambda\Lambda}$N

For all particle combinations, the following selection was applied.

- Strangeness is conserved for vertex A, or 1 less for vertex B and C.
- Charge is conserved.
- Baryon number is conserved.
- Q value is more than -20 MeV (only to save time to calculate).
- Magnitude of total momentum is consistent to be zero.
- Residual between invariant mass and initial mass is consistent to be zero or more.

The residual of the reconstructed invariant mass from the initial mass was calculated for each decay mode. In the case of vertex A, the sum of the masses of Ξ^- and a capturing nucleus was utilized as the initial mass. As for vertex B and C, the mass of a single hypernucleus was used. The mass difference indicates the binding energy of Ξ^- at vertex A described as below. The mass difference was accepted to be more than zero for vertex A. In decay modes containing only one neutral particle,

the invariant mass was obtained by assuming that the neutral particle emitted in such a direction as to conserve the total momentum. In decay modes including multiple neutral particles, such neutral particles were treated as to have the same direction. Therefore, those multiple neutral particles were utilized as a single particle such as '2n' and '3n'. Since this assumption provided the minimum kinetic energy of the neutral, the mass difference of more than zero was accepted in the case of the emission of multiple neutral particles.

vertex A

In the case of vertex A, the residual means the binding energy of the Ξ^- hyperon in the the Ξ^--nucleus system, defined as

$$-B_{\Xi^-} = \sqrt{(E_1 + E_2 + \sum_i E_i^0)^2 - ||\boldsymbol{p}_1 + \boldsymbol{p}_2 + \sum_i \boldsymbol{p}_i^0||^2} - M(\Xi^-) - M(^{(A-1)}(Z+1)), \qquad (5.2)$$

where B_{Ξ^-} is the binding energy of the Ξ^- hyperon. $E_{1,2}$ and $p_{1,2}$ are the total energy and momentum of track #1 and #2. E_i^0 and p_i^0 are the total energy and momentum of the i-th neutral particle. $M(\Xi^-)$ and $M(^{(A-1)}(Z+1))$ are the masses of Ξ^- and the capturing nucleus. Eq. (5.2) corresponds to Eq. (1.2). Figure 5.3 shows the result for all possible decay modes for vertex A. The open circle indicates the decay mode including the estimated mass of single hypernuclei. The magnitude of total momentum was accepted to be zero within 3 σ tolerance. The value of B_{Ξ^-} was selected to be more than zero with 3 σ tolerance. The red marker indicates the accepted decay mode. Only one decay mode remained,

$$\Xi^- + {}^{14}\mathrm{N} \rightarrow {}^{10}_{\Lambda}\mathrm{Be}(\#1) + {}^{5}_{\Lambda}\mathrm{He}(\#2)$$

All the other decay modes were inconsistent with the conservation up to 4.9 σ tolerance.

vertex B

At vertex B, the same criteria were applied using tracks #3–6. Since track #1 decayed into four charged particles, the coplanarity was not calculated. Three hundred fifty-eight possible decay modes remained within 3 σ tolerance of energy and momentum conservation. The decay modes for the case of track #1 being ${}^{10}_{\Lambda}$Be as listed in Table 5.4. Many decay modes were accepted because non-mesonic decay has a large Q value. Moreover, at least two neutral particles were likely to be emitted. Hence, the selection with the conservation was not efficient for vertex B. However, the listed thirteen decay modes were all consistent with the result at vertex A.

A different topology may be possible at vertex B. Since the length of track #3 was considerably short, the topology without track #3 was also tested. The coplanarity of tracks #4–6 was obtained to be -0.500 ± 0.034. Some neutral particle emission was expected due to the large coplanarity. The accepted decay modes for the case of track #1 being ${}^{10}_{\Lambda}$Be as listed in Table 5.5. From forty-eight candidates, the listed four decay modes were consistent with the result at vertex A. In addition, since ^{6}He decays to ^{6}Li + e^- + $\bar{\nu}$ with a half-life of 806.7 ms [93], the case of track #4 being ^{6}He was unlikely.

In any cases, although the decay mode at vertex B was not determined, track #6 was the most likely to be a proton. At least two neutrons were probably emitted.

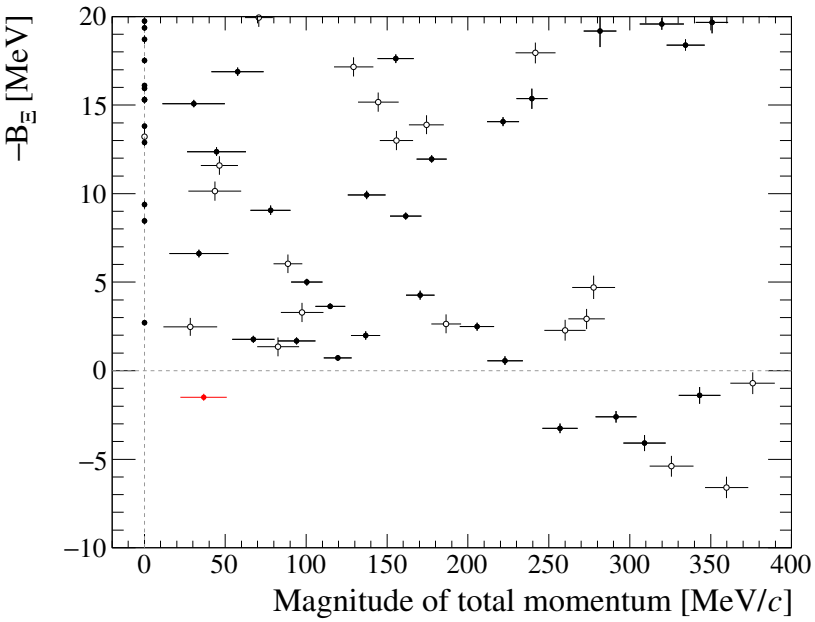

Figure 5.3: Correlation plot of energy versus momentum conservation at vertex A. The open circle indicates the decay mode including the estimated mass of single hypernuclei. The red marker indicates the accepted decay mode.

Table 5.4: Possible decay modes at vertex B for the case of track #1 being ${}^{10}_{\Lambda}$Be.

#3	#4	#5	#6	Missing	Q [MeV]	B_Λ [MeV]
p	d	t	p	$3n$	120.06	< 11.81
p	t	d	p	$3n$	120.06	< 16.36
p	t	t	p	$2n$	126.32	< 12.83
d	p	t	p	$3n$	120.06	< 12.71
d	d	d	p	$3n$	116.03	< 12.89
d	d	t	p	$2n$	122.28	< 10.04
d	t	p	p	$3n$	120.06	< 20.07
d	t	d	p	$2n$	122.28	< 15.27
t	p	d	p	$3n$	120.06	< 17.31
t	p	t	p	$2n$	126.32	< 15.09
t	d	p	p	$3n$	120.06	< 20.15
t	d	d	p	$2n$	122.29	< 15.88
t	t	p	p	$2n$	126.32	< 22.48

Table 5.5: Possible decay modes at vertex B without track #3 for the case of track #1 being ${}^{10}_{\Lambda}$Be.

#4	#5	#6	Missing	Q [MeV]	B_Λ [MeV]
^{3}He	t	p	$3n$	125.55	< 12.13
^{4}He	d	p	$3n$	139.87	< 31.13
^{4}He	t	p	$2n$	146.13	< 24.69
^{6}He	p	p	$2n$	138.63	< 27.68

vertex C

For vertex C, the consistency with the conservation laws was checked using tracks #7–9. Totally, two hundred sixty-three candidates were accepted within 3 σ tolerance of energy and momentum conservation. Almost of all were non-mesonic decay modes with multiple neutral particles. The decay modes for the case of track #2 being ${}^{5}_{\Lambda}$He was only one, obtained as the following decay mode,

$$ {}^{5}_{\Lambda}\mathrm{He} \ \rightarrow \ {}^{4}\mathrm{He}(\#7) + \pi^{-}(\#8) + p(\#9) $$

This decay mode was consistent with the σ-stop of the end point of track #8. Furthermore, this mode also had the consistency with the coplanarity of 0.061 ± 0.030. No neutral particle was likely to be emitted from vertex C with 2 σ tolerance.

Possible decay mode

From the above discussion, the reaction process of IBUKI event was obtained as follows,

$$ \begin{aligned} \Xi^{-} + {}^{14}\mathrm{N} \ &\rightarrow \ {}^{10}_{\Lambda}\mathrm{Be}(\#1) + {}^{5}_{\Lambda}\mathrm{He}(\#2), \\ {}^{10}_{\Lambda}\mathrm{Be} \ &\rightarrow \ (3 \text{ or } 4 \text{ nuclei}) + (2 \text{ or } 3 \ n) \\ {}^{5}_{\Lambda}\mathrm{He} \ &\rightarrow \ {}^{4}\mathrm{He}(\#7) + \pi^{-}(\#8) + p(\#9). \end{aligned} $$

Thus, the formation process of twin Λ hypernuclei was uniquely identified. However, moreover, some kinematic optimization was performed as described in the next section.

5.3 Kinematic optimization

5.3.1 Momentum balance correction

In the reaction process at vertex A, $\Xi^{-} + {}^{14}\mathrm{N} \rightarrow {}^{10}_{\Lambda}\mathrm{Be} + {}^{5}_{\Lambda}\mathrm{He}$, the final state was two body, twin Λ hypernuclei. Therefore, if the initial state is at rest, momenta of twin Λ hypernuclei should balance. By assuming the hypernuclear species of twin Λ hypernuclei, the range was calculated for their momenta to correspond to each other. Since tracks of Ξ^{-} hyperons become thick and dizzy, unbalanced total momentum may be caused by the ambiguity of the position of the Ξ^{-} absorption point. Hence, the range between vertex B and C was measured without the Ξ^{-} track. The range from vertex B to C was measured to be 97.12 ± 0.35 μm. From the constraint of the total length, the ranges of track #1 and 2 were calculated to be 9.40 ± 0.25 μm and 87.72 ± 0.25 μm, respectively, as listed in Table 5.6.

Table 5.6: Ranges and emission angles for vertex A with the momentum balance.

Vertex	Track	Range [μm]	θ [deg]	ϕ [deg]
A	#1	9.40 ± 0.25	90.60 ± 1.88	301.85 ± 2.07
	#2	87.72 ± 0.25	93.49 ± 1.97	122.85 ± 1.45

5.3.2 Kinematic fitting

In the above calculation, errors of all measured values were treated as to be independent, while their measured values should be utilized under the conservation laws of energy and momentum. The measurement errors were minimized by a calculation called kinematic fitting [94].

The fitting technique was based on the well-known Lagrange multiplier method. For the conservation of energy and momentum, there are four constraint equations. $\boldsymbol{\alpha}$ presents the track parameters for n tracks. A total of $3n$ parameters are inputs. The constraint equations are assumed to be linearized and summarized in two matrices. The constraint equations, $\boldsymbol{H}$, is described as

$$\boldsymbol{H}(\boldsymbol{\alpha}) \equiv (H_1, H_2, H_3, H_4) = (-M_i, 0, 0, 0)\,, \tag{5.3}$$

where $\boldsymbol{\alpha}$ is a vector of measured values. Expanding around an appropriate point $\boldsymbol{\alpha}_A$ provides the linearized equations

$$0 = [\partial \boldsymbol{H}(\boldsymbol{\alpha}_A)/\partial \boldsymbol{\alpha}](\boldsymbol{\alpha} - \boldsymbol{\alpha}_A) + \boldsymbol{H}(\boldsymbol{\alpha}_A) \equiv \boldsymbol{D}\delta\boldsymbol{\alpha} + \boldsymbol{d}, \tag{5.4}$$

where $\delta\boldsymbol{\alpha} = \boldsymbol{\alpha} - \boldsymbol{\alpha}_A$. Thus we obtain

$$\boldsymbol{D} = \begin{pmatrix} \partial H_1/\partial\alpha_1 & \partial H_1/\partial\alpha_2 & \dots & \partial H_1/\partial\alpha_n \\ \partial H_2/\partial\alpha_1 & \partial H_2/\partial\alpha_2 & \dots & \partial H_2/\partial\alpha_n \\ \vdots & \vdots & \ddots & \vdots \\ \partial H_4/\partial\alpha_1 & \partial H_4/\partial\alpha_2 & \dots & \partial H_4/\partial\alpha_n \end{pmatrix} \quad \boldsymbol{d} = \begin{pmatrix} H_1(\alpha_A) \\ H_2(\alpha_A) \\ \vdots \\ H_4(\alpha_A) \end{pmatrix}. \tag{5.5}$$

The four constraints are incorporated with the method of Lagrange multipliers. The χ^2 is written

$$\chi^2 = (\boldsymbol{\alpha} - \boldsymbol{\alpha}_0)^T \boldsymbol{V}^{-1}(\boldsymbol{\alpha} - \boldsymbol{\alpha}_0) + 2\lambda^T(\boldsymbol{D}\delta\boldsymbol{\alpha} + \boldsymbol{d}), \tag{5.6}$$

where $\boldsymbol{\lambda}$ is a vector of four unknowns, the Lagrange multipliers. $\boldsymbol{V}_{\alpha_0}^{-1}$ is the inverse of the measurement covariance matrix, given by the expression using a standard deviation of the measurement, σ_i,

$$\boldsymbol{V}_{\alpha_0}^{-1} = \begin{pmatrix} 1/\sigma_1^2 & 0 & \dots & 0 \\ 0 & 1/\sigma_2^2 & \dots & 0 \\ \vdots & \vdots & \ddots & \vdots \\ 0 & 0 & \dots & 1/\sigma_n^2 \end{pmatrix}. \tag{5.7}$$

By using the parameters $\boldsymbol{\alpha}$ and their covariance matrix $\boldsymbol{V}$, the χ^2 is minimized with respect to $\boldsymbol{\alpha}$ and $\boldsymbol{\lambda}$. The solution is written

$$\begin{aligned} \boldsymbol{\alpha} &= \boldsymbol{\alpha}_0 - \boldsymbol{V}_{\boldsymbol{\alpha}_0}\boldsymbol{D}^T\boldsymbol{\lambda} \\ \boldsymbol{\lambda} &= \boldsymbol{V}_D(\boldsymbol{D}\delta\boldsymbol{\alpha}_0 + \boldsymbol{d}) \\ \boldsymbol{V}_D &= \left(\boldsymbol{D}\boldsymbol{V}_{\alpha_0}\boldsymbol{D}^T\right)^{-1} \\ \chi^2 &= \boldsymbol{\lambda}^T(\boldsymbol{D}\delta\boldsymbol{\alpha_0} + \boldsymbol{d}). \end{aligned} \tag{5.8}$$

At vertex A, the kinematic fitting was applied. The fitting result is summarized in Table 5.7. Since the ranges of track #1 and #2 were already optimized to balance their momenta, the ranges

were not changed. The angles present twin Λ hypernuclei being back to back. The χ^2 value was obtained to be 2.409 with degree of freedom of 2. Considering the effects of straggling and the error of the emulsion density, the error of B_{Ξ^-} was measured to be 0.08 MeV. The mass errors of Ξ^- hyperon (1321.71 ± 0.07 MeV/c^2 [47]), ${}^{10}_{\Lambda}$Be (9499.88 ± 0.17 MeV/c^2 [20]), and ${}^{5}_{\Lambda}$He (4839.94 ± 0.02 MeV/c^2 [86]) were also taken into account. The mass of ${}^{10}_{\Lambda}$Be was presented as the sum of the 1^- and 2^- states. The energy spacing between these two states is expected to be less than 0.1 MeV according to a γ-ray measurement of the mirror hypernucleus^{10}0 and theoretical calculations. Therefore, the binding energy of the Ξ^- hyperon in Ξ^-–^{14}N system, $B_{\Xi^-}({}^{15}_{\Xi}\mathrm{C})$ was obtained to be 1.27 ± 0.21 MeV, where the error includes the spin-doublet uncertainty of ^{10}Be.

Table 5.7: Ranges and emission angles for vertex A with the kinematic fitting.

Vertex	Track	Range [μm]	θ [deg]	ϕ [deg]
A	#1	9.40 ± 0.06	88.65 ± 1.35	302.52 ± 1.19
	#2	87.72 ± 0.70	91.35 ± 1.35	122.52 ± 1.19

The kinematic fitting was also applied at vertex C. The result is listed in Table 5.8. The χ^2 value was obtained to be 6.622 with degree of freedom of 5. Since the straggling affects the range errors, the errors of track #8 and #9 became large from the measured values. The binding energy of Λ hyperon in ${}^{5}_{\Lambda}$He, $B_{\Lambda}({}^{5}_{\Lambda}\mathrm{He})$, was calculated to be 2.77 ± 0.23 MeV. Meanwhile, the $B_{\Lambda}({}^{5}_{\Lambda}\mathrm{He})$ value of 3.12 ± 0.02 MeV [86] was utilized in the calculation.

Table 5.8: Ranges and emission angles for vertex C with the kinematic fitting.

Vertex	Track	Range [μm]	θ [deg]	ϕ [deg]
C	#7	19.11 ± 0.20	87.04 ± 1.03	308.85 ± 0.87
	#8	2145.67 ± 71.02	29.54 ± 1.46	236.29 ± 2.19
	#9	2194.37 ± 27.57	105.72 ± 0.98	121.63 ± 0.84

5.4 Discussion

5.4.1 Consideration of excited state

The $B_{\Xi^-}({}^{15}_{\Xi}\mathrm{C})$ value of 1.27 ± 0.21 MeV presents a bound Ξ^-–^{14}N system. However, since the smaller B_{Ξ^-} value is obtained with the larger mass of daughters as shown in Eq. (5.2), the case of twin Λ hypernuclei being produced in excited states is necessary to be considered. However, the binding energy must not be negative for the consistency with the Ξ^- absorption.

With regard to ${}^{5}_{\Lambda}$He, the ground state is interpreted as the core of ^{4}He and a Λ hyperon in the s-orbital. Although there are no experimental data for the excited states of ${}^{5}_{\Lambda}$He, the low-lying state of the ${}^{4}_{\Lambda}$He is theoretically only the ground state ($1/2^+$). Therefore, the produced ${}^{5}_{\Lambda}$He was considered to be in the ground state.

The energy spectrum of ${}^{10}_{\Lambda}$Be was measured at JLab [20]. From the result, the excitation energy is reported to be 2.84 ± 0.11 MeV as the low-lying excited state. Since the excitation energy of

2.84 ± 0.11 MeV is larger than the $B_{\Xi^-}(^{15}_{\Xi}\mathrm{C})$ value of 1.27 ± 0.21 MeV, the $^{10}_{\Lambda}$Be in IBUKI event was probably not produced in such an excited state.

Thus, in IBUKI event, the value of the Ξ^- binding energy $B_{\Xi^-}(^{15}_{\Xi}\mathrm{C})$ was obtained to be 1.27±0.21 MeV for the case of the $^{10}_{\Lambda}$Be being the ground state (2^-) or the other state of the spin doublet (1^-).

Although there is a little uncertainty regarding the determination of the state, the binding energy was determined. From the above consideration, the IBUKI event was concluded to be a bound state of the Ξ^-–^{14}N system by an attractive ΞN interaction.

5.4.2 Comparison with past experiment

Several candidates of twin Λ hypernuclei events were found in the past experiments as denoted in Chapter 1.2.1. Those experiments reported the B_{Ξ^-} values as summarized in Table 5.9 together with the value obtained from the present work, IBUKI event. As for the other observed events in the past experiments, nuclear species of twin Λ hypernuclei were not identified, the process was interpreted to be consistent with a capture from an atomic bound level, or the B_{Ξ^-} value should be revised due to the modification of the nuclear and hypernuclear mass table. Therefore, such events are excluded in Table 5.9. The value of B_{Ξ^-} is decreased if one or both of the daughter Λ hypernuclei were produced in an excited state. Although three interpretations of nuclear species were accepted for both events of KEK E176 #10-9-6 and #13-11-14, the most probable decay modes are used. The B_{Ξ^-} values are plotted in Figure 5.4. The same markers indicate different interpretations for the same event. In order to present the energy level, the y-axis indicates the $-B_{\Xi^-}$ value. In events of KEK E176 #10-9-6 and #13-11-14, the Ξ^- hyperons were the most likely to be absorbed by ^{12}C nuclei. In both KISO and IBUKI event, the target nuclei were interpreted as ^{14}N.

Table 5.9: Summary of the binding energy of the Ξ^- hyperon measured in past and present experiments. There are four events in total.

Event	Target	Decay mode		B_{Ξ^-} [MeV]
KEK E176-#10-9-6 [17, 18]	^{12}C	$^{9}_{\Lambda}$Be	$^{4}_{\Lambda}$H	0.82 ± 0.17
	^{12}C	$^{9}_{\Lambda}$Be	$^{4}_{\Lambda}$H*	-0.23 ± 0.17
KEK E176-#13-11-14 [17, 18]	^{12}C	$^{9}_{\Lambda}$Be	$^{4}_{\Lambda}$H	3.89 ± 0.14
	^{12}C	$^{9}_{\Lambda}$Be	$^{4}_{\Lambda}$H*	2.84 ± 0.15
	^{12}C	$^{9}_{\Lambda}$Be*	$^{4}_{\Lambda}$H	0.82 ± 0.14
	^{12}C	$^{9}_{\Lambda}$Be*	$^{4}_{\Lambda}$H*	-0.19 ± 0.15
KISO [18, 19]	^{14}N	$^{10}_{\Lambda}$Be	$^{5}_{\Lambda}$He	3.87 ± 0.21
	^{14}N	$^{10}_{\Lambda}$Be*	$^{5}_{\Lambda}$He	1.03 ± 0.18
IBUKI (present data)	^{14}N	$^{10}_{\Lambda}$Be	$^{5}_{\Lambda}$He	1.27 ± 0.21

As for the Ξ^-–^{14}N system, the decay mode of KISO event was interpreted as $^{10}_{\Lambda}$Be + $^{5}_{\Lambda}$He or $^{10}_{\Lambda}$Be* + $^{5}_{\Lambda}$He. By considering the excitation energy levels of $^{10}_{\Lambda}$Be as well as the case IBUKI event, those $B_{\Xi^-}(^{15}_{\Xi}\mathrm{C})$ values of KISO event were provided to be 3.87 ± 0.21 MeV and 1.03 ± 0.18 MeV, respectively. The present result is consistent with KISO event if $^{10}_{\Lambda}$Be was assumed to be produced in an excited state. In the case of $^{10}_{\Lambda}$Be being in the ground state in KISO event, the difference of the B_{Ξ^-} between IBUKI event and KISO event indicates the wide natural width of the Ξ^-–^{14}N bound state, or the Ξ^- absorption in the different initial states.

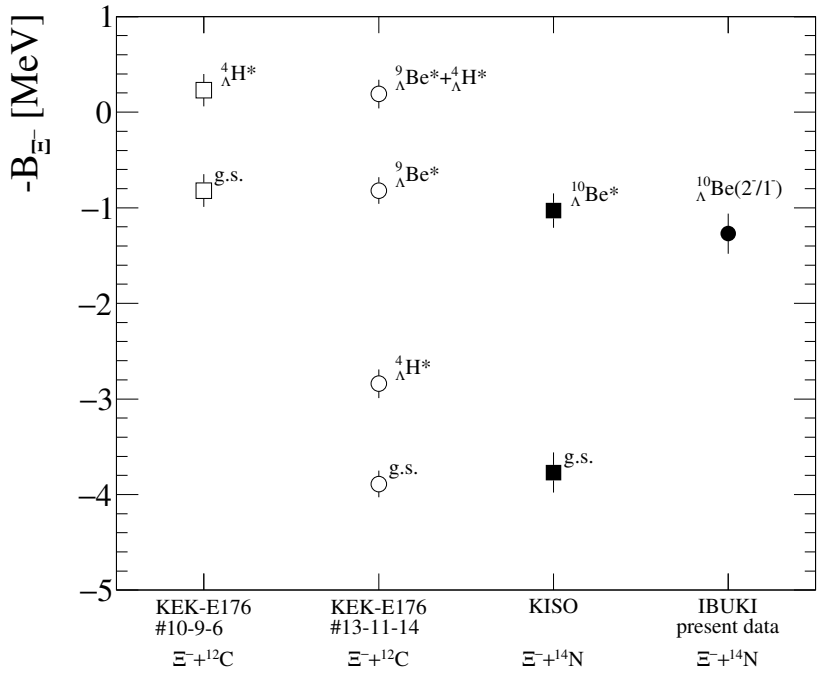

Figure 5.4: Plot of the binding energy of the Ξ^- hyperon measured in past and present experiments. The same markers indicate different interpretations for the same event.

The event of KEK E176 #10-9-6 has two interpretations of the decay mode, namely ${}^{9}_{\Lambda}\mathrm{Be} + {}^{4}_{\Lambda}\mathrm{H}$ and ${}^{9}_{\Lambda}\mathrm{Be} + {}^{4}_{\Lambda}\mathrm{H}^*$. The γ-rays associated with the transition between low-lying states of hypernuclei were measured by the ${}^{9}\mathrm{Be}(K^-, \pi^-\gamma)$ reaction [95, 96]. The measured γ-ray transition energy in the ${}^{4}_{\Lambda}\mathrm{H}^*$ was 1.04 $\pm$ 0.04 MeV, which was assigned to the $1^+ \rightarrow 0^+$ (ground) transition. The γ-ray transition energy in the ${}^{9}_{\Lambda}\mathrm{Be}^*$ was obtained to be 3.079 $\pm$ 0.04 MeV, which was assigned to the $(3/2^+, 5/2^+) \rightarrow 1/2^+$ (ground) transition. Therefore, the $B_{\Xi^-}({}^{13}_{\Xi}\mathrm{B})$ values of KEK E176 #10-9-6 were obtained to be 0.82 $\pm$ 0.17 MeV and -0.23 $\pm$ 0.17 MeV, respectively. In the event of KEK E176 #13-11-14, either or both daughter Λ hypernuclei may be produced in an excited state besides the possibility of the ground state. There were four possible decay modes, namely ${}^{9}_{\Lambda}\mathrm{Be} + {}^{4}_{\Lambda}\mathrm{H}$, ${}^{9}_{\Lambda}\mathrm{Be} + {}^{4}_{\Lambda}\mathrm{H}^*$, ${}^{9}_{\Lambda}\mathrm{Be}^* + {}^{4}_{\Lambda}\mathrm{H}$, and ${}^{9}_{\Lambda}\mathrm{Be}^* + {}^{4}_{\Lambda}\mathrm{H}^*$. Those $B_{\Xi^-}({}^{13}_{\Xi}\mathrm{B})$ values were reported to be 3.89 $\pm$ 0.14 MeV, 2.84 $\pm$ 0.15 MeV, 0.82 $\pm$ 0.14 MeV, and -0.19 $\pm$ 0.15 MeV, respectively. Assuming that the B_{Ξ^-} value in the Ξ^- hypernucleus is almost linearly dependent on the baryon number likewise the B_Λ value in the Λ hypernucleus, the $B_{\Xi^-}({}^{13}_{\Xi}\mathrm{B})$ value is close to or slightly smaller than the $B_{\Xi^-}({}^{15}_{\Xi}\mathrm{C})$ value. The $B_{\Xi^-}({}^{15}_{\Xi}\mathrm{C})$ value in IBUKI event is consistent with the $B_{\Xi^-}({}^{13}_{\Xi}\mathrm{B})$ values of the decay mode of ${}^{9}_{\Lambda}\mathrm{Be} + {}^{4}_{\Lambda}\mathrm{H}$ in KEK E176 #10-9-6. The binding energy of the decay mode of ${}^{9}_{\Lambda}\mathrm{Be}^* + {}^{4}_{\Lambda}\mathrm{H}$ in #13-11-14 event is consistent with that in IBUKI event. Other interpretations for #10-9-6 event and #13-11-14 event are inconsistent with the $B_{\Xi^-}({}^{13}_{\Xi}\mathrm{B})$ values of IBUKI event if we assume they are absorbed in the same initial state. Thus, there is a possibility of Ξ^- absorption in the same initial state for all events, although various interpretations remain without interpretation of the initial states of absorption.

5.4.3 Comparison with theoretical calculation

A theoretical calculation of the binding energies of Ξ^-–^{14}N and Ξ^-–^{12}C systems was reported by Yamaguchi et al. [44] as listed in Table 5.10. The table summarizes the calculated values of the

Table 5.10: Theoretical prediction of B_{Ξ^-} values for the Ξ^-–^{12}C system ($^{13}_{\Xi}$B) and Ξ^-–^{14}N system ($^{15}_{\Xi}$C) using Coulomb potential (C) and Coulomb + Ehime potentials (C+E) in units of MeV [44].

State	B_{Ξ^-}($^{13}_{\Xi}$B)		B_{Ξ^-}($^{15}_{\Xi}$C)	
	C	C+E	C	C+E
$1S$	0.94	4.77	1.22	5.93
$2P$	0.28	0.58	0.39	1.14
$3D$	0.126	0.126	0.174	0.174
$2S$	0.26	0.40	0.34	0.54
$3P$	0.13	0.19	0.17	0.28

binding energies using Coulomb potential (C) and Coulomb + Ehime (C+E) potentials, where the Ehime potential is one-boson-exchange potential for ΞN system derived in extension from the NN one-boson-exchange potential. The Ehime potential is treated in the framework of SU(3) invariance with effective nonet mesons in addition to the effective SU(3) violating σ meson. The SU(3) parameters and the coupling constant are determined by using the data of ΛN system and the B_{Ξ^-} values of KEK E176 experiment. However, it should be noted that the experimental result was used as input for the calculation before revised [15, 16].

By comparing the experimental values to the values in Table 5.10, the possible interpretations were derived for all events. The binding energy with only the Coulomb potential was also considered as an assumption if the contribution of the strong interaction for Ξ^-–nucleus system is small. At first, the B_{Ξ^-}($^{15}_{\Xi}$C) value in IBUKI event is consistent with the values in the $1S$ state using the Coulomb potential (C) and the $2P$ state using the Coulomb and Ehime potentials (C+E). Other states such as the $3D, 2S$ and $3P$ states are inconsistent with the B_{Ξ^-}($^{15}_{\Xi}$C) value in IBUKI event. The interpretations for KISO event branch as follows.

Case 1. IBUKI event is in the $1S$ state.
If the Ξ^- is absorbed in the $1S$ state in IBUKI event, the binding energy of the Ξ^-–^{14}N system is determined almost by the Coulomb potential. Hence, only the decay mode of $^{10}_{\Lambda}$Be* + $^{5}_{\Lambda}$He in KISO event is consistent with the values in the $1S$ state (C).

Case 2. IBUKI event is in the $2P$ state.
If the Ξ^- is absorbed in the $2P$ state in IBUKI event, the Ξ^-–^{14}N system is bound by an additional strong interaction (C+E). Although the B_{Ξ^-}($^{15}_{\Xi}$C) value of the decay modes of $^{10}_{\Lambda}$Be + $^{5}_{\Lambda}$He in KISO event is smaller than the value in the $1S$ state (C+E), the decay mode of $^{10}_{\Lambda}$Be + $^{5}_{\Lambda}$He may be interpreted as the $1S$ state of the Ξ^-–^{14}N system due to the ambiguity of the theoretical calculation. Therefore, the B_{Ξ^-}($^{15}_{\Xi}$C) values of two decay modes of $^{10}_{\Lambda}$Be + $^{5}_{\Lambda}$He and $^{10}_{\Lambda}$Be* + $^{5}_{\Lambda}$He in KISO event are consistent with the values of the $1S$ and $2P$ absorptions (C+E), respectively.

In any interpretations of the state, the binding energies of the IBUKI and KISO events were larger than the calculated values of the $3D, 2S$, and $3P$ absorptions. The possible interpretations are listed in Table 5.11. There are three interpretations for the IBUKI and KISO events.

Table 5.11: Possible interpretations for IBUKI event and KISO event.

KISO event		IBUKI event		Assumed potential
Decay mode	State	Decay mode	State	
${}^{10}_{\Lambda}\mathrm{Be}^* + {}^{5}_{\Lambda}\mathrm{He}$	$1S$	${}^{10}_{\Lambda}\mathrm{Be} + {}^{5}_{\Lambda}\mathrm{He}$	$1S$	Coulomb
${}^{10}_{\Lambda}\mathrm{Be} + {}^{5}_{\Lambda}\mathrm{He}$	$1S$	${}^{10}_{\Lambda}\mathrm{Be} + {}^{5}_{\Lambda}\mathrm{He}$	$2P$	Coulomb + Ehime
${}^{10}_{\Lambda}\mathrm{Be}^* + {}^{5}_{\Lambda}\mathrm{He}$	$2P$	${}^{10}_{\Lambda}\mathrm{Be} + {}^{5}_{\Lambda}\mathrm{He}$	$2P$	Coulomb + Ehime

As for the Ξ^-–^{12}C system, the $B_{\Xi^-}({}^{13}_{\Xi}\mathrm{B})$ value of the decay mode of ${}^{9}_{\Lambda}\mathrm{Be} + {}^{4}_{\Lambda}\mathrm{H}$ in KEK E176 #10-9-6 is consistent with the values of the $1S$ (C) and $2P$ (C+E) absorptions. If the decay mode is ${}^{9}_{\Lambda}\mathrm{Be} + {}^{4}_{\Lambda}\mathrm{H}^*$ in #10-9-6 event, $B_{\Xi^-}({}^{13}_{\Xi}\mathrm{B})$ value is consistent with the values in the $3D, 3P$ (C) and $3D, 3P$ (C+E) absorptions. The $2S$ state is unlikely for #10-9-6 event. Therefore, the interpretations for #13-11-14 event branch as follows.

Case 1. KEK E176 #10-9-6 is in the $1S$ state.
If the Ξ^- is absorbed in the $1S$ state in #10-9-6 event, the binding energy of the Ξ^-–^{12}C system is provided by almost Coulomb potential. Hence, the decay mode of ${}^{9}_{\Lambda}\mathrm{Be} + {}^{4}_{\Lambda}\mathrm{H}$ and ${}^{9}_{\Lambda}\mathrm{Be} + {}^{4}_{\Lambda}\mathrm{H}^*$ in #13-11-14 event are inconsistent with any states. The interpretation of ${}^{9}_{\Lambda}\mathrm{Be}^* + {}^{4}_{\Lambda}\mathrm{H}$ in #13-11-14 event is consistent with the $1S$ state (C). The decay mode of ${}^{9}_{\Lambda}\mathrm{Be}^* + {}^{4}_{\Lambda}\mathrm{H}^*$ in #13-11-14 event is consistent with the $3D$ and $3P$ states (C).

Case 2. KEK E176 #10-9-6 is in the $2P$ state.
If the Ξ^- is absorbed in the $2P$ state in #10-9-6 event, the Ξ^-–^{12}C system is bound by Coulomb and Ehime potentials. Although the $B_{\Xi^-}({}^{13}_{\Xi}\mathrm{B})$ values of two decay modes of ${}^{9}_{\Lambda}\mathrm{Be} + {}^{4}_{\Lambda}\mathrm{H}$ and ${}^{9}_{\Lambda}\mathrm{Be} + {}^{4}_{\Lambda}\mathrm{H}^*$ in #13-11-14 event are smaller than the value in the $1S$ state (C+E), these decay modes may be interpreted as the $1S$ state of the Ξ^-–^{12}C system. The decay mode of ${}^{9}_{\Lambda}\mathrm{Be}^* + {}^{4}_{\Lambda}\mathrm{H}$ in #13-11-14 event is consistent with the $2P$ and state (C+E). The $B_{\Xi^-}({}^{13}_{\Xi}\mathrm{B})$ value of ${}^{9}_{\Lambda}\mathrm{Be}^* + {}^{4}_{\Lambda}\mathrm{H}^*$ in #13-11-14 event is consistent with the $3D$ and $3P$ states (C).

Case 3. KEK E176 #10-9-6 is in the $3D$ or $3P$ states.
If the Ξ^- is absorbed in the $3D$ or $3P$ states in #10-9-6 event, the Ξ^-–^{12}C system is bound by almost only Coulomb potential. Therefore, the contribution of the strong interaction of Ξ^-–^{12}C system is unknown because the contribution of the strong interaction is quite small for the $3D$ and $3P$ states. The $B_{\Xi^-}({}^{13}_{\Xi}\mathrm{B})$ values of two decay modes of ${}^{9}_{\Lambda}\mathrm{Be} + {}^{4}_{\Lambda}\mathrm{H}$ and ${}^{9}_{\Lambda}\mathrm{Be} + {}^{4}_{\Lambda}\mathrm{H}^*$ in #13-11-14 event may be interpreted as the $1S$ state (C+E). The decay mode of ${}^{9}_{\Lambda}\mathrm{Be}^* + {}^{4}_{\Lambda}\mathrm{H}$ in #13-11-14 event is consistent with the $1S$ (C) and $2P$ (C+E) states. The $B_{\Xi^-}({}^{13}_{\Xi}\mathrm{B})$ value of ${}^{9}_{\Lambda}\mathrm{Be}^* + {}^{4}_{\Lambda}\mathrm{H}^*$ in #13-11-14 event is consistent with the $3D$ and $3P$ states (C, C+E).

In any interpretations of the state, the binding energies of #10-9-6 event and #13-11-14 event were inconsistent with the values in the $2S$ state. The possible interpretations are listed in Table 5.12.

There are twelve interpretations for KEK E176 #10-9-6 and #13-11-14.

Table 5.12: Possible interpretations for KEK E176 #10-9-6 and #13-11-14.

#10-9-6 event		#13-11-14 event		Assumed potential
Decay mode	State	Decay mode	State	
${}^{9}_{\Lambda}\mathrm{Be}+{}^{4}_{\Lambda}\mathrm{H}$	$1S$	${}^{9}_{\Lambda}\mathrm{Be}^{*}+{}^{4}_{\Lambda}\mathrm{H}$	$1S$	Coulomb
${}^{9}_{\Lambda}\mathrm{Be}+{}^{4}_{\Lambda}\mathrm{H}$	$1S$	${}^{9}_{\Lambda}\mathrm{Be}^{*}+{}^{4}_{\Lambda}\mathrm{H}^{*}$	$3D, 3P$	Coulomb
${}^{9}_{\Lambda}\mathrm{Be}+{}^{4}_{\Lambda}\mathrm{H}$	$2P$	${}^{9}_{\Lambda}\mathrm{Be}+{}^{4}_{\Lambda}\mathrm{H}$	$1S$	Coulomb + Ehime
${}^{9}_{\Lambda}\mathrm{Be}+{}^{4}_{\Lambda}\mathrm{H}$	$2P$	${}^{9}_{\Lambda}\mathrm{Be}+{}^{4}_{\Lambda}\mathrm{H}^{*}$	$1S$	Coulomb + Ehime
${}^{9}_{\Lambda}\mathrm{Be}+{}^{4}_{\Lambda}\mathrm{H}$	$2P$	${}^{9}_{\Lambda}\mathrm{Be}^{*}+{}^{4}_{\Lambda}\mathrm{H}$	$2P$	Coulomb + Ehime
${}^{9}_{\Lambda}\mathrm{Be}+{}^{4}_{\Lambda}\mathrm{H}$	$2P$	${}^{9}_{\Lambda}\mathrm{Be}^{*}+{}^{4}_{\Lambda}\mathrm{H}^{*}$	$3D, 3P$	Coulomb + Ehime
${}^{9}_{\Lambda}\mathrm{Be}+{}^{4}_{\Lambda}\mathrm{H}^{*}$	$3D, 3P$	${}^{9}_{\Lambda}\mathrm{Be}^{*}+{}^{4}_{\Lambda}\mathrm{H}$	$1S$	Coulomb
${}^{9}_{\Lambda}\mathrm{Be}+{}^{4}_{\Lambda}\mathrm{H}^{*}$	$3D, 3P$	${}^{9}_{\Lambda}\mathrm{Be}+{}^{4}_{\Lambda}\mathrm{H}$	$1S$	Coulomb + Ehime
${}^{9}_{\Lambda}\mathrm{Be}+{}^{4}_{\Lambda}\mathrm{H}^{*}$	$3D, 3P$	${}^{9}_{\Lambda}\mathrm{Be}+{}^{4}_{\Lambda}\mathrm{H}^{*}$	$1S$	Coulomb + Ehime
${}^{9}_{\Lambda}\mathrm{Be}+{}^{4}_{\Lambda}\mathrm{H}^{*}$	$3D, 3P$	${}^{9}_{\Lambda}\mathrm{Be}^{*}+{}^{4}_{\Lambda}\mathrm{H}$	$2P$	Coulomb + Ehime
${}^{9}_{\Lambda}\mathrm{Be}+{}^{4}_{\Lambda}\mathrm{H}^{*}$	$3D, 3P$	${}^{9}_{\Lambda}\mathrm{Be}^{*}+{}^{4}_{\Lambda}\mathrm{H}^{*}$	$3D, 3P$	Coulomb
${}^{9}_{\Lambda}\mathrm{Be}+{}^{4}_{\Lambda}\mathrm{H}^{*}$	$3D, 3P$	${}^{9}_{\Lambda}\mathrm{Be}^{*}+{}^{4}_{\Lambda}\mathrm{H}^{*}$	$3D, 3P$	Coulomb + Ehime

According to the cascade calculation, the probability of the Ξ^- capture for Ξ^-–^{14}N system from S, P, D and F atomic orbitals were estimated to be 0–0.03%, 0.2–1.3%, 54.1–75.7%, and 22.9–45.6%, respectively [97,98]. The probability of Ξ^- being absorbed in the $1S$ state is two orders of magnitude smaller than that in the $2P$ state theoretically. If we assume the binding energy with only Coulomb potential, at least the KISO and IBUKI events indicate Ξ^- absorption in the $1S$ state as shown in Table 5.11. Therefore, the strong interaction of the Ξ^-–nucleus system is likely to contribute the binding energies for all events. By combining Tables 5.11 and 5.12, The possible interpretations for all events are summarized in Table 5.13 with an assumption of Ξ^- absorption in atomic orbitals except for the $1S$ state. Finally, four possible interpretations are obtained. In any interpretations,

Table 5.13: Possible interpretations for KEK E176 #10-9-6 ,#13-11-14, KISO event, and IBUKI event. Ξ^- absorption in atomic orbitals except for the $1S$ state is assumed. The binding energies are considered to be calculated using Coulomb and Ehime potentials.

#10-9-6 event		#13-11-14 event		KISO event		IBUKI event	
Decay mode	State	Decay mode	State	Decay mode	State	Decay mode	State
${}^{9}_{\Lambda}\mathrm{Be}+{}^{4}_{\Lambda}\mathrm{H}$	$2P$	${}^{9}_{\Lambda}\mathrm{Be}^{*}+{}^{4}_{\Lambda}\mathrm{H}$	$2P$	${}^{10}_{\Lambda}\mathrm{Be}^{*}+{}^{5}_{\Lambda}\mathrm{He}$	$2P$	${}^{10}_{\Lambda}\mathrm{Be}+{}^{5}_{\Lambda}\mathrm{He}$	$2P$
${}^{9}_{\Lambda}\mathrm{Be}+{}^{4}_{\Lambda}\mathrm{H}$	$2P$	${}^{9}_{\Lambda}\mathrm{Be}^{*}+{}^{4}_{\Lambda}\mathrm{H}^{*}$	$3D, 3P$	${}^{10}_{\Lambda}\mathrm{Be}^{*}+{}^{5}_{\Lambda}\mathrm{He}$	$2P$	${}^{10}_{\Lambda}\mathrm{Be}+{}^{5}_{\Lambda}\mathrm{He}$	$2P$
${}^{9}_{\Lambda}\mathrm{Be}+{}^{4}_{\Lambda}\mathrm{H}^{*}$	$3D, 3P$	${}^{9}_{\Lambda}\mathrm{Be}^{*}+{}^{4}_{\Lambda}\mathrm{H}$	$2P$	${}^{10}_{\Lambda}\mathrm{Be}^{*}+{}^{5}_{\Lambda}\mathrm{He}$	$2P$	${}^{10}_{\Lambda}\mathrm{Be}+{}^{5}_{\Lambda}\mathrm{He}$	$2P$
${}^{9}_{\Lambda}\mathrm{Be}+{}^{4}_{\Lambda}\mathrm{H}^{*}$	$3D, 3P$	${}^{9}_{\Lambda}\mathrm{Be}^{*}+{}^{4}_{\Lambda}\mathrm{H}^{*}$	$3D, 3P$	${}^{10}_{\Lambda}\mathrm{Be}^{*}+{}^{5}_{\Lambda}\mathrm{He}$	$2P$	${}^{10}_{\Lambda}\mathrm{Be}+{}^{5}_{\Lambda}\mathrm{He}$	$2P$

KISO event and IBUKI event are likely to be Ξ^- absorption in the $2P$ state. The events of KEK E176 #10-9-6 and #13-11-14 may be interpreted as the $2P, 3D$, or $3P$ states.

At least the KISO and IBUKI events of four events present the Ξ^- capture in the $2P$ state. On the other hand, even if we assume Ξ^- absorption in atomic orbitals except for the $1S$ state, the probability of the Ξ^- capture is theoretically estimated to be as small as 0.2–1.3% in the $2P$ state. The result may indicate that twin Λ hypernuclei may be more likely to be produced by the Ξ^- absorption in the $2P$ state than the $3D$ state. The events with the Ξ^- capture in the $3D$ state are important for a further study of the production rate of twin Λ hypernuclei. Furthermore, twin

Λ hypernuclear data without uncertainty is necessary in order to investigate the nuclide dependence of the binding energy.

With an assumption of Ξ^- absorption in the $2P$ state for both KISO event and IBUKI event, the $B_{\Xi^-}(^{15}_{\Xi}\mathrm{C})$ values of the KISO and IBUKI events are 1.03 ± 0.18 and 1.27 ± 0.21 MeV, respectively. In any cases of the decay mode of IBUKI event, it is difficult to discuss the width because the difference of the $B_{\Xi^-}(^{15}_{\Xi}\mathrm{C})$ values between the KISO and IBUKI events is comparable to the errors. As for the Ξ^-–^{12}C system, if we assume Ξ^- absorption in the $2P$ state for both KEK E176 #10-9-6 and #13-11-14, the $B_{\Xi^-}(^{13}_{\Xi}\mathrm{B})$ values of both events are estimated to be the same value, 0.82 ± 0.17 and 0.82 ± 0.14 MeV. Further statistics without uncertainty are indispensable for more precise measurement of the binding energy and the width.

5.4.4 Extraction of ΞN interaction

Using the experimental data of the Ξ^-–nucleus interaction, information of the ΞN interaction can be extracted. Since the hyperon–nucleon and hyperon–hyperon scattering experiments are difficult due to the short life time of hyperons, the hypernuclear structure has been investigated. Regarding to the Λ hypernuclei, the effective ΛN interaction was constructed via a G-matrix calculation starting from the two-body interactions in free space. As was the case with the Λ hypernuclei, the effective ΞN interaction in the the Ξ^-–nucleus system can be calculated. However, scarce hyperon–nucleon scattering data were used to adjust parameters for theoretical models. The Ξ hypernuclear data with small ambiguity such as IBUKI event is essential for the calculation to extract the ΞN interaction. The Ehime model suggested the narrow width less than 0.1 MeV for the Ξ–^{12}C system in the $2P$ bound state. With further experimental data, information on the imaginary part of the Ξ potential is obtained by determing the width.

Chapter 6

Summary

For understanding the baryon–baryon interaction as an extension of the nuclear force, a study on octet baryons in the $SU(3)_{\text{flavor}}$ symmetry is essential. In particular, an experimental investigation around the $S = -2$ sector has been awaited to explore such extended baryon–baryon interaction.

Thus, to study twin Λ hypernuclei and a double-Λ hypernucleus, an experiment with hybrid emulsion method, J-PARC E07 experiment, was performed using a K^- meson beam with the momentum of 1.81 GeV/c at J-PARC K1.8 beam line. Ξ^- hyperons were produced via the quasi-free $p(K^-, K^+)$ reaction at a diamond target. A method using combined information between two spectrometers and nuclear emulsion, called hybrid emulsion method, was conducted by using silicon-strip detectors and one hundred eighteen emulsion modules. In total, 1.13×10^{11} K^- meson beams were irradiated to the emulsion. According to the prediction of the positions and angles of Ξ^- hyperons, the emulsion module have been scanned with a newly developed scanning system. The number of stopped-Ξ^- events exceeded that of the past KEK experiment.

From the prediction of the spectrometer analysis, we observed eight events having a topology of twin Λ hypernuclei and nine events having a topology of double-Λ hypernucleus while the emulsion scanning is under way. One twin Λ hypernuclei event, named "IBUKI event", was observed at the sheet #10 of module #47. At the Ξ^- capture point, two Λ hypernuclei of ${}^{10}_{\Lambda}\text{Be}$ and ${}^{5}_{\Lambda}\text{He}$ were the most likely to be produced by 4.9 σ of the conservation laws of energy and momentum. The reaction process of the IBUKI event was identified as $\Xi^- + {}^{14}\text{N} \to {}^{10}_{\Lambda}\text{Be} + {}^{5}_{\Lambda}\text{He}$. The binding energy of $\Xi^- + {}^{14}\text{N}$ system was determined to be 1.27 ± 0.21 MeV by applying the kinematic fitting. From the consideration of an excited state, the energy level for ${}^{10}_{\Lambda}\text{Be}$ was interpreted to be the ground state (2^-) or the other state of the spin doublet (1^-). The IBUKI event was the first event whose binding energy was determined with a little ambiguity. The binding energy indicates a bound state of the Ξ^-–${}^{14}\text{N}$ system by an attractive ΞN interaction. Furthermore, the binding energy of Λ hyperon in ${}^{5}_{\Lambda}\text{He}$ was obtained to be 2.77 ± 0.23 MeV using vertex C.

The binding energy B_{Ξ^-} was compared with past experimental results. The KISO event in KEK E373 experiment was also interpreted as the same twin Λ hypernuclear production as the IBUKI event. The present result is consistent with the KISO event in the case of ${}^{10}_{\Lambda}\text{Be}$ being an excited state in the KISO event. Although the difference between Ξ^-–${}^{14}\text{N}$ and Ξ^-–${}^{12}\text{C}$ systems should be taken into account for the comparison, the present data is also consistent with the events of KEK E176 #10-9-6 and #13-11-14 with an assumption of the excited states. Since the probability of Ξ^- being absorbed in the $1S$ state is two orders of magnitude smaller than that in the $2P$ state theoretically, Ξ^- absorption in atomic orbitals except for the $1S$ state was assumed. The Ξ^- captures for IBUKI event and KISO event are the most likely to be in the $2P$ state. The interpretations of KEK E176

#10-9-6 and #13-11-14 are possible to be Ξ^- absorption in not only the $2P$ state but also the $3D, 3P$ states.

The present experiment have observed several twin Λ hypernuclei and double-Λ hypernuclei. Many events found one after another are expected to provide us essential and rich information of ΞN and $\Lambda\Lambda$ interactions such as the natural widths of Ξ^-–nucleus bound states and the nuclide dependence of the binding energy. Such studies are possible when the emulsion scanning proceeds in the near future. We believe that spectroscopic analysis using emulsion derives further understanding for baryon–baryon interaction in $S = -2$.

Acknowledgment

First of all, I would like to express the deepest appreciation to all the people who worked together, provided advice, supported, and encouraged for the accomplishment of the present thesis. In particular, I would like to express my sincere gratitude to Prof. Atsushi Sakaguchi who provided carefully considered feedback and valuable comments. He always encouraged me with his constructive suggestion and profound knowledge for physics whenever I had a trouble in the experiment and analysis.

I am deeply grateful to the spokesperson of the present experiment, Prof. Kazuma Nakazawa from Gifu University for his continuous support for my working on the experiment. He provided great advice with encyclopedic knowledge of emulsion.

I would like to express my gratitude to all the collaborators of the J-PARC E07 experiment. The preparation, conduct, and data analysis of the present experiment could not be achieved without their great cooperation. I am grateful to Mr. Hiroyuki Ekawa for his powerful and tireless contribution as a doctoral student in the same experiment. I appreciate the contribution of Dr. Junya Yoshida, Dr. Masahiro Yoshimoto, Dr. Shinji Kinbara, Ms. Yoko Endo, Mr. Masaki Ohashi, Mr. Ryosuke Goto, Mr. Yuichi Nagase, Mr. Daisuke Nakashima, Mr. Hiroki Ito, Dr. Myint Kyaw Soe, Ms. Aye Moh Moh Theint, Ms. Go Sian Huai, and Ms. May Sweet for their preparation, development, and analysis of emulsion. I learned many things about emulsion by Dr. Yoshida. I would like to express my thank to Dr. Sang Hoon Hwang, Dr. Kenji Hosomi, and Dr. Yudai Ichikawa. They provided great efforts for the construction of the spectrometer. Dr. Hosomi taught me the foundation of the data aquisition system. I would like to show my appreciation to Mr. Jaeyong Lee, Dr. Ryuta Kiuchi, Mr. Toyoki Watabe, Mr. Masanori Hirose, and Mr. Kazuya Ito for a hard task of the development of SSD and emulsion mover. Owing to them, SSD, the key detector of the experiment, worked well. I am thankful to Prof. Koji Miwa and Dr. Ryotaro Honda. They always handled my sudden requirement of trigger electronics. I would like to acknowledge Prof. Hirokazu Tamura, Prof. Kiyoshi Tanida, Prof. Toshiyuki Takahashi, Dr. Mifuyu Ukai, Dr. Takeshi Yamamoto for the kind help and advice.

I have spent my graduate school days as a member of the "Nuclear Spectroscopy Group" in Osaka University. I am grateful to Ms. Manami Nakagawa, Mr. Yoshiyuki Nakada, Mr. Ken'ichiro Oue, Mr. Tomonari Hayakawa, Mr. Kazuya Kobayashi, and Mr. Suharu Hoshino for the help and encouragement. I enjoyed working at K1.8 beam line with them together.

I have also belonged to the "Research Group for Hadron Physics" in JAEA during a doctoral course. I would like to offer my thanks to Prof. Hiroyuki Sako, Prof. Shoichi Hasegawa, Prof. Susumu Sato for warm advise.

The present experiment was successfully performed by virtue of efforts of many staffs of J-PARC and KEK. I owe my deepest gratitude to the Hadron beam channel group and accelerator group in

J-PARC for providing high quality beams.

Finally, I would like to express my heartfelt appreciation to my family. I was able to complete this thesis owing to their continuous support and warm encouragements.

Bibliography

[1] V. G. J. Stoks *et al.*, Phys. Rev. C **49**, 2950 (1994).

[2] R. B. Wiringa, V. G. J. Stoks, and R. Schiavilla, Phys. Rev. C **51**, 38 (1995).

[3] R. Machleidt, Phys. Rev. C **63**, 024001 (2001).

[4] H. J. Pirner and J. P. Vary, Phys. Rev. Lett. **46**, 1376 (1981).

[5] M. Gell-Mann, Phys. Lett. **8**, 214 (1964).

[6] G. Zweig, CERN Report 8182/TH.401 (1964).

[7] G. Zweig, CERN Report 8419/TH.412 (1964).

[8] M. Danysz, J. Pniewski, Philos. Mag. **44**, 348 (1953).

[9] O. Hashimoto, H. Tamura, Prog. Part. Nucl. Phys. **57**, 564 (2006).

[10] D. H. Wilkinson *et al.*, Phys. Rev. Lett. **3**, 397 (1959).

[11] B. Bhowmik, Nuov. Cim. **29**, 1 (1963).

[12] P. H. Steinberg and R. J. Prem, Phys. Rev. Lett. **11**, 429 (1963).

[13] A. Bechdolff, G. Baumann, J. P. Gerber, and P. Cüer, Phys. Lett. B **26**, 174 (1968).

[14] A. S. Mondal, A. K. Basak, M. M. Kasim, and A. Husain, Nuov. Cim. A **54**, 333 (1979).

[15] S. Aoki *et al.*, Prog. Theor. Phys. **89**, 493 (1993).

[16] S. Aoki *et al.*, Phys. Lett. B **355**, 45 (1995).

[17] S. Aoki *et al.*, Nucl. Phys. A **828**, 191 (2009).

[18] E. Hiyama and K. Nakazawa, Annu. Rev. Nucl. Part. Sci. **68**, 13159 (2018).

[19] K. Nakazawa *et al.*, Prog. Theor. Exp. Phys. **2015**, 033D02 (2015).

[20] T. Gogami *et al.*, Phys. Rev. C **93**, 034314 (2016).

[21] M. Danysz *et al.*, Nucl. Phys. **49**, 121 (1963).

[22] D. J. Prowse, Phys. Rev. Lett. **17**, 782 (1966).

[23] A. S. Mondal, A. K. Basak, M. M. Kasim, and A. Husain, Nuov. Cim. A **28**, 42 (1975).

[24] R. H. Dalitz *et al.*, Proc. Roy. Soc. Lond. A **426**, 1 (1989).

[25] D. H. Davis, Nucl. Phys. A **754**, 3c (2005).

[26] J. K. Ahn *et al.*, Phys. Rev. C **88**, 014003 (2013).

[27] H. Takahashi, *et al.*, Phys. Rev. Lett. **87**, 212502 (2001).

[28] T. Fukuda *et al.*, Phys. Rev. C **58**, 1306 (1998).

[29] P. Khaustov *et al.*, Phys. Rev. C **61**, 054603 (2000).

[30] T. Tamagawa *et al.*, Nucl. Phys. A **691**, 234c (2001).

[31] M. M. Nagels, T. A. Rijken, and J. J. de Swart, Phys. Rev. D **12**, 744 (1975).

[32] M. M. Nagels, T. A. Rijken, and J. J. de Swart, Phys. Rev. D **15**, 2547 (1977).

[33] M. M. Nagels, T. A. Rijken, and J. J. de Swart, Phys. Rev. D **20**, 1633 (1979).

[34] C. B. Dover and A. Gal, Ann. Phys. **146**, 309 (1983).

[35] T. A. Rijken, V. G. J. Stoks, and Y. Yamamoto, Phys. Rev. C **59**, 21 (1999).

[36] T. A. Rijken, Nucl. Phys. A **691**, 322c (2001).

[37] T. A. Rijken, Phys. Rev. C **73**, 044007 (2006).

[38] T. A. Rijken and Y. Yamamoto, Phys. Rev. C **73**, 044008 (2006).

[39] T. A. Rijken, M. Nagels, and Y. Yamamoto, Nucl. Phys. A **835**, 160 (2010).

[40] Y. Yamamoto, E. Hiyama, and T. Rijken, Nucl. Phys. A **835**, 350 (2010).

[41] T. Rijken, M. Nagels, and Y. Yamamoto, Prog. Theor. Phys. Suppl. **185**, 14 (2010).

[42] T. Rijken, M. Nagels, and Y. Yamamoto, Few-Body Syst. **54**, 801 (2013).

[43] T. Ueda, K. Tominaga, M. Yamaguchi, and N. Kijima, Prog. Theor. Phys. **99**, 891 (1998).

[44] M. Yamaguchi, K. Tominaga, Y. Yamamoto, and T. Ueda, Prog. Theor. Phys. **105**, 627 (2001).

[45] I. N. Filikhin and A. Gal, Phys. Rev. C **65**, 041001 (2002).

[46] E. Hiyama *et al.*, Phys. Rev. C **66**, 024007 (2002).

[47] Particle Data Group, Phys. Lett. B **667**, 1061 (2008).

[48] E. Hiyama, M. Kamimura, Y. Yamamoto, and T. Motoba, Phys. Rev. Lett. **104**, 212502 (2010).

[49] K. Imai, K. Nakazawa, and H. Tamura, Proposal for Nuclear and Particle Physics Experiments at J-PARC, `https://j-parc.jp/researcher/Hadron/en/pac_0606/pdf/p07-Nakazawa.pdf` (2006).

[50] S. Nagamiya, Prog. Theor. Exp. Phys. **2012**, 02B001 (2012).

[51] M. Ikegami, Prog. Theor. Exp. Phys. **2012**, 02B002 (2012).

[52] H. Hotchi *et al.*, Prog. Theor. Exp. Phys. **2012**, 02B003 (2012).

[53] T. Koseki *et al.*, Prog. Theor. Exp. Phys. **2012**, 02B004 (2012).

[54] K. Agari *et al.*, Prog. Theor. Exp. Phys. **2012**, 02B009 (2012).

[55] S. Callier *et al.*, Phys. Proc. **37**, 1569 (2012).

[56] R. Honda *et al.*, PoS PhotoDet2012 **158**, 031 (2012).

[57] T. Uchida, IEEE Trans. Nucl. Sci., **55**, 1631 (2008).

[58] R. Honda *et al.*, Nucl. Inst. and Meth. A **787**, 157 (2015).

[59] O. Sasaki and M. Yoshida, IEEE Trans. Nucl. Sci. **46**, 1871 (1999).

[60] J. Y. Lee *et al.*, Proc. 2nd Int. Symp. Science at J-PARC, JPS Conf. Proc. **8**, 021008 (2015).

[61] J. Y. Lee *et al.*, Proc. 12th Int. Conf. on HYP2015, JPS Conf. Proc. **17**, 033004 (2017).

[62] M. J. French *et al.*, Nucl. Inst. and Meth. A **466**, 359 (2001).

[63] C. Irmler *et al.*, J. Instrum. **7**, C01082 (2012).

[64] T. Akagi *et al.*, Phys. Rev. D **51**, 2061 (1995).

[65] R. Honda (private communication).

[66] *Hadron Universal Logic Module – Open-It*, `https://openit.kek.jp/project/HUL/HUL`.

[67] Y. Igarashi *et al.*, IEEE Trans. Nucl. Sci. **57**, 618 (2010).

[68] Y. Igarashi *et al.*, IEEE Trans. Nucl. Sci. **52**, 2866 (2005).

[69] S. Morinobu (private communication).

[70] T. Matsuo *et al.*, J. Mass Spectrom. **24**, 19 (1976).

[71] Electromagnetics Suite 15.0, Maxwell 3D, ANSYS, Inc., Canonsburg, PA, USA.

[72] J. Myrheim and L. Bugge, Nucl., Inst. Meth. **160**, 43 (1979).

[73] M. Tanabashi *et al.*, (Particle Data Group), Phys. Rev. D **98**, 030001 (2018).

[74] S. Agostinelli *et al.*, Nucl. Inst. Meth. A **506**, 250 (2003).

[75] M. K. Soe *et al.*, Nucl. Inst. Meth. Phys. Res. Sect. A **848**, 66 (2017).

[76] H. H. Heckman *et al.*, Phys. Rev. **117**, 544 (1960).

[77] W. H. Barkas *et al.*, Nuov. Cim. **8**, 185 (1958).

[78] W. H. Barkas, *Nuclear Research Emulsions* (Academic Press, New York, 1963).

[79] M. J. Martin, Nuclear Data Sheets **108**, 1583 (2007).

[80] E. Browne, Nuclear Data Sheets **104**, 427 (2005).

[81] S. -C. WU, Nuclear Data Sheets **108**, 1057 (2007).

[82] E. Browne, J. K. Tuli, Nuclear Data Sheets **112**, 1115 (2011).

[83] S. Singh, B. Singh, Nuclear Data Sheets **130**, 127 (2015).

[84] K. Abusaleem, Nuclear Data Sheets **116**, 163 (2014).

[85] J. Yoshida *et al.*, Nucl. Inst. Meth. Phys. Res. Sect. A **847**, 86 (2017).

[86] M. Jurič *et al.*, Nucl. Phys. B **52**, 1 (1973).

[87] R. Bertini *et al.*, Nucl. Phys. A **368**, 365 (1981).

[88] M. May *et al.*, Phys. Rev. Lett. **47**, 1106 (1981).

[89] D. H. Davis, Contemp. Phys. **27**, 91 (1986).

[90] P. Dłużewski *et al.*, Nucl. Phys. A **484**, 520 (1988).

[91] F. Cusanno *et al.*, Phys. Rev. Lett. **103**, 202501 (2009).

[92] T. Gogami *et al.*, Phys. Rev. C **94**, 021302 (2016).

[93] D. R. Tilley *et al.*, Nucl. Phys. A **708**, 3 (2002).

[94] P. Avery, CLEO Note CBX 91-72, `https://www.phys.ufl.edu/~avery/fitting.html` (1991).

[95] M. Bedjidian *et al.*, Phys. Lett. B **83**, 252 (1979).

[96] M. May *et al.*, Phys. Rev. Lett. **51**, 2085 (1983).

[97] D. Zhu, C. B. Dover, A. Gal, and M. May, Phys. Rev. Lett. **67**, 2268 (1991).

[98] C. J. Batty, E. Friedman, and A. Gal, Phys. Rev. C **59**, 295 (1999).